

University of Montana

## ScholarWorks at University of Montana

---

Graduate Student Theses, Dissertations, &  
Professional Papers

Graduate School

---

2014

# The Development and Study of Surface Bound Ruthenium Organometallic Complexes

Geoffrey Reuben Abbott

Follow this and additional works at: <https://scholarworks.umt.edu/etd>

**Let us know how access to this document benefits you.**

---

### Recommended Citation

Abbott, Geoffrey Reuben, "The Development and Study of Surface Bound Ruthenium Organometallic Complexes" (2014). *Graduate Student Theses, Dissertations, & Professional Papers*. 10761.  
<https://scholarworks.umt.edu/etd/10761>

This Dissertation is brought to you for free and open access by the Graduate School at ScholarWorks at University of Montana. It has been accepted for inclusion in Graduate Student Theses, Dissertations, & Professional Papers by an authorized administrator of ScholarWorks at University of Montana. For more information, please contact [scholarworks@mso.umt.edu](mailto:scholarworks@mso.umt.edu).

**The Development and Study of Surface Bound Ruthenium  
Organometallic Complexes.**

By  
Geoffrey Reuben Abbott  
B.S. in Forensic Science/Chemistry, West Virginia University,  
Morgantown, WV 2009

Dissertation

Presented in Partial Fulfillment of the requirements for the degree of  
Doctor of Philosophy, in Inorganic Chemistry  
The University of Montana  
Missoula, MT  
Spring 2014

Approved by:

J.B. Alexander Ross, Dean of the Graduate School and Committee Member

Dr. Edward Rosenberg Committee Chair  
Department of Chemistry

Dr. Bruce Bowler, Committee Member  
Department of Chemistry

Dr. Valeriy Smirnov, Committee Member  
Department of Chemistry

Dr. Keith Parker, Committee Member  
Department of Biomedical and Pharmaceutical Sciences

---

UMI Number: 3628939

All rights reserved

INFORMATION TO ALL USERS

The quality of this reproduction is dependent upon the quality of the copy submitted.

In the unlikely event that the author did not send a complete manuscript and there are missing pages, these will be noted. Also, if material had to be removed, a note will indicate the deletion.



UMI 3628939

Published by ProQuest LLC (2014). Copyright in the Dissertation held by the Author.

Microform Edition © ProQuest LLC.

All rights reserved. This work is protected against unauthorized copying under Title 17, United States Code



ProQuest LLC.  
789 East Eisenhower Parkway  
P.O. Box 1346  
Ann Arbor, MI 48106 - 1346

Abbott, Geoffrey R., Ph.D., Spring 2014

## **The Development and Study of Surface Bound Ruthenium Organometallic Complexes.**

Chairperson Dr. Edward Rosenberg, Department of Chemistry

### **Abstract**

The focus of this project has been on the use of mono-diimine ruthenium organometallic complexes, of the general structure  $[H(Ru)(CO)(L)_2(L')_2][PF_6]$  ( $L=PPh_3$ , DPPENE and  $L'=Bpy$ , DcBpy, MBpyC, Phen, AminoPhen) bound to surfaces as luminescent probes. Both biological and inorganic/organic hybrid surfaces have been studied. The complexes were characterized both bound and unbound using standard analytical techniques such as NMR, IR and X-ray crystallography, as well as through several photophysical methods as well.

Initially the study focused on how the photophysical properties of the complexes were affected by incorporation into biological membranes. It was found that by conjugating the probes to a more rigid cholesterol moiety that luminescence was conserved, compared to conjugation with a far more flexible lipid moiety, where luminescence was either lost or reduced. Both the cholesterol and lipid conjugates were able to insert into a lipid membrane, and in the more rigid environment some of the lipid conjugates regained some of their luminescence, but often blue shifted and reduced, depending on the conjugation site.

Silica Polyamine Composites (SPCs) were a hybrid material developed in the Rosenberg Lab as useful metal separation materials, that could be easily modified, and had several benefits over current commercially available polymers, or inorganic materials. These SPCs also provided an opportunity for the development of a heterogeneous platform for luminescent complexes as either catalysts or sensors. Upon binding of the luminescent Ru complexes to the surface no loss, or major change in luminescence was seen, however, when bound to the rigid surface a significant increase in excited state lifetime was measured. It is likely that through binding and interacting with the surface that the complexes lost non-radiative decay pathways, resulting in the increase in lifetime, however, these interactions do not seem to affect the energy level of the MLCT band in a large way.

With a better understanding of the effects of surface binding on the complexes, the study turned to possible applications, as either sensors or catalysts. Recently the bound complexes have been found to be very useful as toxic metal sensors, as the free amines left on the surface could bind toxic metal ions in close proximity leading to either a quenching or enhancement of the luminescence of the complexes, depending on the metal ion. This process was determined to be a static process, requiring the toxic metal to remain bound to the surface in order to affect the luminescence of the Ru complex. The quenching is thought to be due to a metal-centered electron-transfer reaction, in which the excited-state electron is transferred from the Ru to the toxic metal, but relaxes back to the Ru center. The enhancement of luminescence is due to the external heavy-atom effect, in which heavier atoms mixes MLCT singlet state with the triplet state through spin-orbit coupling.

## Acknowledgments

Difficult though it may have been, the last 5 years I have spent at the University of Montana and in the city of Missoula have been one of the greatest experiences of my life. I would like to thank all those who have helped make this valley in the middle of nowhere a home I will never forget. First and foremost a huge thanks to Ed Rosenberg who gave me the opportunity to work in his lab and has taught me more than I ever thought, inside the lab and out, a finer boss, and a better man, will be hard to find. I also have to thank Dr. Ayesha Sharmin, Dr. Jesse Allen, and Dr. Raj Kailasam, who were in the lab when I arrived and took the time to teach me even as they finished their own work, and became good friends in the process. Robert Brooks also deserves a great deal of thanks for his hard work and help bringing my projects to completion. To Riley McVey and Shelby, the high school students who I had the privilege of mentoring, I thank you for your hard work, and I hope that your drive to succeed in chemistry continues. To the rest of the Rosenberg lab past and present, thank you for all the memories. To the rest of the Chemistry Department, thank you for all the advice and help through classes and my research, it is amazing how much this building has come to seem like home thanks to you. I would like to thank Earle Adams especially for all his help, and patience, no matter how much bad news regarding instruments I brought him. With his help I have learned more about the technical aspects of instrumentation than I ever thought I would. To my family, your support has been the unwavering foundation on which I have stood for so long and helped me achieved so much. I know it has been difficult to be so far away but I want you to know that you have always been in my heart no matter the distance. To my friends, it has been an amazing experience to have gotten to know such a wonderful group of people. The times we've spent on the river, in the woods, and even those times we've forgotten in the bars, will hold a place in my heart forever. So to all of you again, thank you, Missoula has been the only place I've considered home since I left Kentucky and it is thanks to your friendship and support. So it is that I've come to realize that the reason Montana is the Treasure State is not because of its gold, and silver, but because the memories made here are a treasure that will last forever.

# Table of Contents

Abstract	ii
Acknowledgements	iii
Table of Contents	iv
List of Figures	ix
List of Charts and Tables	xi
List of Abbreviations	xiii
<b>Chapter 1. Background</b>	
<b>1.1 Introduction</b>	<b>1</b>
<b>1.2 Applications</b>	<b>7</b>
1.2.1 Bioconjugation	7
1.2.2 Metal Sensing	8
1.2.3 Catalysis	9
1.2.3.1 Thermal Catalysis	9
1.2.3.2 Photocatalysis	10
<b>1.3 Family of Ruthenium Complexes</b>	<b>11</b>

1.3.1 Comparison of Commercially Available Probes	12
---	----

## **Chapter 2. Bioconjugation of Ruthenium Mono-diimine Complexes to Cholesterol and Lipids for use as Luminescent Probes in Phospholipid Membranes**

<b>2.1 Introduction</b>	<b>14</b>
<b>2.2 Results</b>	<b>18</b>
2.2.1 Synthesis	18
2.2.2 Photophysical Characterizations of Complexes 1-5, 6', and 7-10	24
2.2.3 Photophysical Studies of Complexes 3-5, 7, 9, and 10 Incorporated into Lipid Membrane Bilayers	26
2.2.4 Ligand Lability	38
<b>2.3 Experimental</b>	<b>40</b>
2.3.1 General Methods and Materials	40
2.3.2 Synthesis of $[(H)Ru(CO)(PPh_3)_2(dcbpy-N-succinimidyl)]PF_6$ (1')	41
2.3.3 Synthesis of $[(H)Ru(CO)(PPh_3)_2(dcbpy-N-DPPE_2)]PF_6$ (3)	41
2.3.4 Synthesis of $[(H)Ru(CO)(dppene)(1,10-phen-5-NCS)]PF_6$ (2')	42
2.3.5 Synthesis of $[(H)Ru(CO)(dppene)(1,10-phen-5-NHC(S)-N-DPPE)]PF_6$ (4)	42
2.3.6 Synthesis of $[(H)Ru(CO)(dppene)(1,10-phen-5-NHC(O)OChol)]PF_6$ (5) (Chol = cholesteryl).	43
2.3.7 Synthesis of $[(TFA)_2Ru(CO)_2(PPh_2C_2H_4C(O)OH)]$ (TFA = Trifluoroacetic Acid)(6)	44
2.3.8 Synthesis of $[(H)Ru(CO)(PPh_2C_2H_4C(O)OH)_2(bpy)]PF_6$ (6')	44
2.3.9 Synthesis of $[(H)(CO)Ru(PPh_2C_2H_4C(O)-N-succinimidyl)_2(bpy)]PF_6$ (6'')	44
2.3.10 Synthesis of $[(H)(CO)Ru(PPh_2C_2H_4C(O)-N-DPPE)_2(bpy)]PF_6$ (7)	45
2.3.11 Synthesis of $[Ru(bpy)_2(1,10-phen-5-NHC(O)OChol)]PF_6$ (9)	45

2.3.12 Synthesis of trans-[Ru(CO)(DPPENE) <sub>2</sub> (TFA)][PF <sub>6</sub> ] (13)	46
2.3.13 LUV Preparation	46

## **Chapter 3. Silica Polyamine Composite Technology on the Nanoscale**

<b>3.1 Introduction</b>	<b>48</b>
<b>3.2 Results</b>	<b>49</b>
3.2.1 Composite Nomenclature	49
3.2.2 Synthesis	49
3.2.3 NMR, Elemental Analysis and Copper Capacity	50
3.2.4 Catalysis	56
<b>3.3 Materials and Methods</b>	<b>59</b>
3.3.1 Materials	59
3.3.2 Methods	60
3.3.3 Synthesis	60
3.3.3.1 Synthesis of 3-aminopropyl coated microparticles (MAP)	60
3.3.3.2 Synthesis of 3-aminopropyl coated nanoparticles. (NAP)	60
3.3.3.3 Synthesis of 3-Chloropropyltrimethoxysilane coated nanoparticles	61
3.3.3.4 Synthesis of 7:1 Methyltrimethoxysilane to 3-Chloropropyltrimethoxysilane coated nanoparticles	61
3.3.3.5 Synthesis of WP-1 nanoparticles (NPE)	61
3.3.3.6 Synthesis of BP-1 nanoparticles (NPA)	62

## **Chapter 4. Studying the Effects of Surface Properties on the Photophysical Properties of Ruthenium Mono-diimine Complexes Bound to SPCs**

<b>4.1 Introduction</b>	<b>63</b>
-------------------------	-----------



<b>4.2 Results</b>	<b>66</b>
4.2.1 Synthesis	66
4.2.2 IR, NMR, and Solid-State NMR(SSNMR)	71
4.2.3 Loading	76
4.2.4 Luminescent Studies	77
4.2.5 Lifetime Measurements	81
4.2.6 CO Exchange and Orthometallation	87
<b>4.3 Experimental</b>	<b>90</b>
4.3.1 Materials	90
4.3.2 Methods	90
4.3.2.1 Spectroscopic Measurements	90
4.3.2.2 Metal Analysis	91
4.3.2.3 Excited State Lifetime Measurements	91
4.3.3 Synthesis	92
4.3.3.1 Synthesis of <i>trans</i> -[(H)Ru(CO)(4'-methyl-2,2'-bipyridine-4-carbaldehyde)(PPh <sub>3</sub> ) <sub>2</sub> ][PF <sub>6</sub> ] (12) and <i>trans</i> -[(H)Ru(CO)(4'-methyl-2,2'-bipyridine-4-ethylene glycol acetal)(PPh <sub>3</sub> ) <sub>2</sub> ][PF <sub>6</sub> ] (12')	92
4.3.3.2 General procedure for coupling of complexes 1 and 6' to the composites with HBTU: <sup>1,2</sup> Synthesis of MPA-1, MPE-1, MPA-6', MAP-6', NPA-1, NPA-6'	94
4.3.3.3 General Procedure for coupling complexes 2 and 8 to the composites via the isothiocyanate intermediate: <sup>3,4</sup> synthesis of MPA-2, MPE-2, MPA-8, NPA-2	95
4.3.3.4 General procedure for the coupling of complex 12 to the composites by direct reaction with the composites: synthesis of MPA-12, MPE-12 and NPA-12	96
4.3.3.7 Orthometallation Procedure in Solution	97

**Chapter 5. Applications of Surface Bound Ruthenium Complexes**

<b>5.1 Introduction</b>	<b>99</b>
<b>5.2 Results</b>	<b>100</b>
5.2.1 Metal Sensing	100
<b>5.3 Methods</b>	<b>102</b>

**Chapter 6 Conclusions and Future Work**

<b>6.1 Conclusions</b>	<b>104</b>
6.1.1 Bioconjugation of Ruthenium Complexes	104
6.1.2 SPC Nanomaterials	105
6.1.3 Binding of Ruthenium Complexes to SPCs	106
6.1.4 Applications of SPC Bound Ruthenium Complexes	107
<b>6.2 Future Work</b>	<b>108</b>
6.2.1 Optimization	108
6.2.1.1 Loading	108
6.2.1.2 Metal Sensing	109
6.2.1.3 Catalysis	109
6.2.1.4 Metal Sensing Selectivity	110

<b>Bibliography</b>	<b>111</b>
---------------------	------------

<b>Appendix A</b>	<b>116</b>
-------------------	------------

<b>Appendix B</b>	<b>127</b>
-------------------	------------

## List of Figures

<b>Figure 1: Scale of Scientifically Important Compounds</b>	<b>1</b>
<b>Figure 2: SPC's Coated with Luminescent Complexes</b>	<b>2</b>
<b>Figure 3: Cholesterol and Lipid Conjugated Ru-Complexes</b>	<b>7</b>
<b>Figure 4: Diagram of a Fluorionophore and Design Principles</b>	<b>8</b>
<b>Figure 5: General Catalytic Scheme</b>	<b>9</b>
<b>Figure 6: General Photocatalytic Scheme</b>	<b>10</b>
<b>Figure 7: Common Ru Tris-Diimine Probes</b>	<b>12</b>
<b>Figure 8: Emission Spectra for Compounds (1) and (2)</b>	<b>24</b>
<b>Figure 9: Absorption and Emission Spectra for Compounds (5) and (9)</b>	<b>25</b>
<b>Figure 10: Emission Spectra for Compounds (3) and (4) in Liposomes</b>	<b>28</b>
<b>Figure 11: Temperature Dependence of Compound (5) Lifetime in Liposomes</b>	<b>31</b>
<b>Figure 12: Representation of Bioconjugated Ru-Complexes in a Liposome</b>	<b>37</b>
<b>Figure 13: Crystal Structure of Compound (13)</b>	<b>39</b>
<b>Figure 14: <math>^{13}\text{C}</math> SS-NMR of MAP</b>	<b>50</b>
<b>Figure 15: <math>^{29}\text{Si}</math> SS-NMR Comparison of MAP and NAP</b>	<b>51</b>
<b>Figure 16: <math>^{29}\text{Si}</math> SS-NMR of 7:1 MTMS:CPTMS Coated Nanoparticles</b>	<b>53</b>
<b>Figure 17: <math>^{29}\text{Si}</math> and <math>^{13}\text{C}</math> SSNMR of 7:1 MTMS:CPTMS nanoparticles reacted with PAA</b>	<b>54</b>
<b>Figure 18: IR Comparison of Compound (1) and MPA-1</b>	<b>71</b>

<b>Figure 19: <math>^{31}\text{P}</math> SS-NMR of MPA-2</b>	<b>73</b>
<b>Figure 20: <math>^{29}\text{Si}</math> NMR Comparing Bulk and Surface Silanes</b>	<b>74</b>
<b>Figure 21: SSNMR of Before and After Reaction of NAP with Complex (2)</b>	<b>75</b>
<b>Figure 22: Graph of Complex Loading on Micro and Nano particles</b>	<b>76</b>
<b>Figure 23: Graph of Optimal Loading levels for NPA-6'</b>	<b>77</b>
<b>Figure 24: Absorption Spectra for Compound (1) and MPA-1</b>	<b>79</b>
<b>Figure 25: Emission and Excitation of Compound (6') and MPA-6'</b>	<b>79</b>
<b>Figure 26: Close Packed Sphere Models of Compounds (1), (2) and (9)</b>	<b>82</b>
<b>Figure 27: Lifetime Curve for MPA-1</b>	<b>87</b>
<b>Figure 28: Reaction Mechanism for Orthometallation of Compound (1)</b>	<b>88</b>
<b>Figure 29: <math>^{13}\text{C}</math> NMR of Compound (1) Before and After Orthometallation</b>	<b>88</b>
<b>Figure 30: <math>^{13}\text{C}</math> SS-NMR of MPA-1 Before and After Orthometallation</b>	<b>89</b>
<b>Figure 31: Graph of Emission Changes of MPA-1 After Treatment with a Metal Ion Solution</b>	<b>100</b>
<b>Figure 32: Stern-Volmer Plot of MPA-1 Soaked in <math>\text{Cu}^{2+}</math> Solution</b>	<b>101</b>
<b>Figure 33: Comparison of Excitation Spectra of MPA-1 Before and After Soaking with <math>\text{Cu}^{2+}</math></b>	<b>102</b>

## List of Tables, Charts and Schemes

<b>Scheme 1: Synthesis of SPCs</b>	<b>6</b>
<b>Table 1: Structures of Studied Ruthenium Complexes</b>	<b>11</b>
<b>Scheme 2: Bioconjugation of Compound (1) to a Lipid</b>	<b>17</b>
<b>Scheme 3: Bioconjugation of Compound (2) to Cholesterol and Lipid</b>	<b>19</b>
<b>Scheme 4: Bioconjugation of Compound (6) to a Lipid</b>	<b>20</b>
<b>Table 2: Absorption, emission, and excited-state lifetimes of ruthenium MLC probes in ethanol.</b>	<b>23</b>
<b>Table 3: Average Lifetime, limiting anisotropy and rotational correlation times for complexes 3 and 4 in egg-PC LUVs (100 nm) from 5–50°C.</b>	<b>29</b>
<b>Table 4: Average lifetime, limiting anisotropy and rotational correlation times for complex 5 at a range of temperature in 100-nm egg-PC LUVS.</b>	<b>33</b>
<b>Chart 1: Definition of T and Q peak in <sup>29</sup>Si SSNMR</b>	<b>51</b>
<b>Table 5: Comparison of the Properties of Micro and Nano- SPCs</b>	<b>52</b>
<b>Table 6: Anchor Points and Copper Capacities for Micro and Nano- SPCs</b>	<b>55</b>
<b>Table 7: Variation in Copper Capacities for Nano SPCs made with PEI (MW=300-25K)</b>	<b>56</b>
<b>Scheme 5: Knoevenagel Catalytic Cycle</b>	<b>57</b>
<b>Table 8: Second Order Rate Constants for the SPC Catalyzed Knoevenagel Reaction</b>	<b>60</b>
<b>Chart 2: Structures of Ruthenium Complexes Studied</b>	<b>64</b>
<b>Scheme 6: Hydride Formation for Complex 1</b>	<b>66</b>

<b>Scheme 7: Coupling of Compound (1) to BP-1</b>	<b>67</b>
<b>Scheme 8: Coupling of Compounds (2) and (9) to BP-1</b>	<b>69</b>
<b>Scheme 9: Coupling of Compounds (12) and (12') to BP-1</b>	<b>70</b>
<b>Table 9: Comparison of Emission Maxima for Complexes in Solution and on BP-1</b>	<b>78</b>
<b>Table 10: Comparison of Lifetimes for Complexes in Solution and on BP-1 Microparticles</b>	<b>81</b>
<b>Scheme 10: Lifetime Comparisons of Complex 2 on Different Surfaces</b>	<b>84</b>
<b>Table 11: Comparison of Lifetimes for Complexes on Different Microparticle Surfaces</b>	<b>84</b>
<b>Table 12: Comparison of Lifetimes for Complexes in Solution and Complexes on BP-1 Nanoparticles</b>	<b>86</b>

## List of Abbreviations

<b>AA</b>	<b>Atomic Absorption</b>
<b>AP</b>	<b>5-amino-1,10-phenanthroline</b>
<b>BP-1</b>	<b>Polyallylamine Coated Particles</b>
<b>Bpy</b>	<b>2,2'-bipyridyl</b>
<b>Chol</b>	<b>Cholesterol</b>
<b>CPTCS</b>	<b>3-Chloropropyl Trichlorosilane</b>
<b>CPTMS</b>	<b>3-Chloropropyl Trimethoxysilane</b>
<b>DcBpy</b>	<b>4,4'-Dicarboxy-2,2'-Bipyridyl</b>
<b>DPPE</b>	<b>1,2 dihexadecanoyl-sn-glycero-3-phosphoethanolamine</b>
<b>DPPENE</b>	<b>cis-1,2-Bis(diphenylphosphino)ethylene</b>
<b>EPR</b>	<b>Electron Paramagnetic Resonance</b>
<b>HBTU</b>	<b>O-(Benzotriazol-1-yl) N,N,N',N'-tetramethyluronium hexafluorophosphate</b>
<b>IR</b>	<b>Infrared</b>
<b>MAP</b>	<b>Microscale Particles Coated with 3-Aminopropyl Trimethoxysilane</b>
<b>MBpyC</b>	<b>4-methyl-2,2'-Bipyridyl-4'-carbaldehyde</b>
<b>MLCT</b>	<b>Metal to Ligand Charge Transfer</b>
<b>MPA</b>	<b>Microscale Particles Coated with Polyallylamine</b>

<b>MPE</b>	<b>Microscale Particles Coated with Polyethyleneimine</b>
<b>MTCS</b>	<b>Methyl Trichlorosilane</b>
<b>MTMS</b>	<b>Methyl Trimethoxysilane</b>
<b>NAP</b>	<b>Nanoscale Particles Coated with 3-Aminopropyl Trimethoxysilane</b>
<b>NMR</b>	<b>Nuclear Magnetic Resonance</b>
<b>NPA</b>	<b>Nanoscale Particles Coated with Polyallylamine</b>
<b>NPE</b>	<b>Nanoscale Particles Coated with Polyethyleneimine</b>
<b>PAA</b>	<b>Polyallylamine</b>
<b>PEI</b>	<b>Polyethyleneimine</b>
<b>Ph</b>	<b>Phenyl</b>
<b>Phen</b>	<b>1,10-phenanthroline</b>
<b>SEM</b>	<b>Scanning Electron Microscope</b>
<b>SPC</b>	<b>Silica Polyamine Composite</b>
<b>SSNMR</b>	<b>Solid State Nuclear Magnetic Resonance</b>
<b>TFA</b>	<b>Trifluoroacetic Acid</b>
<b>TEM</b>	<b>Tunneling Electron Microscope</b>
<b>WP-1</b>	<b>Polyethyleneimine Coated Particles</b>



# Chapter 1. Background

## 1.1 Introduction

As science has advanced it has moved from processes that could be monitored by the human eye down to the interactions of single atoms. Between these extremes though lies an area which has been difficult to study, the gray area where the molecules are too small to be seen by normal light microscopy, yet too large to be easily analyzed by single atom methods such as NMR or mass spectrometry. This range is where proteins, membranes and more complex chemical polymers lie. As is shown in Figure 1, the range of low  $\mu\text{m}$ -nm is where things such as blood cells, and proteins will lie and while there are techniques for imaging these structures, these imaging techniques give too wide a view to understand all the processes going on at the molecular level. To measure the processes happening on the surface of these systems a secondary form of measurement is needed, that is where luminescent probes come in.

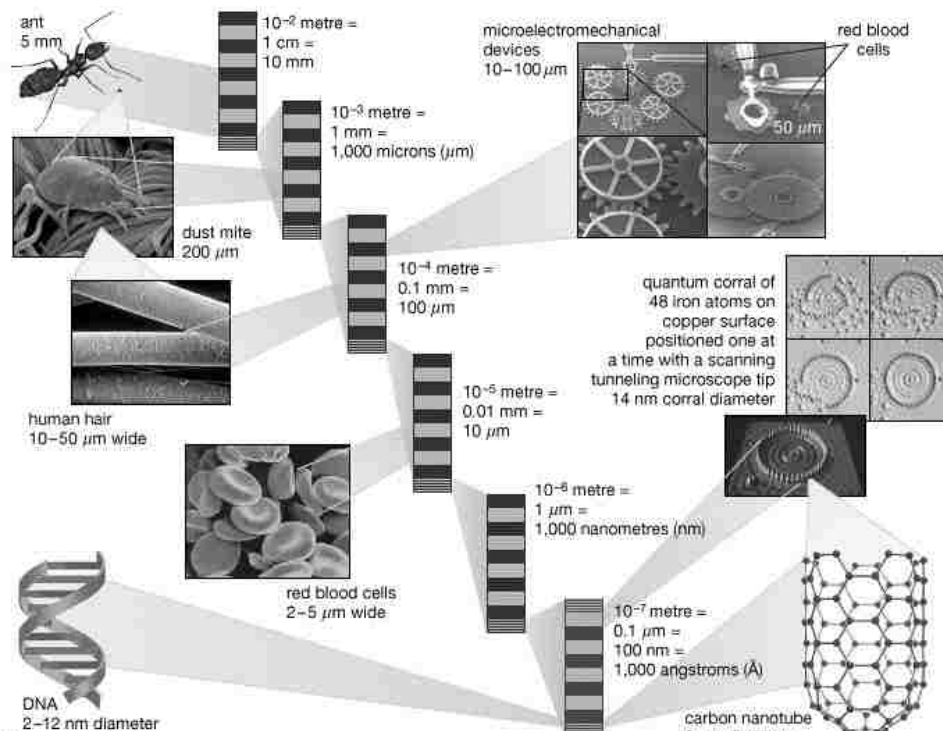


**Figure 1 Representation of the changes in scale of scientifically important compounds**

Luminescence has become a powerful tool in the study of many biological as well as chemical systems. The use of emitted light from chemical probes allows for a variety of measurements to be made using only a single properly designed probe. Intensity can be used to gather information on concentrations or the timescale of chemical reactions, while the emitted light can be tracked through physical space to better understand the motions of larger materials.<sup>3,5-18</sup>

Along with biological systems luminescent probes are also useful in the characterization of chemical surfaces as well.<sup>11,12,19-22</sup> The changes a surface can cause in the photophysical properties of a luminescent molecule can give information regarding the chemical and physical environments present on a surface (Figure 2).<sup>20-22</sup> A better understanding of the interaction between probe and surface can lead to several new and important discoveries and processes, such as using the interaction of probes on a surface to increase or decrease light intensity on a solar cell to increase efficiency.<sup>23,24</sup>

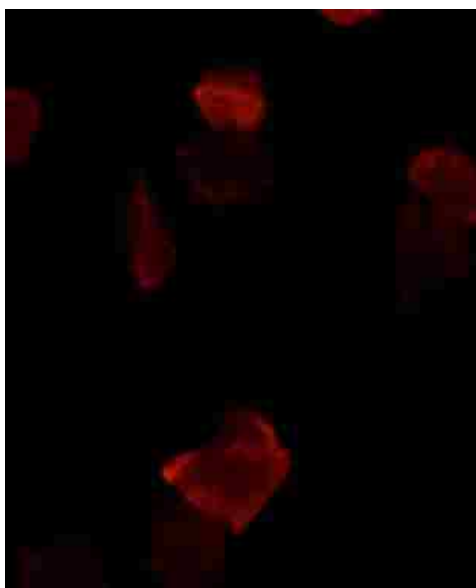


**Figure 2 Image of coated, Silica Polyamine Composite (SPC), particles illustrates how direct viewing of luminescence can show heterogeneity on the surface. (Brighter areas represent higher loading of complex)**

Luminescent spectroscopy is also a very important tool, because it is not only sensitive, it is low cost and quick.<sup>25</sup> The cost and speed with which luminescent studies can be done allow for a much higher and quicker throughput of samples meaning that samples that need further study can be more efficiently identified. The development of probes that are capable of binding and providing chemical and physical details across a variety of surface types further increases this efficiency as only a single probe needs to be synthesized instead of one per material.

In the course of designing luminescent probes for the study of systems that are difficult to study by other means, a variety of factors must be taken into account.<sup>3,5,26-29</sup> One of the biggest factors is stability, chemical and electronic, and depending on the systems being studied this can be difficult to incorporate into probe design. When studying the environment of a system, say a surface, the stability of a probe cannot be so great that it behaves the same in every environment, it needs to be able to interact and change based on the environment, yet still be stable enough to provide information.

Another key factor is the quantum yield of a luminescent probe which is the amount of light a probe emits based on how much light it absorbs. The need for high quantum yields is due to the fact that often, when adding a probe to a system, the very fact that a new compound is introduced to a system can induce changes. While probes are often relatively small compared to the system being studied, high quantum yields allow for measurements to be made with fewer probes, meaning that the behavior of the system is less likely to be affected.

Perhaps the most considered factors are the photophysical properties, absorption wavelengths, emission wavelengths, and excited state lifetimes, because it is usually much easier to design a probe around these properties than stability and quantum yield. So while the stability and quantum yield of a probe are very important they are often secondary considerations, with

the other photophysical properties being the driving force in the design. These properties are easily controlled by the use of ligands and functional groups and are usually designed specifically for the system being studied.

Beyond the three factors listed above there are many other factors, such as anchoring motif, that need to be considered as well. These factors depend even more than the photophysical properties on the system being studied. While the design of a probe for a simple system can be relatively straightforward, as the complexity and number of systems being studied increases, so does the difficulty of creating a probe that can be used across a variety of systems.

In recent years, there has been an increase both in academia and the chemical industry to understand and use more and more complex systems. In order to probe these larger, more complex systems new compounds must be developed.<sup>6,9,10,27,30</sup> These compounds must be robust enough to handle a variety of environments while still being able to be measured using standardized techniques. Ruthenium complexes have been a common choice for use as probe molecules. The fact that ruthenium probes use a metal to ligand charge transfer (MLCT) band which tends to have a large Stokes shift allow them to have reduced self-quenching and to emit a wavelength that is less harmful to biomolecules. Ruthenium based complexes are also versatile in their chemistry with the ability to use many different ligands which can affect their luminescent properties, as well as make them robust enough to stand up to a variety of environments.

Beyond their use as luminescent probes ruthenium complexes are known catalysts for several types of important reactions.<sup>31-36</sup> Ruthenium complexes have been shown to be efficient catalysts for dehydrogenation, hydrogenation, transfer hydrogenation and olefin metathesis reactions depending on the ligands associated with the metal center. The robustness and

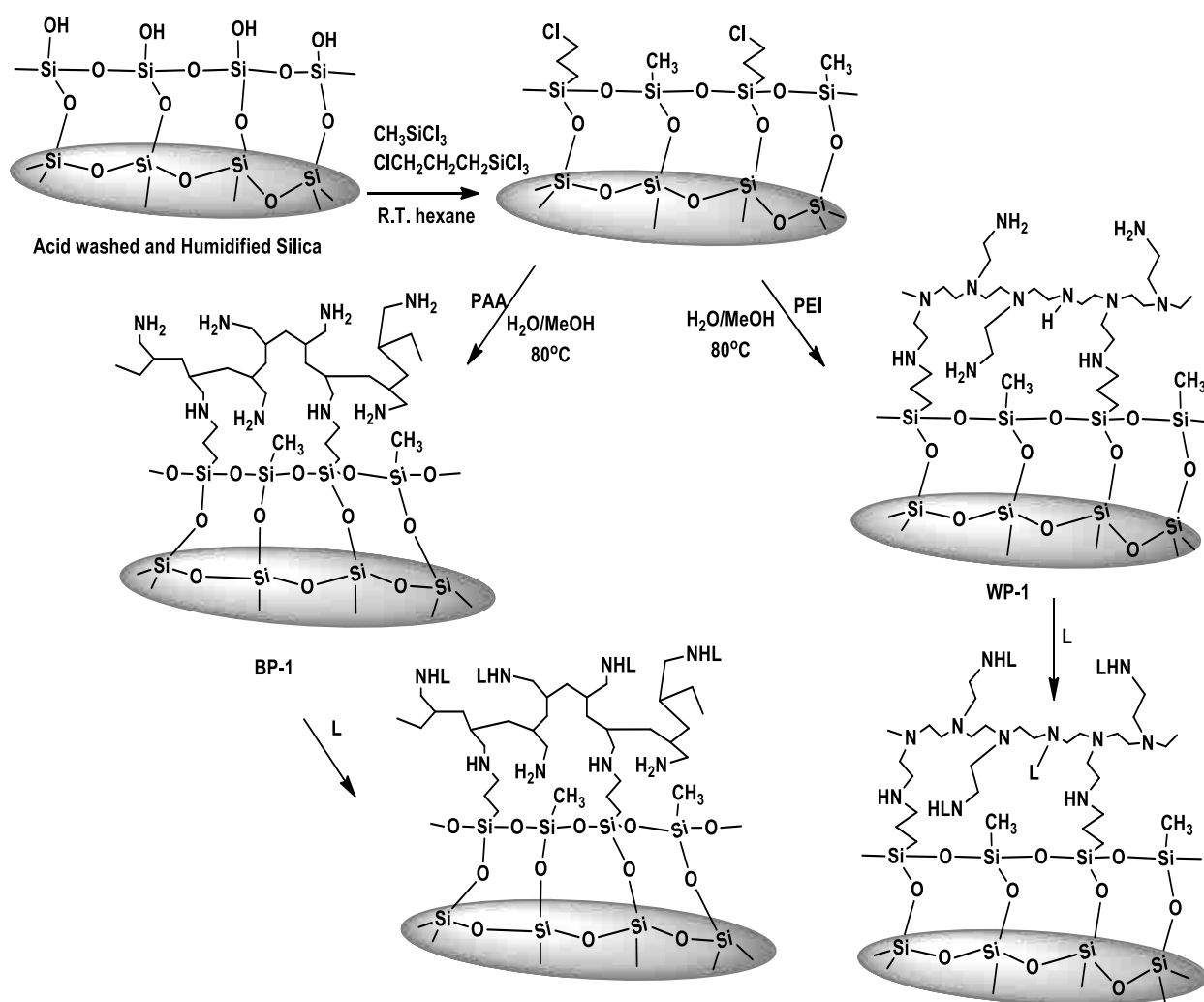
adaptability of ruthenium complexes makes them very strong candidates for not only photophysical studies but also as heterogeneous catalysts when bound to a surface.<sup>31,35,37-39</sup>

One area where probes and catalysts have become an increasingly important tool is in the field of surface chemistry because more and more chemical and industrial processes are moving towards heterogeneous processes. Heterogeneous chemistry has long been less efficient chemically but more efficient with regards to the physical separation of products. As surface chemistry has become better understood the design of materials and their efficiency in a wide range of reactions has improved to the point they are often now more commercially viable than homogeneous methods, because of the reduced cost of separation from the product mixture.

Most heterogeneous chemistry relies on a large stable support to anchor active complexes to, in order to provide the volume necessary for easy physical separation. Surfaces like amorphous silica, SiO<sub>2</sub>, and alumina, Al<sub>2</sub>O<sub>3</sub>, are common choices, as they are readily available and low cost. Polymers such as polystyrene are another common support system for heterogeneous chemistry. Both systems have their advantages, polymers can be synthesized to contain almost any functional group needed, but they suffer from shrink swell issues with changes in pH and temperature. While inorganic substrates such as silica and alumina do not suffer from shrink swell issues, they have a more limited chemistry and are easily dissolved at high pH.

Silica Polyamine Composites (SPCS's) are a new hybrid composite, designed to be both commercially and environmentally useful.<sup>40-59</sup> SPCs are an inorganic silica platform that has been coated with an amine based polymer, the goal in developing these materials was to design a matrix that had the mechanical stability of an inorganic material with the flexibility in modification of a polymer, the best of both worlds.

SPC synthesis, shown in Scheme 1, starts with an amorphous silica particle that has been humidified to create a monolayer of water on the surface. This hydrated surface is then reacted with a mixture of 3-chloropropyltrichlorosilane and methyltrichlorosilane, at a 1:7.5 ratio, to create anchor points for the polymer. The surface is then reacted with one of two amine based polymers, polyallylamine(PAA) is a linear polymer composed of primary amines, or polyethyleneimine(PEI), a branched polymer which contains primary, secondary and tertiary amines.



Scheme 1

SPCs were designed originally for metal capture and separation and have been well characterized and even commercialized for those applications (Johnson-Matthey Ltd has licensed this technology from the University of Montana). SPC's though, have the possibility to be used for a variety of heterogeneous processes such as catalysis and metal sensing. In order to understand how SPCs will affect more complex chemical reactions a more complete understanding of how the surface interacts with molecules is necessary.

## 1.2 Applications

### 1.2.1 Bioconjugation

A growing field in which luminescent probes are becoming more and more important is biophysics.<sup>4,5,7-10,13-15,29,60-64</sup> In the case of biological systems there is a certain scale at which normal visual methods, i.e. light microscopy are no longer viable, while methods that measure smaller scales, i.e. NMR, and EPR<sup>65</sup> become complicated when examining these larger biomolecular structures. There are methods capable of elucidating structures at these scales such as SEM and TEM and X-ray crystallography, however, these are static measurements, meaning that only a single structure can be measured, not a dynamic process.

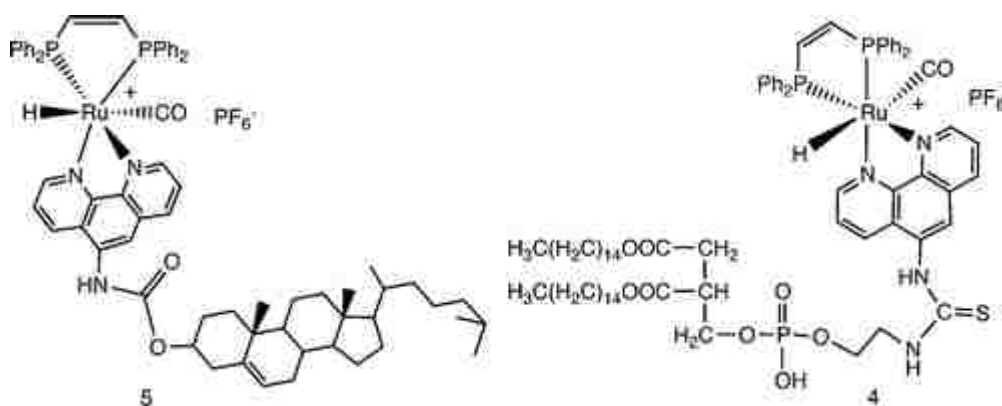


**Figure 3 Two Bioconjugated ruthenium probes for study of model biological membranes**

The use of luminescent probes allows for the measurement of dynamic processes of structures of varying size. Chemical probes also allow for the specific measurement of certain regions of larger biomolecules by being synthesized to only bind to a specific chemical motif<sup>30,65-67</sup> (Figure 3). This can allow for the independent measurement of different regions of a complex system without having to synthesize multiple luminescent probes.

### 1.2.2 Metal Sensing

Luminescent probes are also useful for the detection of many different chemicals and biomolecules. Many probes undergo changes in some of their photophysical properties in the presence of metal impurities, primarily quenching of luminescence.<sup>11,26</sup> The level of quenching can be dependent not only on the concentration of the metal but also on which metal it is and the design of the probe meaning that the process can be made selective and able to identify individual contaminants. Figure 4 shows the considerations that must be taken into account

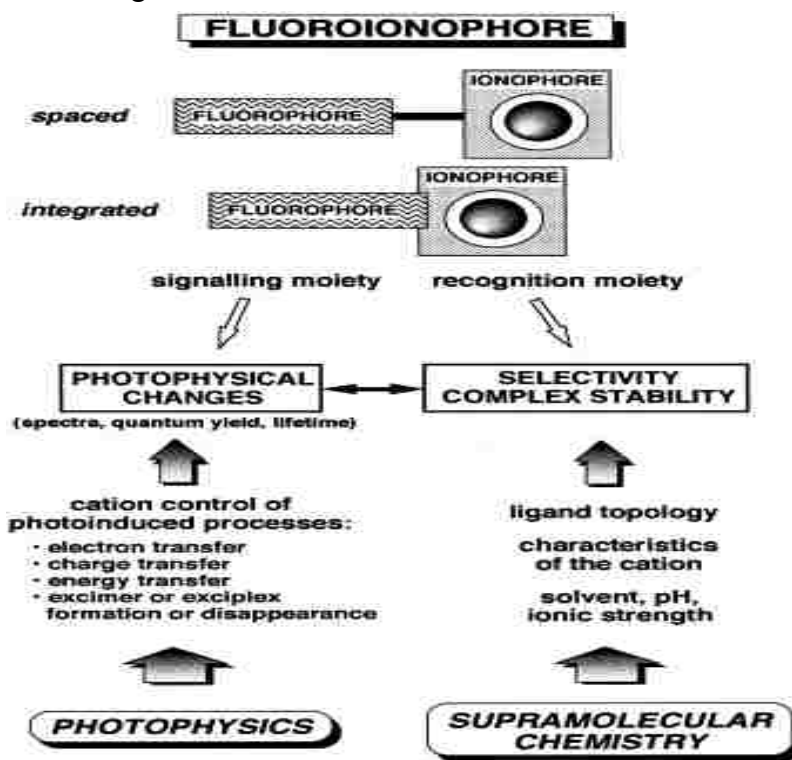


Figure 4 Factors to consider when using a luminescent probe to detect metal species.<sup>23</sup>



when designing what Valeur et al. call fluoroionophores<sup>26</sup>, which are a luminescent complex, the fluorophore, that contains a binding site for a cationic species, the ionophore. The interaction between the ionophore and the fluorophore induce a change that can be detected between the bound and unbound state of the ionic species. These same principles apply to using surface bound probes as the distance between the binding sites for the luminescent probes and the ionic species being measured must be considered as well as the selectivity of the surfaces binding sites.

One reason luminescent probes should be considered as a viable technology for metal sensing is that electronic spectroscopy is a quick and cheap experimental method. While light spectroscopy can lack the sensitivity and range of some more complex methods, the rate at which samples can be processed is much higher. The other advantage to using electronic spectroscopy is that the technology is much more portable than that of other systems, meaning that measurements could be taken on sight of a possible contamination.

### 1.2.3 Catalysis

#### 1.2.3.1 Thermal Catalysis

Many luminescent organometallic complexes have also been used as catalysts for a wide variety of reactions depending upon the complex's central metal and ligands<sup>31-34,36,68</sup>. These

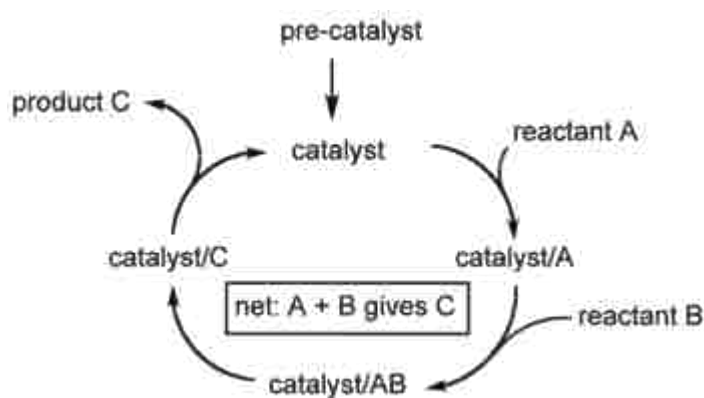


Figure 5 General catalytic scheme.

complexes are most often used as thermal catalysts, in which the luminescent properties are a secondary feature. The primary features when using a complex as a thermal catalyst are the geometry and electronic structure of the complex. The design of the catalyst is then often based on the type of reaction being catalyzed and the products being formed. Still, even though the photophysical properties do not play a direct role in the catalytic reaction they can be used to monitor the state and quality of the catalyst.

### 1.2.3.2 Photocatalysis

Luminescent organometallic complexes can also be used in order to take advantage of their photophysical properties to enhance their catalytic effectiveness or to widen the variety of reactions they can catalyze<sup>69,70</sup>. When using complexes as photocatalysts the photophysical properties become a primary concern. The properties often controlled are the energy level at which the complex absorbs/emits light, and the excited state lifetime of the electrons.

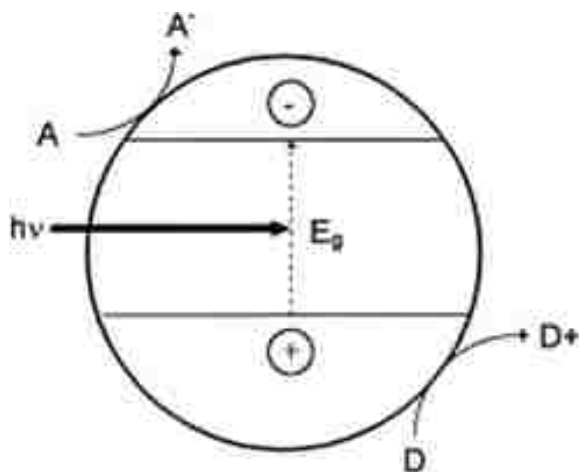


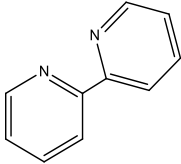
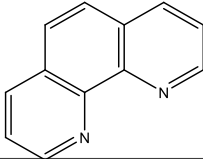
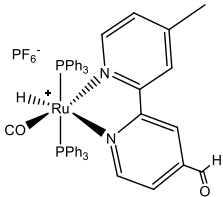
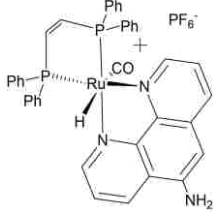
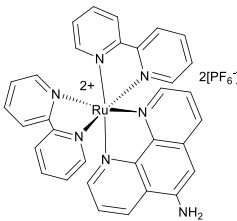
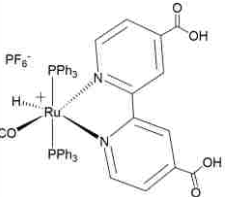
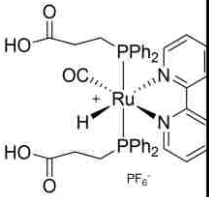
Figure 6 General scheme for photo catalysis

This type of catalysis can be very useful because the external energy being put into the reaction is more focused. With thermal catalysis the energy comes from the heat being applied, which is over a wide range of energies, this can lead to more side reactions or unwanted processes having the energy to proceed. With photocatalysis the energy being put into the

reaction is a narrow wavelength that is absorbed by the target molecule and not the system as a whole, meaning that the chance of side reactions is more limited. As shown in, Figure 6, the luminescent complex is irradiated at a specific energy which excites an electron to a higher state. In this excited state the lone electron is much more available for reactions due to its higher energy, in this case Compound A comes and takes up the electron and is reduced. This leaves the luminescent complex in an oxidized state which means it is now available to take an electron from Compound D, which is then in an oxidized state and can go on to do further reactions while the luminescent catalyst is regenerated. Also, photoexcited electrons can be used in stoichiometric reductions as in photopromoted electrochemistry

### 1.3 Family of Ruthenium Complexes

**Table 1 Structures of Studied Ruthenium Complexes**

Luminophore	Bipyridyl	Phenanthroline	Combination
			
Single Anchor			
Double Anchor			

As stated earlier ruthenium complexes have long been used, due in part to their variety and robustness, as luminescent probes<sup>3,13-15,67</sup>. They are also well known catalysts for a variety of reactions which can be controlled by using specific ligands.<sup>31,34,36</sup> The family of ligands

chosen for this research are a series of bis-phosphine mono-diimine ruthenium complexes with the general formula  $[\text{HRu}(\text{CO})(\text{L})_2(\text{L}')][\text{PF}_6^-]$  or  $[\text{HRu}(\text{CO})(\text{L})(\text{L}')][\text{PF}_6^-]$  where  $\text{L} = \text{PPh}_3$ ,  $\text{P}(\text{Ph})_2\text{CH}_2\text{CH}_2\text{COOH}$ ,  $n\text{-(Ph)}_2\text{PCH}_2\text{CH}_2\text{P}(\text{Ph})_2$  and  $\text{L}' = n\text{-[C}_{10}\text{H}_8\text{N}_2(\text{COOH})_2]$ ,  $n\text{-[C}_{10}\text{H}_8\text{N}_2(\text{CH}_3)(\text{OHC})]$ ,  $n\text{-[C}_{10}\text{H}_{10}\text{N}_2]$ ,  $n\text{-[C}_{12}\text{H}_7\text{N}_2(\text{NH}_2)]$ . This family of compounds was chosen because they contain various luminophores, as well as various functional groups which can be used to further modify these probes by connection to larger systems such as biomolecules and polymer surfaces<sup>3</sup>.

### 1.3.1 Comparison of Commercially Available Probes

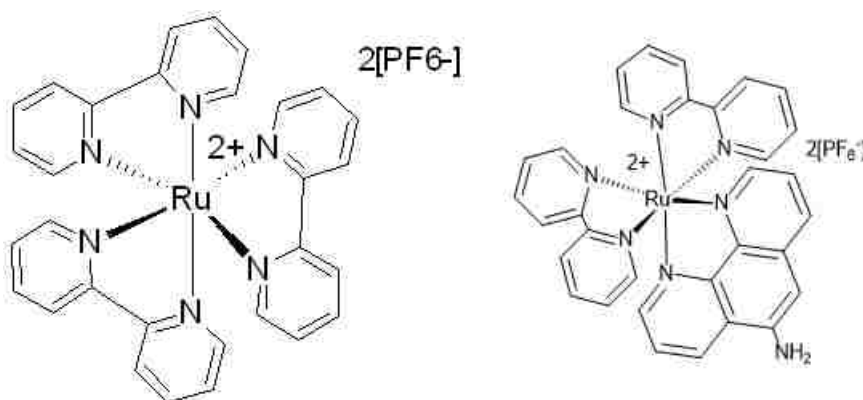


**Figure 7** Examples of 2 currently available tris-diimine luminescent probes

The most commonly used ruthenium in recent years has been  $\text{Ru}(\text{bpy})_3^{2+}$  and other such tris-diimines, like  $\text{Ru}(\text{bpy})_2(\text{phen})^{2+}$  developed by J.R. Lakowicz.<sup>29,30,60,67,71-73</sup> These probes exhibit long excited state lifetimes which allow for the study of slower molecular processes. The shortfall of many of these types of probes is their low quantum yield, a factor which can be improved through the addition of phosphine ligands such as those used in the previously described family of complexes. Tris-diimine probes also have low anisotropy due to their relatively high degrees of symmetry, meaning that when they are excited by polarized light, the light that they emit is more isotropic in intensity with respect to the parallel and perpendicular planes of the incident light. Anisotropy is important in the study of proteins because if a

luminescent complex has high anisotropy then the loss of polarized emission can be attributed to rotation of the whole protein-probe complex rather than just randomized emission. By replacing some of the ligands and using only a single diimine, the family of probes in this research have a much higher anisotropy which is very useful in the study of rotational movements of large molecular structures<sup>32</sup>. Another benefit to the use of a single diimine is the coordination of labile ligands in the remaining two to four coordination sites. Tris-diimine complexes have ligands that are non-labile which reduces their catalytic abilities, making them more useful as photocatalysts, while the single diimines complexes can catalyze reactions both photolytically and thermally.

The strengths of tris-diimine complexes are that there are multiple luminophores on the complex often of only 1 or 2 different types. This means that their photophysical properties are more stable and less likely to be affected by different environments<sup>35</sup>. This is useful when attempting to study the motions of a surface, as the complex is less likely to lose its luminescence. However the stability of the photophysical properties make tris-diimine ligands poor molecules to use to actually study the surface. If the photophysical properties are stable across a variety of surfaces using these probes will not allow for the detection of changes in the surfaces.

## **Chapter 2 Bioconjugation of Ruthenium Mono-diimine Complexes to Cholesterol and Lipids for use as Luminescent Probes in Phospholipid Membranes**

### **2.1 Introduction**

The objective of this study is to synthesize probes suitable for incorporation into biological membranes for membrane dynamics measurements. To achieve this objective, we have synthesized a series of luminescent probes derived from ruthenium- based metal complexes that are tethered either to lipids or to cholesterol and have long excited-state lifetimes and low molecular symmetry. The diffusion dynamics of proteins and protein assemblies that associate with membrane bilayers are slow, on a time scale of microseconds and longer, compared to the rotational diffusion of proteins in solution, which occurs on a time scale of several to tens of nanoseconds.<sup>4</sup> For example, the correlation times of the rotational motions of membrane-bound proteins can be microseconds to milliseconds.<sup>29,61-63</sup> The difference in time scales for these dynamical processes (microseconds versus tens of nanoseconds) is the result of interactions between the proteins and the membrane lipids. The fluorescence probes most useful for studying protein dynamics in solution have excited-state lifetimes in the range of 5–30 ns. Longer excited-state lifetimes are needed to measure the dynamics of biomacromolecules on or in membranes. Microsecond and millisecond time scale dynamics are often studied by using phosphorescent probes.<sup>14,15,74</sup> Other techniques, such as electron paramagnetic resonance(EPR), using site-directed spin labeling are also useful for these purposes.<sup>65</sup> However, excited-state probes potentially offer greater sensitivity for signal detection when compared with EPR. Transition-metal complexes containing one or more diimine ligands exhibit tunable, long luminescence lifetimes (100 ns to ~10  $\mu$ s), polarized emission, high photostability, large Stokes shifts, and sensitivity to the probe environment.<sup>30,71,73</sup> In addition, the lifetimes of these probes can be tuned

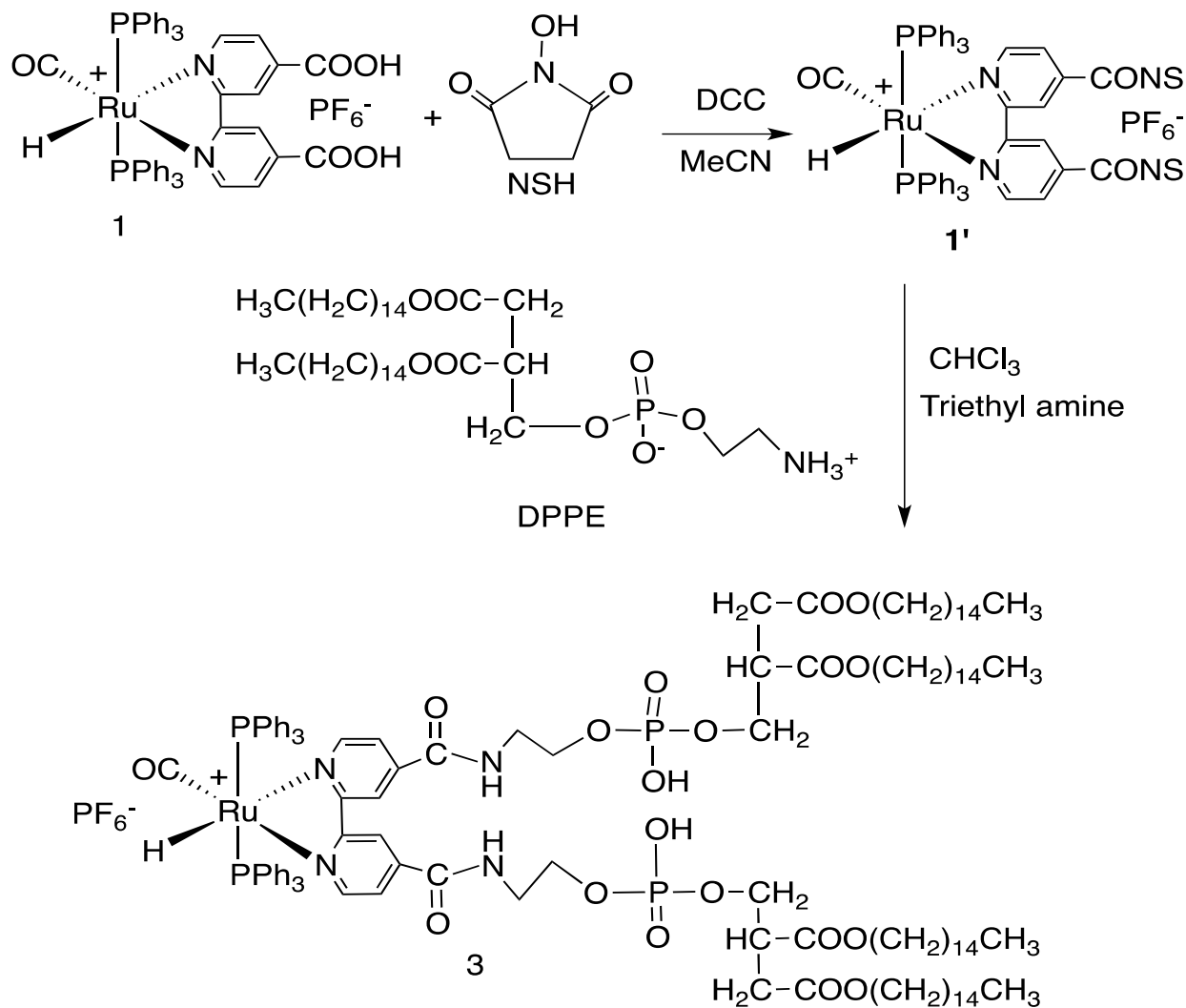
by varying the ligands attached to the metal center.<sup>30,72</sup> Microsecond excited-state lifetimes and polarized emissions make them useful probes for studying the microsecond time scale dynamics of membranes and macromolecular assemblies.  $[\text{Ru}^{\text{II}}(\text{bpy})_3]^{2+}$  and other similar transition-metal complexes are now extensively used to understand the nature of the charge-transfer excited state.<sup>60,62,63,67,75-78</sup> Typically these complexes contain diimine ligands such as 2,2'-bipyridyl(bpy), 1,10-phenanthroline(phen), and their derivatives 4,4'-dicarboxy-bpy (dcbpy) and 5-amino-1,10-phen, which provide low-energy  $\pi^*$  orbitals for accepting the excited electron from the metal. Other ligands, such as phosphines, carbonyl, and halides, can be introduced with the diimine ligands to tune the luminescence and solution properties. In these systems, the initial singlet excited state undergoes intersystem crossing with a quantum efficiency close to unity; the radiative lifetime of the triplet metal-to-ligand charge transfer (<sup>3</sup>MLCT) state reflects the effect of strong spin-orbit coupling on the degree of singlet-triplet mixing in the excited state.<sup>79,80</sup> As a result, the luminescence lifetime and the overall emission quantum yield of these complexes depend only on the radiative ( $k_r$ ) and nonradiative ( $k_{nr}$ ) decay rates of the triplet state. According to the energy gap law,  $k_{nr}$  increases exponentially as the emission energy decreases.<sup>81-84</sup> Other factors, such as the Jahn-Teller distortion of the excited <sup>1</sup>MLCT state, also increase nonradiative decay ( $k_{nr}$ ).<sup>85-87</sup> Therefore, in order to obtain luminescence from transition-metal complexes, a delicate balance of the energy levels of the metal and the ligand energy levels must be established. The highly polarized emission from some of these complexes stimulated our interest in using these complexes as anisotropy probes for biophysical studies.<sup>65,88</sup> Luminophores covalently attached to macromolecules often undergo local (segmental) motions in addition to depolarization through global Brownian tumbling of the entire macromolecule. This results in complex anisotropy decays; time-resolved anisotropy measurements can be used to resolve

information about segmental motion, global motion, size and shape of the macromolecule, and flexibility of the system.<sup>29</sup> From a practical point of view, the fundamental, zero-time anisotropy ( $r_0$ ) should be at least 0.05 or greater. The fundamental anisotropy is related to molecular symmetry. For example,  $[\text{Ru}^{\text{II}}(\text{bpy})_2(\text{dcbpy})]^{2+}$  and  $[\text{Ru}^{\text{II}}(\text{bpy})_2(\text{phen})]^{2+}$ , which contain more than one type of diimine ligand, (i.e., less symmetric), show higher maximum fundamental anisotropies (excited near 490 nm,  $r_0 \sim 0.25$  and  $\sim 0.175$ , respectively) than the more symmetric complex  $[\text{Ru}(\text{bpy})_3]^{2+}$  (excited near 460 nm,  $r_0 \sim 0.13$ ).<sup>5</sup> Transition-metal complexes with a single chromophoric ligand have been reported for Re(I) and Ru(II) complexes (e.g.,  $[\text{Re}(4,7\text{-Me}_2\text{-phen})(\text{CO})_3(4\text{-COOHPy})][\text{PF}_6]^{89}$  and  $[(\text{H})\text{Ru}(\text{CO})(\text{dcbpy})(\text{PPh}_3)_2][\text{PF}_6]^{30}$ ), but their fundamental anisotropies have not been reported. Because low molecular symmetry is expected to promote high anisotropy, and because high anisotropy is required for membrane dynamics measurements, the complexes reported here were designed with one diimine ligand, the anisotropy of which is compared in one case with that of a tris-diimine complex.

Covalently attaching a ruthenium–polypyridyl probe with a long-lived excited state to either cholesterol or a phospholipid requires complementary functional groups for conjugation. Metal–polypyridyl complexes with carboxylate or amine functional groups are suitable for covalent conjugation to lipids, cholesterol, and proteins.<sup>29,65,66</sup> Phosphatidylethanolamine, a glycerophospholipid found in biological membranes, contains an amine group that can be reacted with a carboxyl group on the metal ligand via formation of an activated ester. The chloroformate derivative of cholesterol, on the other hand, can be covalently bound to an amine-substituted ligand. In both cases, the resulting conjugates can be easily incorporated into lipid-bilayer vesicles or biological membranes for photophysical measurements.<sup>2,17</sup> Here, we report phospholipid and cholesterol conjugates for the complexes  $[(\text{H})\text{Ru}(\text{CO})(\text{PPh}_3)_2(\text{dcbpy})][\text{PF}_6](\mathbf{1})$



and [(H)Ru(CO)(dppene)(5-amino-1,10-phen)][PF<sub>6</sub>](**2**), (dppene = bis(diphenylphosphino)ethylene), along with a detailed analysis of their polarized emissions when they are incorporated into different types of large lipid unilamellar vesicles (LUVs). To understand the effects of conjugation through the diimine luminophore on the photophysical properties of these complexes, we also present an investigation of the first example of a



DPPE = 1,2-dihexadecanoyl-*sn*-glycero-3-phosphoethanolamine  
 NHS = N- hydroxy succinimide  
 DCC = dicyclohexyl carbodiimide

**Scheme 2**

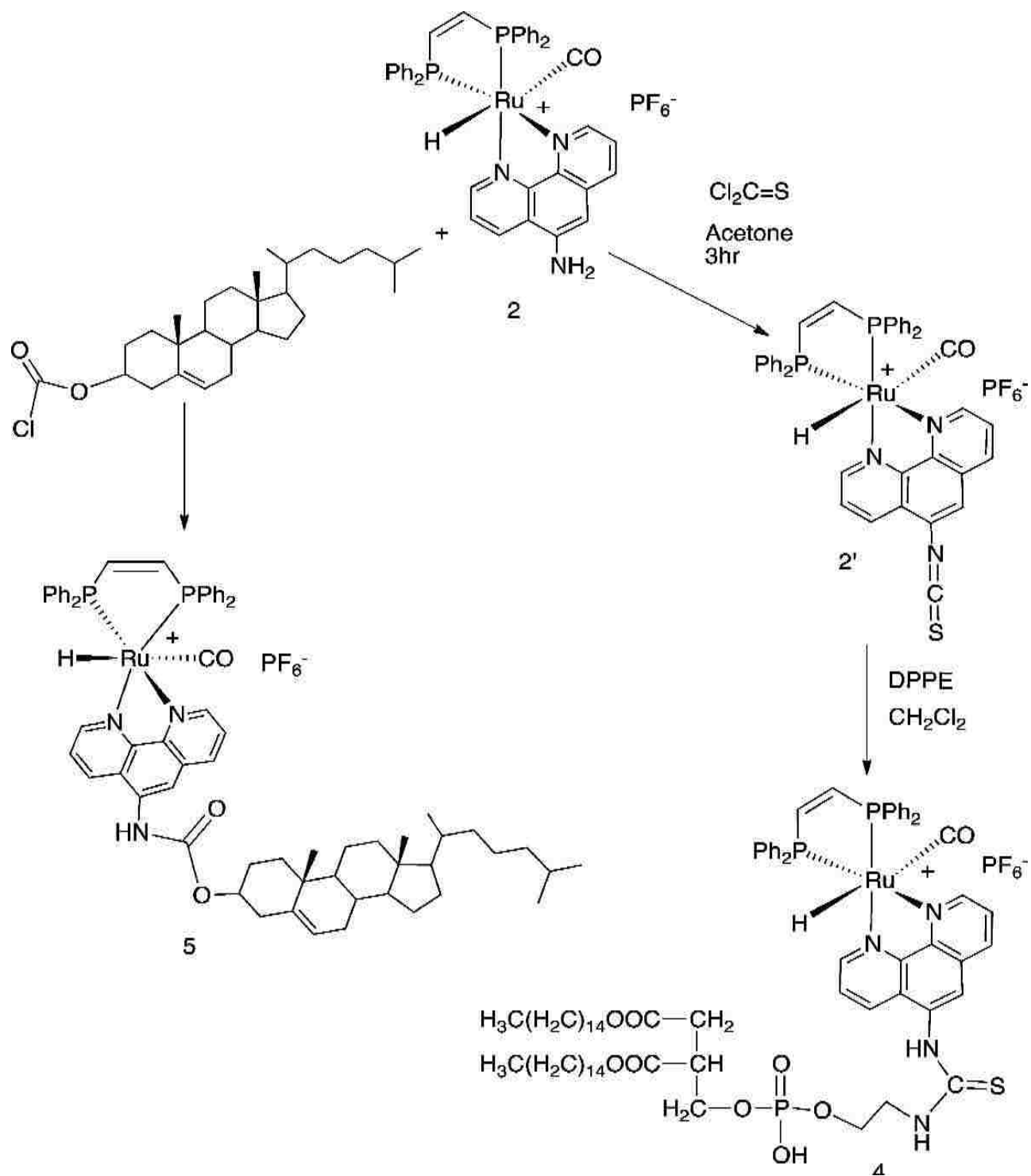
transition-metal complex conjugated through the phosphine ligand using trans- $[(\text{H})\text{Ru}(\text{bpy})(\text{Ph}_2\text{PCH}_2\text{CH}_2\text{COOH})_2][\text{PF}_6]$  (**6'**) as the precursor. To our knowledge, this is the first such report. For comparison with the photophysical properties of the phosphine-containing complexes 1–6', we also report the photophysical properties of the cholesterol and monolipid conjugates of the complex  $[\text{Ru}(\text{bpy})_2(5\text{-amino-1,10-phen})][\text{PF}_6]_2$  (**8**). The lipid conjugate of complex 8 was previously reported.<sup>60,67</sup>

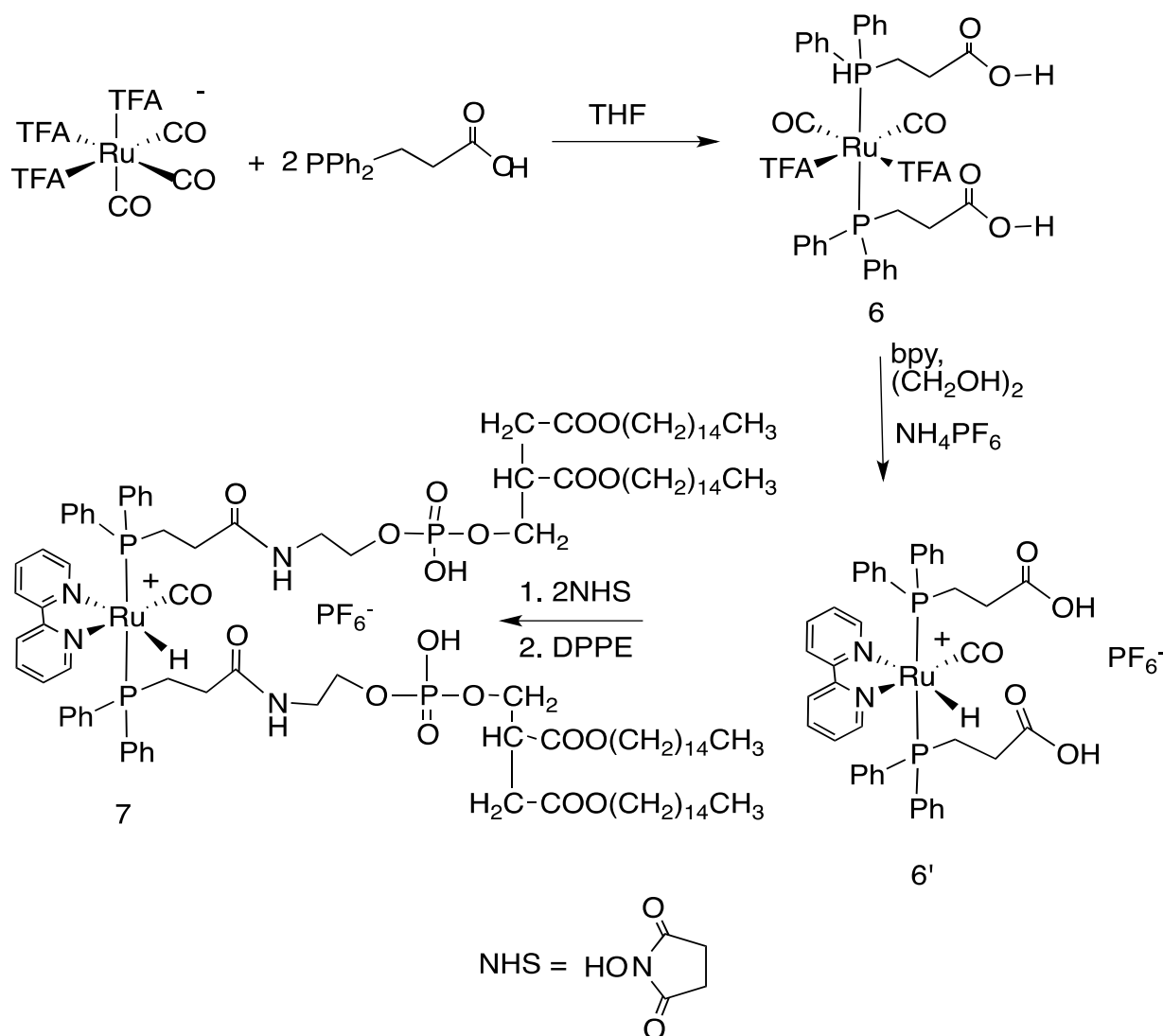
## 2.2 Results

### 2.2.1 Synthesis

Schemes 1 and 2 describe the ligand modification and conjugation of the ruthenium probes with lipids and cholesterol. For the phospholipid conjugations, we used diimine ligands containing either activated ester or highly reactive isothiocyanate functional groups. Complex 1 contains a bpy ligand with two carboxylic acid groups, which were converted to the activated ester groups, and the activated ester groups were then used to form a peptide bond with the primary amine of DPPE. Complex 3, conjugated to two DPPE molecules, was synthesized and purified by standard chromatographic methods. Complex 4 was obtained by first converting the amine group on the 5-amino-1,10-phen ligand of complex 2 into 5-isothiocyanato-1,10-phen (SCN-phen), and then one molecule of DPPE was conjugated with the ruthenium probe through formation of a thiourea bond between SCN-phen-Ru and the primary amine group of DPPE. Because cholesterol is an important component of biological membranes, we synthesized the cholesterol conjugate of the ruthenium complex 2. The amino group of 5-amino-1,10-phen was used to form the amide bond in complex 5 by reacting complex 2 with the highly reactive cholesteryl-chloroformate. All conjugated transition-metal complexes reported here were characterized by IR,  $^1\text{H}$  NMR, and  $^{31}\text{P}$  NMR spectroscopies. In the IR, the terminal M–CO

shows CO stretching modes around  $2150\text{--}1850\text{cm}^{-1}$ . Complexes 1–5 have only one M–CO ligand. The strong M–CO stretch appears at  $1949$  and  $1956\text{ cm}^{-1}$  for complexes 1 and 3,





**Scheme 4**

respectively, and complexes 2, 4, and 5 showed strong M–CO stretches from 1990 to 1997 $\text{cm}^{-1}$ . Strong absorptions in the organic carbonyl region were also observed for the carboxy-amide functional group in complex 5 and for the glycerol-ester groups of lipids in complexes 3 and 4. Medium intensity absorptions from 2102 to 2050 $\text{cm}^{-1}$  are observed for 4, which are assignable to the iso-thiocyanate (N=C=S) stretches. The  $^1\text{H}$  and  $^{31}\text{P}\{^1\text{H}\}$  NMR spectra of complexes 1' and 3

obtained in CDCl<sub>3</sub> are consistent with the proposed structures. The M–H resonance appeared as a triplet at  $\delta$  –11.07 ( $J = 20$  Hz) for complex 1' and as a broad multiplet at  $\delta$  –11.19 upon conjugation with lipids in complex 3. The hydride resonances for complexes 2, 4, and 5 appear as triplets at  $\delta$  –7.61, –7.5, and –7.6, respectively. The aromatic region of the <sup>1</sup>H spectra is complex because of the phenyl protons of the phosphine ligands and the aromatic protons of the diimine ligands. The CH=CH protons of dppe are observed from  $\delta$  6.2 to 6.9 for complexes 2, 4, and 5. The conjugates showed chemical shifts in the aliphatic regions that are characteristic of the corresponding lipid and cholesterol. The <sup>1</sup>H NMR resonances for the lipid and cholesterol conjugates are slightly broader than those of the unconjugated complexes (Appendix A, Figures A6–A10), probably because the rotational correlation times of the complexes are long, which means that the molecules are not orientationally averaged and therefore do not display sharp signals. This could also be the result of aggregate formation in the polar organic solvents used. The chemical shifts of the metal-bound phosphine ligands in the <sup>31</sup>P NMR spectra are in good agreement with those of similar Ru(II)phosphine complexes.<sup>30</sup> Complexes 1–5 show singlet resonances from  $\delta$  49.2 to 75.7 relative to external H<sub>3</sub>PO<sub>4</sub>; these resonances are due to the triphenyl and diphenylphosphino-ethylene ligands. The singlet observed for these complexes indicates that they have a symmetry plane that makes the two phosphorus nuclei magnetically equivalent in complexes 1 and 3, which is consistent with the proposed structures. That singlets are observed for complexes 3–5 as well suggests that the asymmetry in the phenanthroline ring is not sufficient to preclude overlap of the phosphine resonances. This is also the case for complex 2.<sup>30</sup> The <sup>31</sup>P resonances for the lipid phosphorus atoms are observed at  $\delta$  25.0 (2P) and 58.19 (1P) for complexes 3 and 4, respectively. The higher-frequency shift in complex 4 relative to that of complex 3 might result from the different modes of binding to the diimine ring or to

conformational effects. In all the  $^{31}\text{P}$  NMR spectra, the counter anion  $[\text{PF}_6^-]$  appeared as a septet at  $\delta=155$  with an integrated relative intensity of 1:2 when compared with the phosphine ligand resonances. To evaluate the effect of the site of lipid conjugation on the photophysical properties of the complexes in LUVs, we synthesized complex 7 (Scheme 3). This was done by reacting the common starting material  $[\text{K}][\text{Ru}(\text{CO})_3(\text{TFA})_3]$  with DPPA to give the 3-(diphenylphosphino)propionyl carboxylate 6 (two isomers were observed by  $^1\text{H}$  NMR), which was then reacted with bpy to give complex 6'. The bis-lipid conjugate was obtained by conversion of complex 6' to the activated ester derivative 6''. Then conjugation with DPPE, using a procedure similar to that used for the synthesis of complex 3, gave trans-[(H)Ru-(PPh<sub>2</sub>C<sub>2</sub>H<sub>4</sub>C(O)-N-DPPE)<sub>2</sub>(bpy)(CO)][PF<sub>6</sub>](7) (Scheme 3). The complexes were characterized spectroscopically at each stage of the synthesis, to confirm evidence of the formation of the expected analogues of complexes 1 and 3. Under the conditions used for the reaction with bpy, namely, refluxing in ethylene glycol, all of the complexes were converted to their corresponding hydrides. Note that complexes 4 and 5 are chiral, while complexes 3 and 7 are not, by virtue of the symmetry plane that is perpendicular to the two trans-phosphines and contains the other ligands. Because we observe only one set of NMR resonances for both complexes, either the chemical shift differences for the diastereomers of complexes 4 and 5 are not large enough to be resolved or only one of the diastereomers is populated.

Compound	$\lambda_{ab}$ (nm)	$\lambda_{em}$ (nm)	$\tau$ ( $\mu$ s)	$\phi$
<b>1</b> [HRu(CO)(PPh <sub>3</sub> ) <sub>2</sub> (4,4'-dcbpy)][PF <sub>6</sub> ]	303, 468	647	0.72	0.30 <sup>a</sup>
<b>2</b> [(H)Ru(CO)(dppene)(5-amino-1,10-phen)][PF <sub>6</sub> ]	289, 364, 442	610	0.25	0.25 <sup>a</sup>
<b>3</b> [HRu(CO)(PPh <sub>3</sub> ) <sub>2</sub> (dcbpy- <i>N</i> -DPPE <sub>2</sub> )][PF <sub>6</sub> ]	316, 442	----	----	----
<b>4</b> [(H)Ru(CO)(dppene)(1,10-phen-5- <i>N</i> -DPPE)][PF <sub>6</sub> ]	360,450	618	----	----
<b>5</b> [(H)Ru(CO)(dppene)(1,10-phen-5-NHC(O)OChol)][PF <sub>6</sub> ]	356, 440	605	0.47	0.49
<b>6</b> [(H)Ru(CO)(dppa) <sub>2</sub> (bpy)][PF <sub>6</sub> ]	460	608	0.27	0.50 <sup>b</sup>
<b>7</b> [(H)Ru(CO)(dppa- <i>N</i> -DPPE) <sub>2</sub> (bpy)][PF <sub>6</sub> ]	295,400	505	0.004	0.019
<b>8</b> [Ru(bpy) <sub>2</sub> (5-amino-phen)][PF <sub>6</sub> ] <sub>2</sub>	350,445	625	0.22	
<b>9</b> [Ru(bpy) <sub>2</sub> (1,10-phen-5-NHC(O)OChol)][PF <sub>6</sub> ] <sub>2</sub>	350,445	625	0.22	0.25
<b>10</b> [Ru(bpy) <sub>2</sub> (1,10-phen-5- <i>N</i> -DPPE)][PF <sub>6</sub> ] <sub>2</sub> <sup>c</sup>	330, 460	625	0.22	

**Table 2. Absorption, emission, and excited-state lifetimes of ruthenium MLC probes in ethanol.**

<sup>a</sup>From reference 11

<sup>b</sup>This work

<sup>c</sup>From reference 17,39

## 2.2.2 Photophysical Characterizations of complexes 1-5, 6' and 7-10

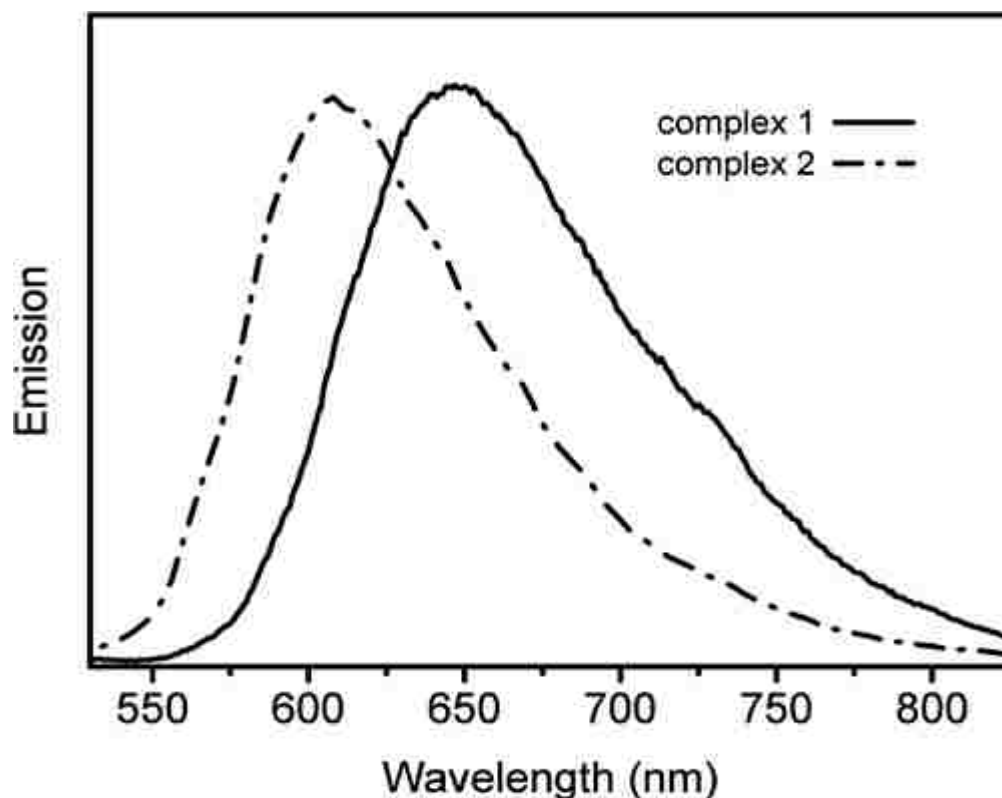


**Figure 8** Peak-normalized emission spectra of complex  $[\text{HRu}(\text{CO})(\text{PPh}_3)_2(\text{dc bpy})][\text{PF}_6]$  (1) and  $[\text{(H)Ru}(\text{CO})(\text{dppene})(5\text{-amino-1,10-phen})][\text{PF}_6]$  (2) in ethanol.

Table 2 lists the absorption and emission maxima and the luminescence lifetimes for complexes 1–7 in ethanol. All of the compounds show intense, higher-energy absorptions at 270–295 nm due to the spin-allowed intraligand ( $\pi\text{-}\pi^*$ ) transitions. These absorptions are not shown in Table 1 in order to focus on the more important MLCT and phosphine absorptions. In the case of complex 7 the absorption at 295 nm is due to the phosphine. The absorptions of this complex are all blue-shifted relative to the others including the MLCT (vide infra), and this is borne out by the excitation spectra (see Appendix A, Figure A1). The absorptions observed between 356 and 366 nm for complexes 2, 4, and 5 are due to the presence of the double bond in



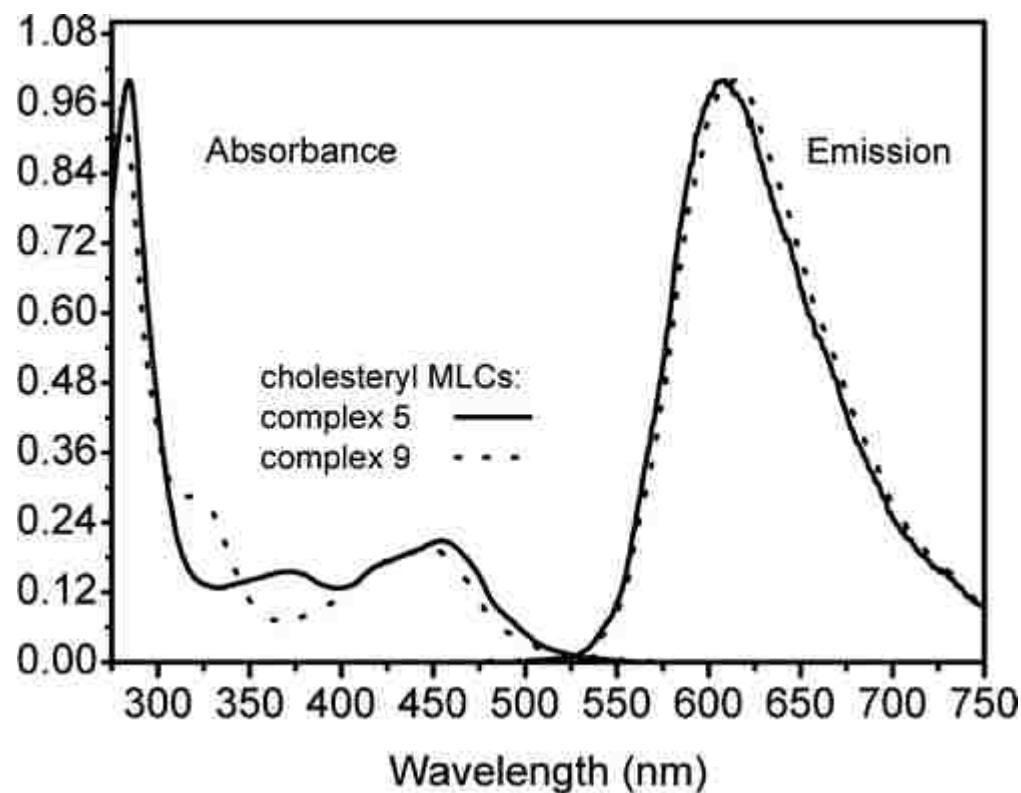


**Figure 9** Absorption and emission spectra of complex [(H)Ru(CO)-(dppene)(1,10-phen-5-NHC(O)OChol)][PF<sub>6</sub>] (5) and complex [Ru-(bpy)<sub>2</sub>(1,10-phen-5-HC(O)OChol)][PF<sub>6</sub>]<sub>2</sub> (9) in ethanol.

the chelating phosphine ligand of these complexes. The less-intense absorption bands ( $\epsilon_{450} \approx 2 \times 10^3 \text{ M}^{-1} \text{ cm}^{-1}$ ) of all probes and their conjugates in the visible region (410–490 nm) are attributed to spin-allowed <sup>1</sup>MLCT (d– $\pi^*$ ) transitions. The <sup>1</sup>MLCT absorption bands of the complexes containing dcbpy are at slightly lower energy than the lipid-derivative complex 3. In the cases of complexes 4 and 7 the MLCT absorption is blue-shifted to  $\approx 400$  nm (see Appendix A, Figures A4 and A5). All the complexes containing the chelating phosphine and phenanthroline ligands displayed <sup>1</sup>MLCT absorption bands at similar wavelengths. In ethanol, acetonitrile, or methylene chloride, complexes 1, 2, 5, and 6' displayed long-lived, orange-red luminescence characteristic of a <sup>3</sup>MLCT excited state (see Figure 8; the emission spectra of complexes 5 and 6'-not shown-are very similar to those of complexes 2 and 1, respectively). The conjugation with cholesterol (complex 5) resulted in an approximate twofold increase of the

excited-state lifetime. No emission was observed from complex 3, and a very weak emission at 520 nm was observed for complex 4. This emission had a short lifetime (4–5 ns) and had an ill-defined excitation spectrum (see Appendix A, Figure A4). At 608 nm, complex 6' exhibits a <sup>3</sup>MLCT emission, which interestingly has a much shorter lifetime but a higher quantum yield than that of complex 1. Complex 7 showed a blue-shifted <sup>1</sup>MLCT absorption band with a peak near 400 nm; excitation at 450 nm gave an emission with a maximum at 505 nm with a lifetime of ~4.46 ns in chloroform at 5 °C (see Table 1). The quantum yield of this emission was found to be 0.019, making this a very weak singlet emission. Thus, bis-lipid conjugation via the phosphine ligand does not cause quenching of the luminescence as seen for complex 3 but gives the short-lived, blue-shifted emission in ethanol observed for complex 4. Complexes 8–10, on the other hand, showed identical long-lived <sup>3</sup>MLCT emissions with a peak near 625 nm. The absorption and emission spectra of complex 9 are shown in Figure 9. Analysis of the time-resolved anisotropy decay of complexes 1, 2, and 5 in neat glycerol at 0 °C and with excitation at 470 nm yielded  $r_0$  values of 0.124, 0.077, and 0.121, respectively.

### **2.2.3 Photophysical Studies of Complexes 3–5, 7, 9, and 10 Incorporated in Lipid**

#### **Membrane Bilayers.**

The lipid conjugates 3, 4, 7, and 10 and the cholesterol conjugates 5 and 9 were incorporated in LUVs to study the photophysical properties of these probes in a membrane-like environment. The maximum of the low-energy absorption band was near 440 nm except for complexes 4 and 7, which had this absorption at ~400 nm. The dynamics of these probes incorporated in the LUVs were determined from the kinetics of the time-resolved emission anisotropy. Although the absorption spectrum for complex 3 from 400 to 550 nm was characteristic of the charge-transfer band and essentially identical in chloroform, ethanol, and

lipid LUVs, emission was only observed when complex 3 was incorporated in LUVs. Furthermore, the emission spectrum of complex 3 in the LUVs was blue-shifted ( $\lambda_{\text{max}} = 534$  nm, Figure 10) with respect to that of the precursor probe 1 ( $\lambda_{\text{max}} = 647$  nm in ethanol) (see Table 1 and Figure 8). Complex 3 also exhibited a very short excited-state lifetime (11 ns at 5°C, air equilibrated) in PC-LUVs. Complex 4 in ethanol solution showed a weak short-lived emission at 520 nm. Complex 4 in PC-LUVs also had a blue-shifted emission (545 nm) with a short lifetime (8 ns) (see Figure 10), similar to its emission in solution, but with a much higher intensity. Both complexes showed more intense emission in LUVs compared to that of the red-shifted emission of the unconjugated precursors 1 and 2 in ethanol. The emission yield of complex 3 was greater than that of complex 4, as was the case for the bpy complex 1 relative to the phen complex 2. Complex 7 showed the same blue-shifted emission in the LUVs as in ethanol. Complex 10 did not show this blue shift when incorporated in LUVs but did show a factor of 2 increase in the excited-state lifetime (0.22 to 0.52  $\mu\text{s}$ ). To eliminate the possibility that the blue-shifted, short-lifetime emissions of complexes 3 and 4 in lipid LUVs were due to decomposition in the lipid bilayer, we synthesized the bis-lipid derivative dcbpy-N-DPPE2 (11) (see Appendix A) and compared the photophysical behavior of this compound in egg-PC-LUVs to that of complexes 3 and 4 in lipid LUVs. This conjugate, which lacks the metal center, showed a less intense absorption band at 327 nm and an intense absorption band at 295 nm, characteristic of the unconjugated dcbpy ligand. Furthermore, the emission maximum of 11 in PC-LUVs was at 405 nm (excitation at 327 nm), not near 534 nm, and complex intensity decay kinetics were observed with a 5 ns intensity-averaged lifetime,  $\langle\tau\rangle$ . In another experiment, we prepared PC-LUVs without any probe incorporated. As expected, there was no emission whether excited at 327 or 450 nm. These LUVs, which lacked a probe,

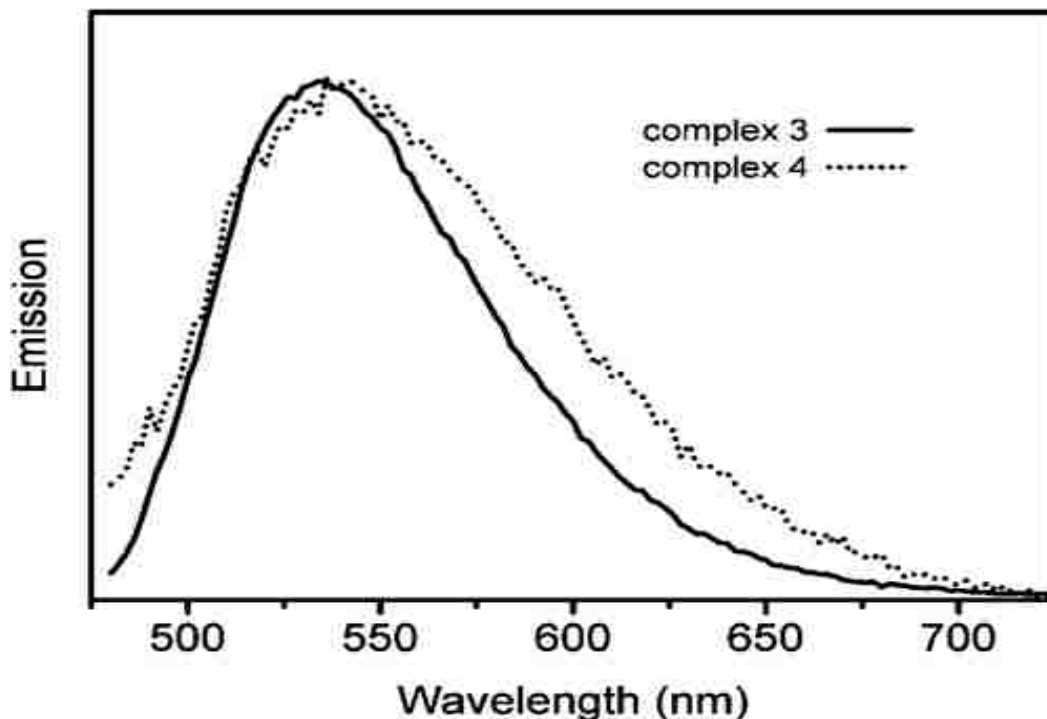


**Figure 10** Peak-normalized emission spectra of complex  $[(H)Ru(CO)(PPh_3)_2(dcbpy-N-DPPE_2)][PF_6]$  (3) and  $[(H)Ru(CO)(dppene)(1,10\text{-phen-5-NHC(S)-N-DPPE})][PF_6]$  (4) in egg-PC LUVs

were then incubated at 35°C with complex 3 previously dissolved in THF (THF was approximately 2% of the final volume) to adsorb the probe onto the LUVs. In contrast to the conjugate incorporated in LUVs by the standard reconstitution procedure, described previously, the emission spectrum of the bis-lipid conjugate adsorbed onto the preformed LUVs had its maximum at 620 nm, characteristic of  $^3MLCT$  luminescence. However, when this preparation was subsequently extruded through the sizing membrane, the blue-shifted emission with a maximum near 530 nm was once again observed. These results indicate that the blue-shifted emission and short, nanosecond-time scale excited-state lifetime observed for complex 3 are not due to the decomposition of the complex to a free bpy-DPPE moiety, but are features of the system when the probe is incorporated into the LUV bilayer.

**Table 3. Average lifetime, limiting anisotropy and rotational correlation times for complexes 3 and 4 in egg-PC LUVs (100 nm) from 5–50°C.**

Compound	Temp. (°C)	$\langle\tau\rangle^a$ (ns)	$r_\infty$	$\theta_1$ (ns) <sup>b</sup>	$\theta_2$ (ns) <sup>b</sup>	$\chi^2$
<b>3</b>	5	11	0.096	9.8(-1.62, 1.69)	2.46(-0.21, 0.24)	1.18
	10	9.4	0.07	8.62(-1.68, 2.4)	1.95(-0.18, 0.21)	1.10
	20	7.9	0.05	5.5(-1.31, 2.05)	1.2(-0.17, 0.18)	1.13
	30	6.7	0.03	4.1(-0.55, 0.68)	1.0(-0.06, 0.07)	1.19
	40	5.5	0.02	3.2(-1.84, 1.89)	0.58(-0.51, 1.0)	1.15
	50	4.5	0.01	1.6(-0.15, 0.42)	0.26(-0.06, 0.18)	1.14
<b>4</b>	5	7.2	0.09	8.4(-0.624, 1.2)	0.79(-0.21, 0.25)	1.19
	10	6.6	0.07	6.3(-0.54, 0.62)	0.83(-0.11, 0.13)	1.1
	20	5.8	0.04	5.4(-1.35, 2.01)	0.5(-0.03, 0.04)	1.2
	30	4.8	0.02	3.3(-0.15, 0.16)	0.36(-0.03, 0.02)	1.08
	40	3.8	0.01	2.0(-0.10, 0.11)	0.29(-0.04, 0.05)	1.0
	50	3.1	0.008	1.3(-0.08, 0.085)	0.13(-0.04, 0.041)	1.1

<sup>a</sup>Intensity-average lifetime,  $\langle\tau\rangle = \sum\alpha_i \tau_i^2 / \sum\alpha_i \tau_i$

<sup>b</sup>Upper and lower 95% confidence limits, calculated by support-plane method, are indicated within parenthesis.

This conclusion is also supported by the observation that the <sup>1</sup>MLCT absorption band of complex 3 is the same both in alcohol solution and in PC–LUVs. A progressive decrease in the blue-shifted luminescence intensity with increasing temperature was observed over the temperature range of 5–50°C (Table 3). The change in excited- state lifetime and the anisotropy decay of the blue-shifted emission of complexes 3 and 4 incorporated in PC–LUVs were also measured over a range of temperatures to determine the sensitivity of these probes toward changes in the microviscosity of the

bilayer environment. The excited-state lifetime decreased progressively with increasing temperature, consistent with the decrease in luminescence expected for quenching by thermally activated motions. An increase in the local motions, as reflected by the decrease in the rotational correlation times, was also observed with increasing temperature. The blue-shifted emission of lipid-conjugated probes 3 and 4 showed high fundamental anisotropy values (excitation at 470 nm,  $r_0 = 0.24$  and  $0.35$ , respectively) in LUVs compared to those of the red-shifted emission of complexes 1 ( $r_0 = 0.12$ ), 2 ( $r_0 = 0.08$ ), and 5 ( $r_0 = 0.12$ ) in glycerol. The results of analyses of the time-resolved anisotropy data in terms of a double exponential decay for complexes 3 and 4 in LUVs at variable temperature are summarized in Table 3. At lower temperatures, the anisotropy decay revealed a significant contribution from the limiting anisotropy at infinite time ( $r_\infty$ ); a nonzero  $r_\infty$  is indicative of restricted motion in the membrane.<sup>74</sup> Compound 7 was examined in DMPC– LUVs and showed a slightly longer lifetime of 4.56 ns, a very high fundamental anisotropy of 0.31, and a significant  $r_\infty$  of 0.103. These properties closely parallel those observed for complexes 3 and 4 in LUVs. The variable-temperature study of this emission showed very little variation in lifetime over the range of 0–30°C, which is likely due to the low quantum yield observed for 7 in solution. The absorption and emission spectra of cholesterol-conjugate complexes 5 and 9 in ethanol are shown in Figure 9. In contrast to the lipid-conjugate complexes 3 and 4, the emission spectra of complexes 5 and 9 are red-shifted and identical to those observed when incorporated in the egg-PC–LUVs. In addition, the excited-state lifetimes 0.47 and 0.22  $\mu\text{s}$  for 5 and 9 increased to 0.89 and 0.52  $\mu\text{s}$ , respectively, for the complexes in egg-PC– LUVs at 23 °C in ethanol. Complexes 4

and 7 both showed blue-shifted luminescence with a maximum near 505 nm and a lifetime of ~4 to 5 ns in egg- PC-LUVs, similar to that observed in ethanol. This

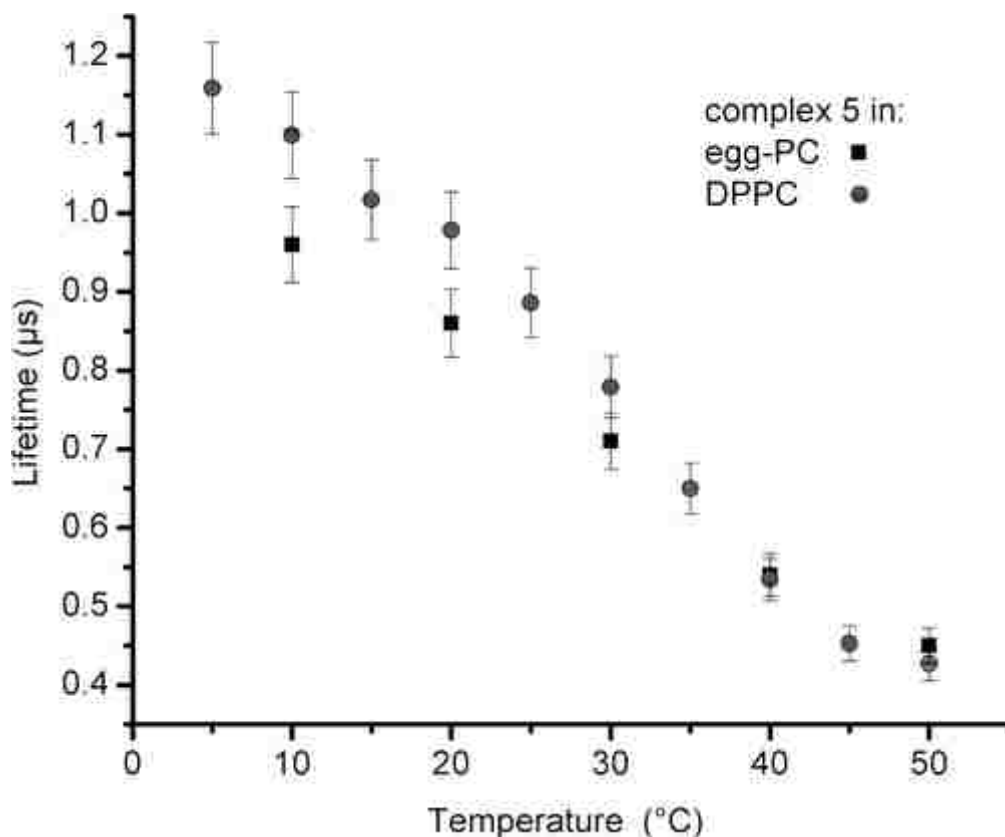


**Figure 11** Average lifetime of complex [(H)Ru(CO)(dppene)(1,10- phen-5-NC(O)OChol)]PF<sub>6</sub>( 5) in LUVs over a range of temperatures. Error bars are based on the errors in the nonlinear least-squares fit using the support plane method developed by M.L. Johnson and S.G. Frasier and described in *Methods in Enzymology* Vol. 117, Academic Press: New York 1985 p. 301

indicates that the large blue shifts and short lifetimes observed for the emissions of complexes 3 and 4 in LUVs are likely due to large perturbations in the geometry and/or electronic energies of the excited states. In Complex 10 the lipid is conjugated to the phen rather than bpy ligand, which is the likely luminophore, does not show a blue shift, and has an excited state lifetime typical of a <sup>3</sup>MLCT (0.41 μs). The perturbations that result in the blue shifts and short lifetimes for complexes 3, 4, and 7 are likely the result of conjugation of the large lipid molecules directly to the luminophore or to an

ancillary ligand (phosphines) that makes a significant contribution to the MLCT excited state, but this is not the case for complex 10.<sup>60,67,90</sup> Egg-PC has a low phase-transition temperature (less than 0 °C) because it contains mixed saturated and unsaturated acyl chains of different lengths, leading to a highly disordered phase. To understand the effect of a more ordered membrane on the observed rotational correlation times, we measured the photo-physical properties of complex 5 incorporated in DPPC-LUVs, which have two 16-carbon saturated acyl chains. The phase-transition temperature for DPPC is 41 °C;<sup>91</sup> the bilayer is in an ordered phase below this temperature. As in egg-PC, the emission of complex 5 was red-shifted in DPPC. An analysis of the time-dependent anisotropy decay of complex 5 incorporated in either egg-PC or DPPC-LUVs resulted in a fundamental anisotropy value of  $\sim 0.1$ . A single exponential satisfactorily fit the time-resolved intensity decay of complex 5. In the DPPC-LUVs, the luminescence lifetime of complex 5 ranges from 1.10  $\mu\text{s}$  at 10°C to 0.43  $\mu\text{s}$  at 50°C. This temperature range spans the phase-transition temperature of DPPC (41 °C). In egg-PC-LUVs, the same lifetime is comparable (0.96  $\mu\text{s}$  at 10°C and 0.45  $\mu\text{s}$  at 50°C) (see Figure 11). The long decay times suggest that these probes can be used to measure rotational motions as long as 3  $\mu\text{s}$  (3 times the mean intensity decay time).<sup>29,61</sup> The rotational motions of complex 5 in egg-PC-LUVs were also analyzed over a range of temperatures. The rotational correlation time decreased from 112 to 14 ns as the temperature increased from 10 to 50 °C (Table 3). The recovered rotational correlation times are not due to the overall rotation of the 100 nm diameter LUVs,



**Table 4. Average lifetime, limiting anisotropy and rotational correlation times for complex 5 at a range of temperature in 100-nm egg-PC LUVs.**

Temp. (°C)	$\langle\tau\rangle^a$ ( $\mu\text{s}$ )	$r_\infty$	$\phi$ (ns) <sup>b</sup>	$\chi^2$
5	1.46	0.058	71(-1.61, 2.0)	1.00
10	1.24	0.055	54(-1.47, 1.93)	1.02
20	0.94	0.046	49(-1.46, 2.0)	1.08
30	0.68	0.051	44(-1.51, 2.4)	1.08
40	0.57	0.049	24(-1.2, 2.27)	1.18
50	0.47	0.050	10(-4.21, 7.2)	0.98

<sup>a</sup>. Intensity-averaged lifetime,  $\langle\tau\rangle = \sum\alpha_i \tau_i^2 / \sum\alpha_i \tau_i$

<sup>b</sup>. Upper and lower 95% confidence limits, calculated by support-plane method, are indicated within parenthesis.

which would cause these times to be much longer (sub-millisecond range), but are due to local motions. There is considerable uncertainty in measuring longer correlation times of the LUVs because of the difficulty of measuring accurately a correlation time above 3  $\mu\text{s}$  with a probe of 1  $\mu\text{s}$  lifetime. Considering its luminescence lifetime, probe 5 would be more appropriate for studying the overall rotational motion of small unilamellar vesicles (SUVs) with diameters less than 20 nm, which have rotational correlation times in the sub-microsecond range. The time-dependent anisotropy decays at variable temperatures were analyzed by using single-exponential correlation times and a nonzero baseline limiting anisotropy ( $r_\infty$ ), which reflects the restricted motion of the probe during the lifetime of the excited state.<sup>16-18,74</sup>

One of the key design features of the series of complexes 1–7 was to decrease the molecular symmetry by using only one diimine ligand; we reasoned that the decreased symmetry would increase the excitation anisotropy of the transition-metal complex luminescence. To determine whether having only one diimine ligand in the cholesterol conjugate 5 has any

significant effect on, or advantage for, the photophysical properties of this complex in membrane-like environments, we also synthesized, for comparison, a cholesterol derivative of complex 8,<sup>60,67,90</sup> which contains three diimine ligands. This tris-diimine cholesterol conjugate, 9, had a <sup>1</sup>MLCT absorption band and a red-shifted emission maximum similar to those of conjugate 5 (see Figure 9). The tris-diimine complex 9 also had a similar luminescence lifetime ( $\sim 0.41 \mu\text{s}$  at 20°C when incorporated in egg-PC–LUVs). However, the fundamental luminescence anisotropy was much smaller (with excitation at 470 nm,  $r_0 \approx 0.02$  for complex 9 versus  $r_0 \approx 0.12$  for complex 5), consistent with the hypothesis that the larger fundamental luminescence anisotropy of the cholesterol conjugate 5 is due to the decreased symmetry of the mono diimine complex. The anisotropies of the parent complexes 1 and 2 are similar to those of complex 5.

The ruthenium probes reported in this paper that were synthesized with only one diimine ligand showed both the long, microsecond excited-state lifetimes and the sufficiently high fundamental anisotropies required to study dynamics in the sub- microsecond–microsecond time range. Interestingly, the lipid conjugates showed no emission in the case of complex 3 and short-lived blue-shifted emissions in the cases of complexes 4 and 7, in alcohol or chloroform. This lack of emission is likely due to the large number of vibrational modes available, which increases the nonradiative decay when the conjugates are in organic solvents. Consistent with this, conjugate 3, which has two lipids, was nonemissive, whereas conjugate 4, which has only one lipid and the more rigid phenanthroline ring, showed a weak emission that was blue-shifted and short-lived. Interestingly, conjugate 7, in which the lipid is conjugated to the phosphine, showed a blue- shifted weak emission that had a short lifetime in solution; this is likely the result of perturbation of the orbitals contributing to the MLCT excited state or energy transfer to intraligand transitions.<sup>25</sup> In the more constrained environment of the PC–LUVs, intense blue-

shifted emissions were observed for complexes 3 and 4. Complex 7 showed a similar blue shift but with lower intensity in both the LUVs and the organic solvents. Furthermore, the fact that the MLCT absorption spectra of complexes 3, 4, and 7 are very similar in solution and in the LUVs indicates that the orbital perturbation resulting in the blue shift must occur only in the excited state after the electron is transferred from the metal center to the aromatic ring. This suggests that in the initial excited state, the orbital energies are perturbed such that emission takes place from a singlet  $\pi^*$  state. Similar effects have been observed in other ruthenium complexes.<sup>85</sup> Consistent with this interpretation, they also have very short excited-state lifetimes relative to the parent complexes, as well as much higher fundamental anisotropies (see Table 2); the photophysical properties-Stokes shift and lifetime-observed for complexes 3, 4, and 7 in lipid LUVs are characteristic of a singlet emission, although a short-lived triplet cannot be strictly ruled out. Note that the previously reported tris-diimine lipid- conjugated complex 10 does not show the anomalous blue- shifted, short-lived emissions observed for complexes 3, 4, and 7. This could be because, in this complex, the un-substituted diimine ring is the electron acceptor from the metal, and the lipid-conjugated phenanthroline ligand makes no contribution to the excited state, whereas in complexes 3, 4, and 7 the phosphine ligand does contribute to the excited state. This is borne out by the excitation spectra for complexes 3, 4, and 7, in which a significant contribution from phosphine absorptions is observed at about 325–350 nm (see Appendix A). We considered the possibility that the anomalous blue shifts could be due to a fluorescent impurity. However, excitation at varying wavelengths within the MLCT band results in identical emission line shapes characteristic of that compound, and the intensity varies, as expected for the differences in absorption at the different excitation wavelengths. This confirms that the spectra are not due to an impurity. Accompanying the short excited-state lifetimes (11 and 8 ns) in

LUVs, the lipid conjugates have high fundamental anisotropy and temperature-sensitive rotational correlation times, which are helpful for studying faster, local motions (up to 33 ns) in the LUVs. Complexes 3 and 4, which have two and one lipid conjugate, respectively, have double exponential anisotropy decays when incorporated in LUVs. Interestingly, the longer rotational correlation decay times are similar (7–8 ns at 10°C, Table 2). Both the time scale and the insensitivity to the number of lipid anchors suggest that this motion reflects restricted diffusion, classically referred to as “wobble-in-a-cone,”<sup>16-18</sup> and is not due to axial rotation.<sup>92</sup> In the wobble-in-a-cone model, it is assumed that the major axis of the probe wobbles randomly within a cone of semi-angle  $\theta_c$ , which can be estimated using the following relationship:

$$\frac{r_{\infty}}{r_0} = \left[ \frac{1}{2} \cos \theta_c (1 + \theta_c) \right]^2 \quad (2)$$

The temperature-dependent motions of the lipid probes in egg-PC-LUVs were analyzed using this model. Over the temperature range from 10 to 50°C, the cone angle  $\theta_c$  varied from 44° to 72° for complex 3 and from 55° to 74° for complex 4. In contrast to the longer correlation times, the shorter correlation times are significantly different for complexes 3 and 4 (2.0 and 0.7 ns, respectively at 10 °C, Table 2). This time scale and the dependence on the number of anchoring

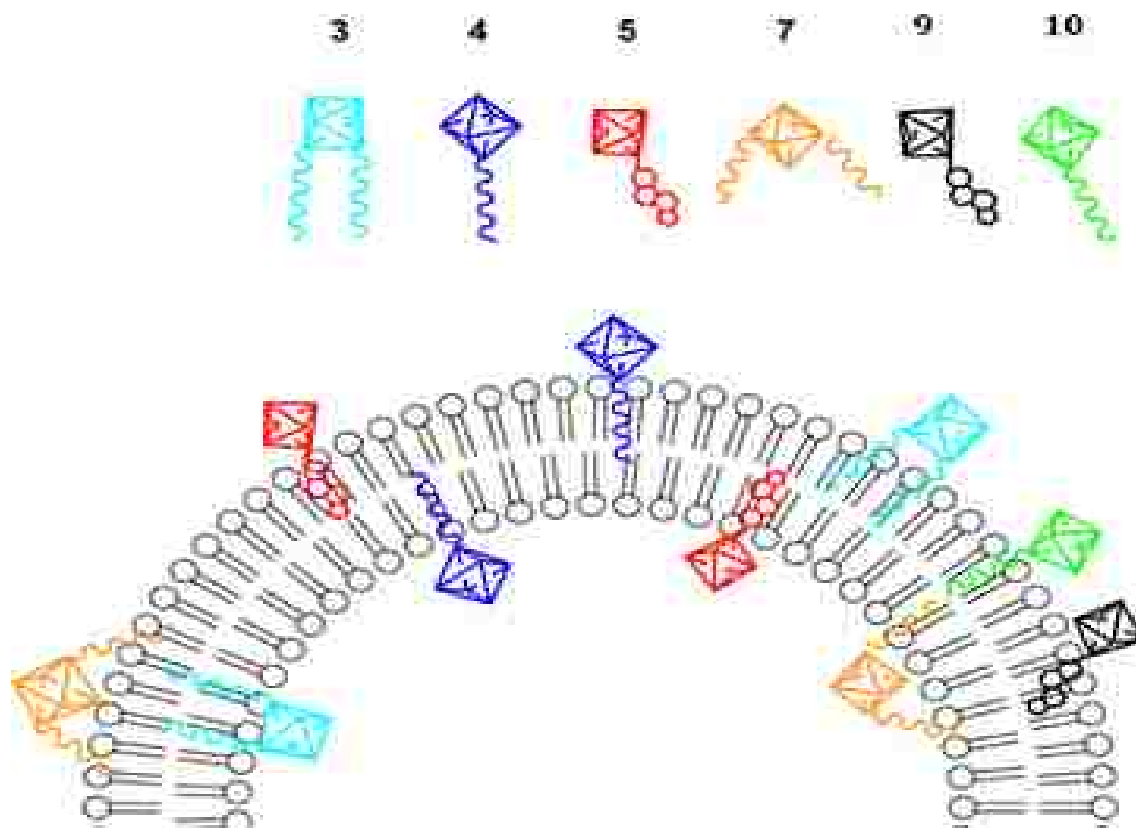


**Figure 12 Representation of the MLC-LUV conjugate interactions showing the differences in probe incorporation into the lipid bilayer.**

lipids indicate that these shorter rotational correlation times mainly reflect the diffusive dynamics of the probe-labeled headgroup.<sup>92</sup> Thus, these probes could be useful for studying lipid-headgroup motions. Recently, reversible coordination and lipid incorporation of a Ru(II) diimine-aqua complex to a thioether cholesteryl conjugate that was previously incorporated into

lipid vesicles was reported.<sup>93</sup> Complex 5, however, to our knowledge, represents the first cholesterol conjugate covalently linked to the diimine ring. The long excited-state lifetimes relative to fluorescence (microseconds versus nanoseconds) and high anisotropy values observed for probe 5 in glycerol and in PC-LUVs make this probe an excellent candidate for studying membrane dynamics on the microsecond time scale. That the cholesterol probes do not show the blue shifts observed for the lipid probes is likely related to the greater rigidity of the cholesterol molecule, and this structural feature leads to less perturbation of the excited-state orbitals. Preliminary data from our laboratory show that this probe is useful for studying the global dynamics of lipid nanodiscs, which are 10 nm diameter recombinant lipoprotein A-lipid constructs.

#### **2.2.4 Ligand Lability**

During the course of this study attempts were made to obtain crystals for X-Ray diffraction of the hydride complexes. In previous publications, only the dc-bpy complex has had the hydride crystal structure reported. The single crystal x-ray structure of the 1,10-phenanthroline complexes were reported as the TFA and Cl derivatives. After several attempts at recrystallization, crystals were collected from an acetone:hexane mixture for the 5-amino-1,10-phenanthroline hydride complex. Once the crystal structure was solved however it was found that a new complex had formed: The crystal contained a complex with 2 chelating DPPENE ligands and a trans CO and TFA (Figure 13).

NMR's of the starting amino-phenanthroline complex show the expected hydride, indicating that the complex rearranged during crystallization. The NMR also revealed that there was some leftover TFA in the hydride sample used for crystallization, which is believed to be the cause of the rearrangement. The excess acid led to the protonation of the phenanthroline ring,

making it highly labile. The crystal also contains solvent molecules indicating that the rearrangement could be very solvent dependent, as it clearly requires solvent coordination in order for it to crystallize.

As this was a unique complex, steps were taken to synthesize and crystallize the double chelated complex on purpose. By simply repeating the reaction for addition of the DPPENE ligand a second time, the bis-chelated complex was synthesized, before crystallization 2 isomers appeared in the IR, a cis and trans isomer for the CO and TFA, however after crystallization only the trans isomer was seen. The product was crystallized in very good yield and data was collected using IR and NMR. Proton NMR data of the complex shows the expected lack of hydride, as does the IR, which also shows the expected  $1690\text{ cm}^{-1}$  stretch for TFA, while the fluorine NMR now shows the expected additional peak for TFA.

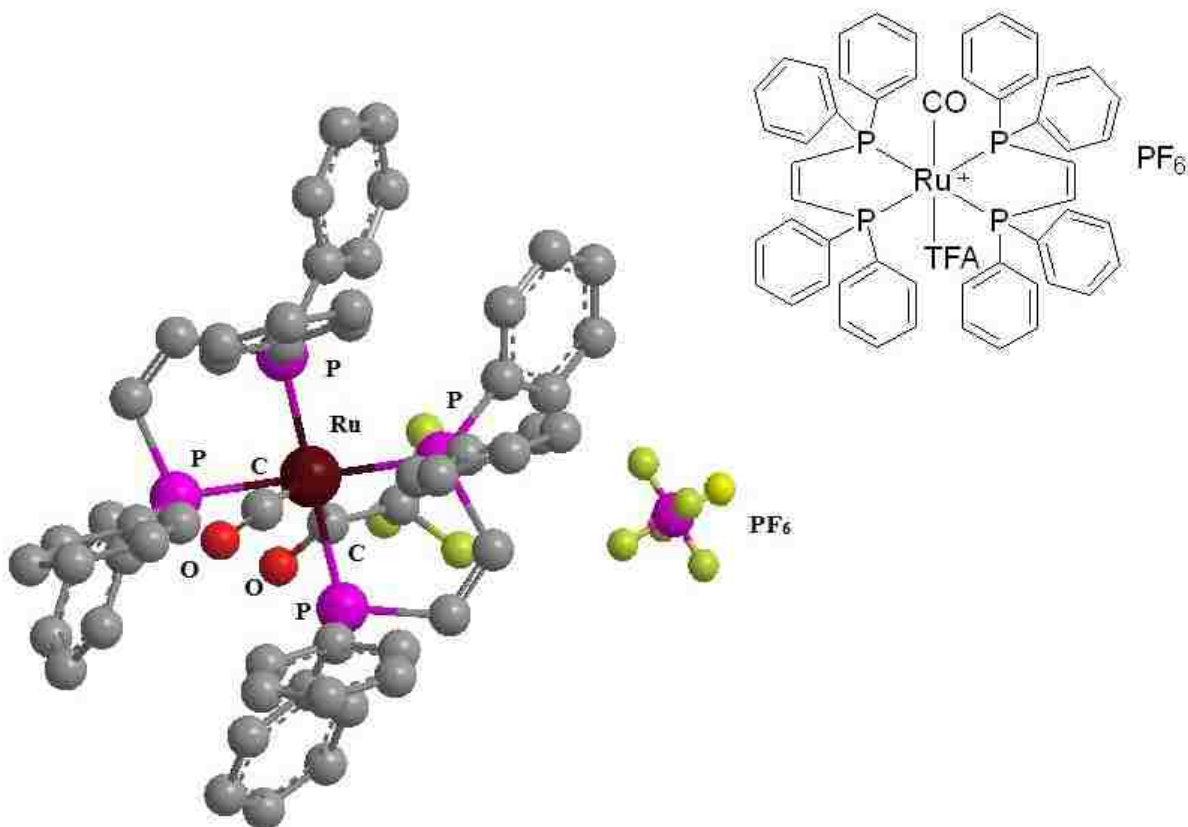


Figure 13 Crystal structure of  $[\text{Ru}(\text{CO})(\text{DPPENE})_2(\text{TFA})][\text{PF}_6]$ (13) complex

## 2.3 Experimental

### 2.3.1 General Methods and Materials

The reactions were carried out under nitrogen. Purification was carried out in air by using preparative thin-layer chromatography (10 × 20 cm plates coated with 1 mm silica gel PF 60254-EM Science). Activated neutral alumina (Aldrich, 150 mesh, 58 Å) was also used to purify compounds by column chromatography. Reagent-grade solvents were purchased from J.T. Baker. Methylene chloride (CH<sub>2</sub>Cl<sub>2</sub>) and acetonitrile (MeCN) were distilled from calcium hydride. Tetrahydrofuran (THF) was distilled from benzophenone ketyl. Ruthenium carbonyl was purchased from Strem Chemicals. Cholesteryl-chloroformate, thiophosgene, 1,10-phen, 5-amino-1,10-phen, bpy, and dcbpy were purchased from Sigma-Aldrich and used as received. 1,2-Dihexadecanoyl-sn-glycero-3-phosphoethanol-amine (DPPE), 1,2-dihexadecanoyl-sn-glycero-3-phosphocholine (DPPC), 1,2-dimyristoyl-sn-glycero-3-phosphocholine (DMPC), and L- $\alpha$ -phosphatidylcholine from chicken egg (egg-PC) were purchased from Avanti Polar Lipids Inc. and used as received. The complexes [(H)Ru(CO)(PPh<sub>3</sub>)<sub>0</sub>(dcbpy)][PF<sub>6</sub>]( 1) and [(H)Ru(CO)(dppene)- (5-amino-1,10-phen)][PF<sub>6</sub>]( 2) were synthesized according to published procedures.<sup>30</sup> The compounds [Ru(bpy)<sub>2</sub>(5-amino-1,10-phen)][PF<sub>6</sub>]<sub>2</sub> (8) and [Ru(bpy)<sub>2</sub>(1,10-phen-5-NHC(S)-N-DPPE)][PF<sub>6</sub>]<sub>2</sub> (10) were synthesized according to literature procedures.<sup>60</sup> <sup>1</sup>H NMR and <sup>31</sup>P {<sup>1</sup>H} NMR spectra were obtained on a Varian 400 MHz Unity Plus or a Varian NMR Systems 500 MHz spectrometer. Fourier transform infrared (FT-IR) spectra were obtained on a Thermo-Nicolet 633 FT-IR spectrometer. Electrospray ionization mass spectrometry (ESI-MS) spectra were obtained on a Waters Micromass LCT using 80% MeCN as the carrier solvent. Luminescence Spectroscopy. Steady-state UV–visible absorption spectra and emission spectra were recorded on a Molecular Device Spectra Max M2. The emission quantum yields ( $\phi$ ) for the



ruthenium complexes in the presence of oxygen were calculated relative to a Rhodamine B standard ( $\phi = 0.73$ , in ethanol).<sup>11,30</sup>  $\phi = \frac{\text{abs Rhodamine B area}}{\text{abs Ru complex}} \times \frac{\text{area Rhodamine B}}{\text{area Ru complex}}$  (1) Here “abs” refers to the absorbance of the luminophores at the excitation wavelength, and “area” refers to the integrated area under the emission spectral curve. In the case of compound 7 the quantum yield was measured by a similar procedure, but because of the blue-shifted emission of this complex, fluorescein was used as the standard.<sup>30b</sup> Details of the methods used for the time-resolved spectroscopy are given in Appendix A.<sup>74,94-96</sup>

### 2.3.2 Synthesis of (H)Ru(CO)(PPh<sub>3</sub>)<sub>2</sub>(dcbpy-N-succinimidyl)[PF<sub>6</sub>](1’).

A mixture of compound 111 (155mg, 0.16mmol) and N-hydroxysuccinimide (34mg, 0.32mmol) was stirred in 4 mL of dry MeCN at room temperature in a 10 mL round-bottom flask until all the reactants dissolved. N,N'-Dicyclohexylcarbodiimide (DCC) (103 mg, 0.48 mmol) was added to the mixture, and the reaction was stirred for three hours. The resulting solid precipitate (dicyclohexylurea) was removed by filtration through a 0.2  $\mu\text{m}$  syringe filter. The filtrate was added to 5mL of isopropanol, and the mixture was kept at  $-4\text{ }^\circ\text{C}$  to complete the precipitation. The supernatant was evaporated, and the remaining orange residue was washed three times with 2 mL aliquots of dry ethyl ether. Compound 1’ was obtained in 32% yield (60 mg). IR in KBr: CO stretching frequency at 1956 (vs), 1775 (m), 1742 (s), 1650 (m) and CH aliphatic  $2980\text{ cm}^{-1}$ . <sup>1</sup>H NMR (CDCl<sub>3</sub>  $\delta$ ): 9.6–7.2 (m, 36H), –11.1 (t, 1H), 2.8 (4H). <sup>31</sup>P {<sup>1</sup>H} NMR (CDCl<sub>3</sub>  $\delta$ ): 49.2 (s, 2P), –155 (m, 1P).

### 2.3.3 Synthesis of [(H)Ru(CO)(PPh<sub>3</sub>)<sub>2</sub>(dcbpy-N-DPPE<sub>2</sub>)] [PF<sub>6</sub>](3).

DPPE (30 mg, 0.043 mmol) was dissolved in CHCl<sub>3</sub>, and 3.5 mL of triethylamine was added to the solution. The mixture was stirred for 15 min, and then a solution of complex 1’ (60 mg, 0.021 mmol) in 2 mL of dry MeCN was added dropwise over 20 min. The reaction was

stirred overnight, and then the solvent was removed by rotary evaporation. The residue was purified by thin layer chromatography on silica gel. Two successive elutions with a mixture of hexane/methylene chloride/ ethanol {6.5:3.5:0.5 (v/v)} yielded two bands. The baseline contained unreacted complex 1'. The faster-moving UV-absorbing band was identified as unreacted DPPE, and the slower-moving deep yellow band gave compound 3 in 15% yield (22 mg). IR in KBr: CO stretching frequency at 1956 (vs), 1734 (s), 1684 (vs) and CH aliphatic 2963 (s), 2924 (s), 2851 (m)  $\text{cm}^{-1}$ .  $^1\text{H}$  NMR ( $\text{CDCl}_3$   $\delta$ ): 9.5–7.0 (m, 36H), 5.2 (2H), 5.1–2.2 (35H), 1.9–0.78 (107H), –11.19 (br, 1H);  $^{31}\text{P}$  { $^1\text{H}$ } NMR ( $\text{CDCl}_3$   $\delta$ ): 49.6 (s, 2P), 25.04 (2P), –155 (m, 1P). ESI-MS:  $m/z$  2034 [ $\text{M}^+ - (\text{C}_{15}\text{H}_{31} + \text{PF}_6)$ ] (calcd  $\text{M}^+ - (\text{C}_{15}\text{H}_{31} + \text{PF}_6) = 2034$ ).

#### 2.3.4 Synthesis of [(H)Ru(CO)(dppene)(1,10-phen-5-NCS)][PF<sub>6</sub>]( 2').

A 122 mg (0.13 mmol) sample of compound 2<sup>30</sup> was dissolved in 3 mL of dry acetone. Finely crushed  $\text{CaCO}_3$  (45 mg, 0.45 mmol) was added to the solution of complex 2 followed by addition of thiophosgene (11  $\mu\text{L}$ , 0.07 mmol). The reaction mixture was stirred at room temperature for 1 h and then refluxed for 2.5 h. After the mixture was cooled to room temperature,  $\text{CaCO}_3$  was removed by using a 0.45  $\mu\text{m}$  filter, and the acetone was removed by rotary evaporation. Compound 2' was obtained in 94% yield (50 mg). IR in KBr: CO stretching frequency at 1990 (vs),  $\text{N}=\text{C}=\text{S}$  at 2119 (m) and 2046 (m)  $\text{cm}^{-1}$ . ESI-MS:  $m/z$  860 [ $\text{M}^+ - \text{PF}_6$ ] (calcd  $\text{M}^+ - \text{PF}_6 = 860$ ).

#### 2.3.5 Synthesis of [(H)Ru(CO)(dppene)(1,10-phen-5-NHC(S)-N-DPPE)][PF<sub>6</sub>]( 4).

A solution of compound 2' (50 mg, 0.049 mmol in 3 mL of dry  $\text{CH}_2\text{Cl}_2$ ) was added dropwise into a stirring solution of DPPE (35 mg, 0.048 mmol in 5 mL of dry  $\text{CH}_2\text{Cl}_2$ ) over 1h at room temperature, and the reaction was stirred overnight. The solvent was removed by rotary evaporation, and the residue was purified by thin- layer chromatography on silica plates. Three

bands were resolved by elution with hexane/methylene chloride/methanol {3:6:2 (v/v)}. The fastest-moving UV-absorbing band was identified as unreacted DPPE, and the second moving yellow band was too small for further characterization. The slowest-moving, deep-yellow band yielded compound 4 in 10% yield (15 mg). IR in KBr: CO stretching frequency at 1993 (vs), 1735 (vs),  $\text{cm}^{-1}$ ; NH stretching at 3422 and aliphatic C–H stretching at 2920 (vs), 2849 (vs)  $\text{cm}^{-1}$ .  $^1\text{H}$  NMR ( $\text{CDCl}_3$   $\delta$ ): 7.5–6.6 (m, 29H), 5.32 (s, br 1H), 4.0–3.4 (m, 9H), 2.9–0.2 (63H), –7.80 (1H).  $^{31}\text{P}$  { $^1\text{H}$ } NMR ( $\text{CDCl}_3$   $\delta$ ): 68.30 (s, 2P), 58.19 (br, 1P), –145 (m, 1P).

### **2.3.6 Synthesis of [(H)Ru(CO)(dppene)(1,10-phen-5-NHC(O)OChol)][PF<sub>6</sub>](5) (Chol = cholesteryl).**

In 15 mL of dry  $\text{CH}_2\text{Cl}_2$  and 1 mL of dry MeCN, 100 mg (0.10 mmol) of compound 2 was dissolved, and then 1 mL of triethylamine was added to the deoxygenated solution. A 10 mL  $\text{CH}_2\text{Cl}_2$  solution of cholesteryl-chloroformate (45 mg, 0.10 mmol) was added to the probe solution dropwise over 20 min, and the mixture was refluxed for 5 h. Progress of the reaction was monitored by the disappearance of the peak at  $1776\text{ cm}^{-1}$  in the IR spectrum, corresponding to the chloroformate, and by the appearance of a new peak at  $1730\text{ cm}^{-1}$ , corresponding to the amide. The solvent was removed by rotary evaporation, and the residue was purified by thin layer chromatography on silica gel. Elution with hexane/methylene chloride/methanol {1:1:1 (v/v)} yielded two bands. Compound 5 was recovered in 20% yield (30 mg) from the orange, slower-moving band while the faster UV-absorbing band contained unreacted cholesteryl-chloroformate. IR in KBr: CO stretching frequency at 1997 (vs), 1976 (vs), 1735 (s), and CH aliphatic 3054 (w), 2926 (vs), 2850 (s)  $\text{cm}^{-1}$ .  $^1\text{H}$  NMR ( $\text{CDCl}_3$   $\delta$ ): 8.5–6.5 (m, 29H), 6.05 (2m, 1H), 4.3 (s, 1H), 2.0–0.5 (44 H), –7.90 (m, 1H).  $^{31}\text{P}$  { $^1\text{H}$ } NMR ( $\text{CDCl}_3$   $\delta$ ): 75.71 (s, 2P), –145 (m, 1P).

### 2.3.7 Synthesis of [(TFA)<sub>2</sub>Ru(CO)<sub>2</sub>(PPh<sub>2</sub>C<sub>2</sub>H<sub>4</sub>C(O)OH)] (TFA = Trifluoroacetic Acid)(6).

A THF solution of K[Ru(CF<sub>3</sub>CO<sub>2</sub>)<sub>3</sub>(CO)<sub>3</sub>]<sup>30</sup> (500mg, 0.90mmol) and 3-(diphenylphosphino) propionic acid (DPPA)(425mg, 1.8 mmol) was heated overnight at 45 °C. The solvent was removed by rotary evaporation, and the residue was vacuum dried yielding 625 mg (81%) of complex 6 as a pale yellow solid. IR in KBr: 2023 (vs), 2010 (vs), 1960 (m), 1790 (m, br), 1685 (vs, br) cm<sup>-1</sup>. <sup>1</sup>H NMR in acetone-d<sub>6</sub>: δ 7.9–7.3 (m, 20H), 3.90 (m, 2.8H, isomer a), 3.14 (m, 1.2H, isomer b), 2.57 (m, 1.2H, isomer b), 2.10 (m, 2.8H, isomer); <sup>31</sup>P {<sup>1</sup>H} NMR: δ 26.59 (d, t, br).

### 2.3.8 Synthesis of [(H)Ru(CO)(PPh<sub>2</sub>C<sub>2</sub>H<sub>4</sub>C(O)OH)<sub>2</sub>(bpy)][PF<sub>6</sub>](6').

The reaction of complex 6 (300 mg, 0.35 mmol) with bpy (55 mg, 0.35 mmol) in ethylene glycol (15 mL) was heated at 140 °C for 72 h producing an orange solution. A deep-orange precipitate was obtained by the addition of NH<sub>4</sub>PF<sub>6</sub> in deionized (DI) water (1.0 g/10 mL) dropwise until precipitation was completed. The precipitate was filtered and washed three times with cold DI water, three times with diethyl ether, and dried under vacuum. Complex 6' was obtained in 41% yield (135 mg). IR in KBr: 1971 (vs), 1730 (s), 1740 (vs), 1605 (s) cm<sup>-1</sup>. <sup>1</sup>H NMR in acetone-d<sub>6</sub>: δ 8.38–6.95 (m, 28H), 3.99 (t, 4H), 3.61 (t, 4H), -11.1 (t, 1H); <sup>31</sup>P {<sup>1</sup>H} NMR: δ 43.06 (s, 2P), -145 (m, 1P).

### 2.3.9 Synthesis of [(H)(CO)Ru(PPh<sub>2</sub>C<sub>2</sub>H<sub>4</sub>C(O)-N-succinimidyl)<sub>2</sub>(bpy)][PF<sub>6</sub>](6'').

The succinimidyl derivative was obtained by dissolving complex 6'(100 mg, 0.106 mmol) in 5mL of MeCN in a round-bottom flask at 0 °C along with N-hydroxysuccinimide (25 mg, 0.212 mmol) and DCC (65 mg, 0.32 mmol) overnight. After it was stirred, the reaction mixture was passed through a 0.2 μm syringe filter to remove urea that had precipitated. The filtrate was added to an excess of cold isopropanol and recrystallized. The resulting precipitate

was filtered and washed three times with diethyl ether. Complex 6'' was obtained in 58% yield (70 mg, 0.061 mmol). IR in KBr: CO stretching frequency at 1939 (s), 1780 (s), 1736 (vs) and CH aliphatic 2930 (vs), 2853 (s)  $\text{cm}^{-1}$ .  $^1\text{H}$  NMR ( $\text{CDCl}_3$   $\delta$ ): 8.6–6.7 (28H), 4.3–3.2 (8H), 2.95–2.8 (t, 8H), –11.3 (t, 1H).  $^{31}\text{P}$  { $^1\text{H}$ } NMR:  $\delta$  35.4 (2P) and –145 (1P).

### 2.3.10 Synthesis of [(H)(CO)Ru(PPh<sub>2</sub>C<sub>2</sub>H<sub>4</sub>C(O)-N-DPPE)<sub>2</sub>(bpy)][PF<sub>6</sub>]( 7).

A MeCN solution of complex 6'' (60 mg, 0.048 mmol) was added dropwise into a stirring methylene chloride solution of DPPE (68 mg, 0.096 mmol) in the presence of a catalytic amount of triethylamine. The reaction mixture was stirred overnight at ambient temperature. The solvent was removed on a rotary evaporator, and the residue was purified by thin-layer chromatography on silica. Elution with hexane/methylene chloride/methanol (6:3:1) on silica gave a slower-moving yellow band and a faster-moving UV band with a heavy yellow baseline. The yellow compound on the baseline and the UV-absorbing band were identified as unreacted complex 6'' and DPPE, respectively. The yellow band on the TLC plate gave compound 7 in 20% (~20 mg) yield. IR in KBr: CO stretching frequency at 1941 (s), 1735 (vs), 1653 (m) and CH aliphatic 2960 (s), 2918 (vs), 2850 (s)  $\text{cm}^{-1}$ .  $^1\text{H}$  NMR ( $\text{CDCl}_3$   $\delta$ ): 8.6–6.7 (28H), 5.2–3.2 (44H), 3.0–0.4 (108H), –11.1 (t, 1H). Peaks in both the aliphatic and the aromatic regions were broad. The  $^{31}\text{P}$  NMR showed that the phosphine peak and the phosphate peak of the lipid were also broad and appeared at  $\delta$  37.94 (2P) and 22.5 (2P), respectively; the PF<sub>6</sub> peak was at  $\delta$  –145 (1P).

### 2.3.11 Synthesis of [Ru(bpy)<sub>2</sub>(1,10-phen-5-NHC(O)OChol)][PF<sub>6</sub>]<sub>2</sub> (9).

Complex 8 was prepared according to a published method.<sup>39</sup> Complex 8 (100 mg, 0.11 mmol) was dissolved in 10 mL of dry  $\text{CH}_2\text{Cl}_2$ , and then 1 mL of triethylamine was added to the deoxygenated solution. A 5 mL  $\text{CH}_2\text{Cl}_2$  solution of cholesteryl-chloroformate (50 mg, 0.11

mmol) was added to the probe-containing solution dropwise over 20 min, and the reaction mixture was refluxed for 4 h. Progress of the reaction was monitored by the disappearance of the peak at  $1776\text{ cm}^{-1}$  in the IR spectrum, corresponding to the chloroformate, and by the appearance of a new peak at  $1731\text{ cm}^{-1}$ , corresponding to the amide. The solvent was removed by rotary evaporation, and the residue was purified by thin layer chromatography on silica gel. Elution with the solvent mixture hexane/methylene chloride/methanol {1:2:1 (v/v)} yielded two bands. The complex 9 was recovered in 14% yield (23 mg) from the orange, slower-moving band while the faster, UV-absorbing band contained unreacted cholesteryl-chloroformate. IR (KBr) ( $\text{vcm}^{-1}$ ): CO stretching frequency at 1731 (s) and CH aliphatic 3139 (w), 2950 (vs), 2868 (s).  $^1\text{H}$  NMR ( $\text{CDCl}_3$   $\delta$ ): 8.7–7.0 (24H), 5.37 (1H), 3.99 (1H), 2.0–0.5 (43 H).

### 2.3.12 Synthesis of trans-[Ru(CO)(DPPENE)<sub>2</sub>(TFA)][PF<sub>6</sub>] (13)

100mg Ru(CO)<sub>2</sub>(DPPENE)(TFA)<sub>2</sub><sup>30</sup>(.128mmol) was dissolved in 20mL of 1:1 Ether:Acetone along with 52mg DPPENE (.128mmol) and refluxed for 2 hours. After 2 hours the solvent was removed via rotary evaporation. After solvent removal the product was recrystallized using an acetone:hexane mixture overnight in a -20°C freezer. After recrystallization 70mg(0.069mmol) of clear crystalline product was collected via filtration and dried under vacuum overnight. IR in KBr: CO stretching frequency at 1994(s, metal CO), 1684(s,b, TFA CO) $\text{cm}^{-1}$ .  $^1\text{H}$  NMR ( $\text{d}_6$ -Acetone  $\delta$ ): 8.36(t, 4H), 7.52(t, 8H), 7.32(overlapping triplet, 14H), 7.13(d,b, 14H), 3.77(s,b 4H).  $^{31}\text{P}$  { $^1\text{H}$ } 49.73(s, 4P)(DPPENE), 144.22(q, 1P)(PF<sub>6</sub>).  $^{19}\text{F}$  102.84 (s, 3F)(TFA), 104.8(d, 6F)(PF<sub>6</sub>)

### 2.3.13 LUV Preparation.

A chloroform mixture of the conjugated probe (3, 4, 5, or 7) and DPPC, DMPC, or a mixture of phospholipids containing a choline head group (egg-PC) was prepared in a molar ratio

of 1:99. The organic solvent was removed by evaporation with argon gas, and the lipid/chromophore mixture was further dried under vacuum overnight. Then 0.52 mL of saline buffer (20 mM N-(2-hydroxyethyl)piperazine- N'-ethanesulfonic acid, 100 mM NaCl, pH 7.5) was added to the dried lipid, and the solution was maintained above the phase-transition temperature of the corresponding phosphocholine (41 °C for DPPC, 23°C for DMPC, and less than 0°C for egg-PC)<sup>96</sup> to obtain a final lipid concentration of 1 mM. Addition of the buffer to the lipid mixture produced cloudy suspensions. The suspensions were incubated above the phase-transition temperature for 1 h with occasional stirring. Then a freeze/thaw cycle was carried out 5 times. Finally, clear suspensions of ~100 nm diameter LUVs were obtained by extrusion through a 100 nm sizing membrane as previously described.<sup>91</sup>

## Chapter 3 Silica Polyamine Composite Technology on the Nanoscale

### 3.1 Introduction

As materials technology has evolved the goal has always been to create the most efficient surface for a given task. Often this means optimizing the surface area while decreasing the volume. The ideal size is nanoparticles, 10-20nm diameter particles, where their surface area is approximately equal to the volume. These particles maximize surface area while still maintaining a surface which can do novel chemistry, and be easily separated from a solution.

SPC technology has been extensively studied at the macro, 150-600 micron diameter, level and even commercialized for the capture and reclaiming of metals from mine drainage<sup>19,40-55,57,97-107</sup>. As with any material research it is believed that by moving to the nanoscale SPC technology could be further improved by improving the surface area to volume ratio of the materials.<sup>108</sup> SPC technology could have limits at the nanoscale level though, as the polymers that are often used in the synthesis of the materials are large and could lead to aggregation. In order to explore the role of both the particle size and polymer in the SPC technology, initial experiments were done using a monomer analog of the polymers, as well as varying low molecular weight polymers of PEI. Once it was determined that the chemistry could be performed on the nanoparticles, the commercially available analogs were made using the high molecular weight PEI and PAA. Scheme 1 shows the general synthetic schemes for creation of the SPC's with either the PEI or PAA polymer.

This study will also investigate the effects of nanoscale SPC's as they would apply beyond the application of metal capture as well. Using the relatively simple Knoevenagel condensation between benzaldehyde and ethyl cyanoacetate, which is catalyzed through primary amines, the effectiveness of the materials as catalytic platforms can also be evaluated.<sup>109,110</sup> The



catalytic reaction will also elucidate whether particle size has any effect on more dynamic processes involving the polymers on the SPCs.

## **3.2 Results**

### **3.2.1 Composite nomenclature**

The composites are named by the first two letters of the polymer or aminopropyl to which the complex is bound: PA for PAA(BP-1); PE for PEI (WP-1); and AP for aminopropyl. The micro-particle composites have the letter prefix M (e.g., MPA) and the nanoparticles have the letter prefix N (e.g. NPA). The complex is designated by its number (e.g. **MPA-1** means complex **1** bound to PAA on the micro-particle BP-1, SPC).

### **3.2.2 Synthesis**

Initial testing between the micro and nano scale particles was done using the monomer analog of the SPC's, a 3- aminopropyl coated surface. The goal of these initial tests was to ensure that the chemistry used on the 150-250 micron particles would still apply to the nanoscale. Both functionalization reactions were carried out under similar conditions, room temperature in toluene with 15% by weight of the monomer, the only difference being that the nanoparticles were sonicated to minimize aggregates, while the micro particles were top-stirred in order to prevent particle degradation through grinding.

After synthesizing the monomer analog without issue on the nanoscale, a series of materials were synthesized using increasing molecular weights of PEI to investigate if there was a polymer weight boundary which would cause issues of aggregation between nanoparticles. PEI was chosen because PAA only comes in the molecular weight of 15,000. In order to bind the polymer the silica surface must be coated with anchor points, which were unnecessary with the monomer analog. These anchor points were created by reacting the unmodified silica

particles with either pure 3-chloropropyl trimethoxy silane, or a mixture of methyl trimethoxy silane and 3-chloropropyl trimethoxy silane, which has been shown to improve the metal capture abilities of the micro particle analogs. In the commercially produced analogs this mixture is done at 7:1 methyl:chloropropyl, in these studies we will also compare other ratios as well to ensure that the same processes are occurring at the nanoscale that occur at the micro scale.

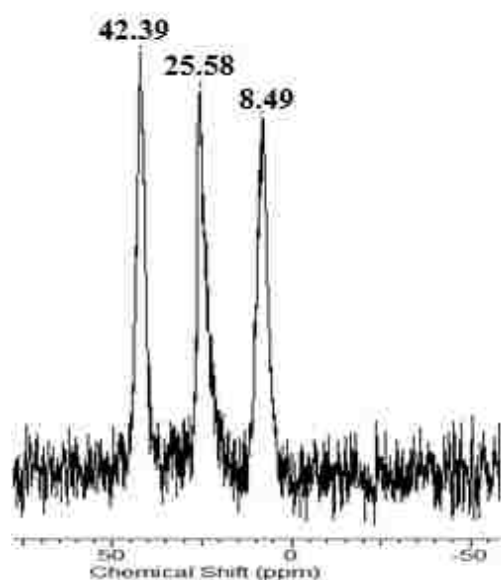


**Figure 14** <sup>13</sup>C SS-NMR Shifts for Aminopropyl coated particles

During the synthesis of all the materials no aggregation could be visually identified, each nanoparticle material maintained a very fine powdery physical appearance, even as the molecular weight of the polymer was increased. After initial syntheses using the lower molecular weight polymers had no issues, the higher molecular weight polymers that would be analogous to the commercially available materials was used, 25,000 MW PEI as well as 15,000 MW PAA. These

materials as well showed no physical signs of aggregation and this was confirmed by using SEM and TEM images of the modified and unmodified silica, which showed no visible increase in the size of the aggregates that formed during the mounting process for the images.

### 3.2.3 NMR, Elemental Analysis and Copper Capacity

Once synthesized all of the materials were compared using C<sup>13</sup> and Si<sup>29</sup> SSNMR, to ensure the monomer bound to the surface, as well elemental analysis to quantify the amount of monomer loaded. Comparison of chlorine in the elemental analysis between the chloropropyl intermediates and final SPC nano materials allows for the determination of the number of anchor

points the polymer has on the surface. Copper capacities were also performed to see how the size affected performance of metal ion capture.

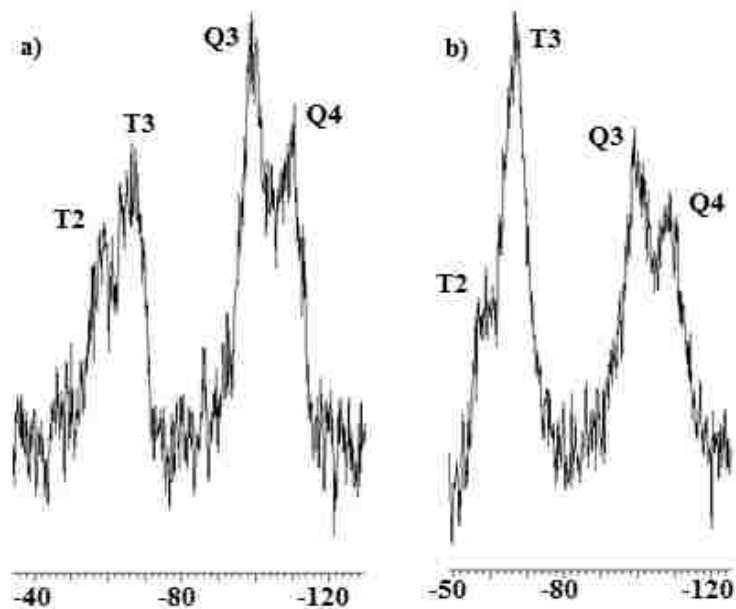


Figure 15 Comparison of (a) MAP vs (b) NAP <sup>29</sup>Si SSNMR Spectra

<sup>13</sup>C SSNMR for the **MAP** and **NAP** materials both show very strong sharp peaks for the 1,2 and 3 carbons of the amino propyl chain at 8, 25, and 42 ppm respectively, indicating that the monomer is on the surface (Figure 14). The <sup>29</sup>Si both show the expected T groups indicating that the aminopropyl groups are

covalently bound to the surface, both T and Q groups are explained in Chart 1. The ratio of T to Q groups for the nanoparticles is larger than that of the microparticle indicating that there is a higher percentage of surface coverage of the nanoparticles than there is for the microparticles (Figure 15).

These results are further supported by the elemental analysis of the **MAP** and **NAP** materials,

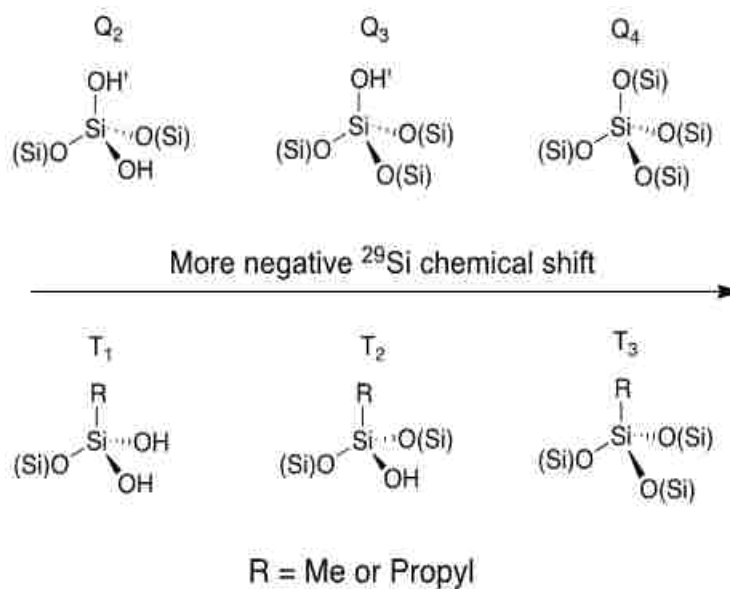


Chart 1 Definition of T and Q peaks in <sup>29</sup>Si SSNMR

which shows a nitrogen content of 2.37 and 3.21 mmol N/g respectively. However, the copper capacity data does not show as large a difference with the **MAP** material having a copper capacity of 1.2 mmol/g and the **NAP** having only a slightly higher value of 1.4 mmol/g. This along with the coordination number of 2.3 vs 2.0 for the **NAP** vs. **MAP** indicates that there are more unused nitrogen groups on the nano material than on the micro. These values are similar for the commercially available BP-1 which is the PAA polymer on a microparticle, which has a copper capacity of 1.6 mmol/g and a copper coordination of 1.4, indicating that the polymer is a more efficient metal capturing material than the monomer (Table 5).

**Table 5. Comparison of the Properties of Micro- and Nano-SPC**

SPC	Functional	Particle size	MW	N mmol g <sup>-1</sup>	Cu Capacity mmol g <sup>-1</sup>	N:Cu Ratio
<b>MPE</b>	PEI	150-300 μm	25k	2.21	1.1	2.0
<b>MPA</b>	PAA	150-300 μm	15k	1.63	1.6	1.0
<b>NAP</b>	APTMS	10-20 nm	-	2.29	1.4	1.6
<b>MAP</b>	APTMS	150-300 μm	-	1.69	1.2	1.4
<b>NPE</b>	PEI	10-20 nm	25k	2.73	0.6	4.6
<b>NPA</b>	PAA	10-20-nm	15k	2.16	2.1	1.0

The polymer studies were done starting with 300, 600, 1200 and 1800MW PEI, on silica nanoparticles that were either coated with 3-chloropropyl trimethoxy silane or a 7:1 mixture of methyl trimethoxy silane and 3-chloropropyl trimethoxy silane. The C<sup>13</sup> SSNMR of the chloropropyl and mixed silane material again show 3 sharp peaks for the chloropropyl at 8, 23 and 43ppm, with the mixed silane material containing a large methyl silyl peak at -6ppm as well.

The  $^{29}\text{Si}$  show the expected T and Q peaks corresponding to covalent bonding of the anchor groups to the surface of the silica, however, these materials also showed a  $T_1$  and  $Q_2$  peaks that were absent in the monomer aminopropyl NMRs which indicates a higher level of surface hydrolysis is occurring with these materials( Figure 16).

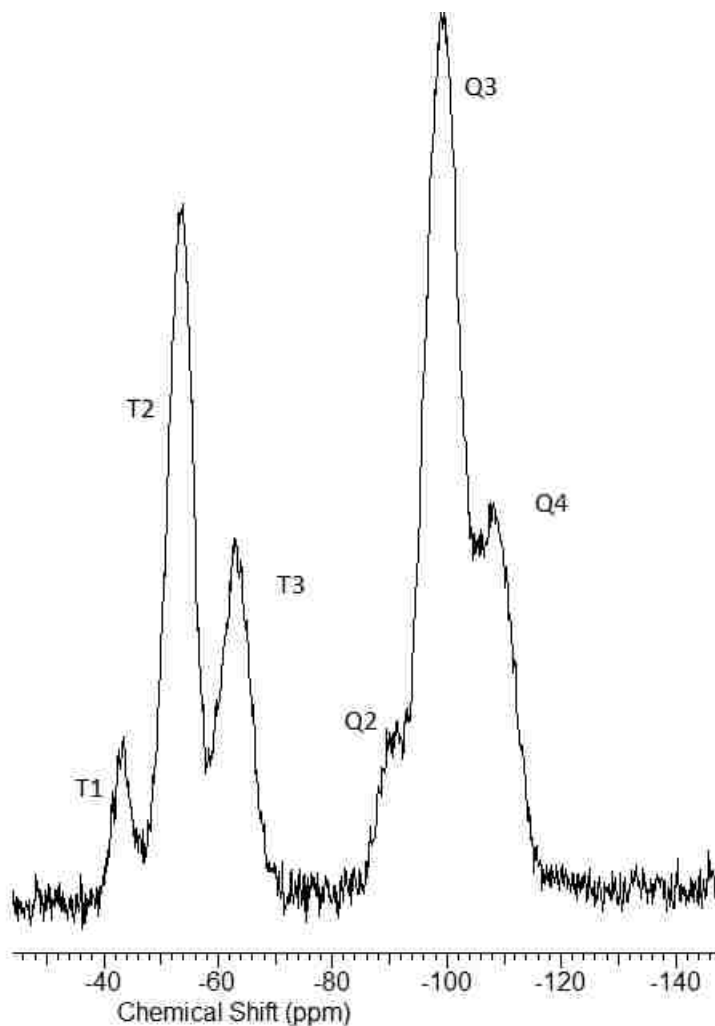


**Figure 16**  $^{29}\text{Si}$  SSNMR of 7:1 Methyl:Chloropropyl coated nanoparticles.

After reaction with the polymer a distinct broad signal appears in the alkane region of the  $\text{C}^{13}$  SSNMR indicating that the polymer has been bound to the chloropropyl groups. This polymer region can be seen in all the low molecular weight polymers indicating that the increasing polymer weight has little effect on the binding to the surface. The  $^{29}\text{Si}$  NMR shows a

distinct change over the MTMS and MTMS:CPTMS materials in that the T<sub>1</sub> and Q<sub>2</sub> peaks seen before reaction have been reduced as well as the T<sub>3</sub> peaks are now more dominant than the T<sub>2</sub>.

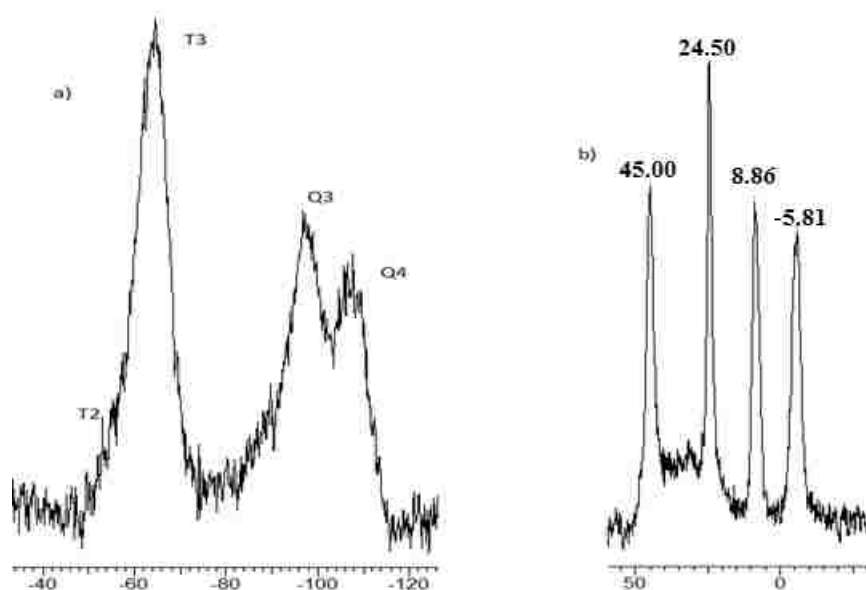


Figure 17 <sup>29</sup>Si (a) and <sup>13</sup>C (b) SSNMR of 7:1 MTMS:CPTMS nanoparticles reacted with PAA at 80°C

This is taken as the addition of the polymer has catalyzed the reaction of surface hydroxyls with the alkyl silanes pushing the reaction to completion.

With the study on the low molecular weight polymers showing no changes based on the increasing molecular weight, we moved on to make materials using higher molecular weight materials using 10,000MW PEI and analogs of the commercially produce materials with 25,000MW PEI and 15,000MW PAA. These materials showed very similar NMR profiles both in the C<sup>13</sup> and Si<sup>29</sup> SSNMRs as the previous low molecular weight materials had (Figure 17). Elemental analysis was done on the commercial analogs for comparison and both nano materials showed an increased level of nitrogen bound than their micro analogs. The analyses also showed that as expected when using the mixed silane coating the number of anchor points decreased which has been previously shown to improve metal loading and capture kinetics. The nano materials though consistently had a lower chloride utilization however the number of anchor

points for the PAA was higher in both the CPTMS and mixed silane material. This fact can be attributed to the higher levels of surface loading for the CPTMS on the nanoparticles than the microparticles on both materials (Table 6).

**Table 6. Anchor Points and Copper Capacities for Micro and Nano-SPC**

Composite	# anchor points	% Cl utilized	Cu Capacity mg/g
PEI CPTMS only-nano	178	64	39
PEI CPTCS only micro	230	80	65
PAA CPTMS only nano	154	45	136
PAA CPTCS only micro	105	80	90
PAA 7: 1 mix of CPTMS and MTMS nano	41	27	130
PAA 7:1 mix of CPTCS and MTCS only micro	24	81	100
PAA Sol-gel micro 4.5: :1:1*	38	38	100
PAA sol-gel micro 62:30:1*	13	51	118

Copper capacities done on the various molecular weights of PEI showed only minor variation between molecular weights of polymer, however, the CPTMS only materials had higher capacities at every molecular weight polymer except 10,000MW which was about equal to its mixed silane analog. The copper loading data for the nano-analog of the commercially available 25,000 MW material showed that it had only about 50% of the copper capacity as that of the microparticle material. This indicates that even though there are more amines loaded on the nano material the availability of these amines for metal capture is greatly reduced.<sup>53</sup>

The PAA micro and nano analogs show a much different pattern than that of the PEI polymer, with the nano material performing better at metal capture than the micro analog. The

copper capacities for the micro and nano materials are 1.6 and 2.1 mmol/g respectively. When the coordination number for amines to copper is calculated for these materials both give a value of 1.4, indicating that polymer is behaving the same on both materials, there is just more loaded per gram on the nanoparticles (Table 7).

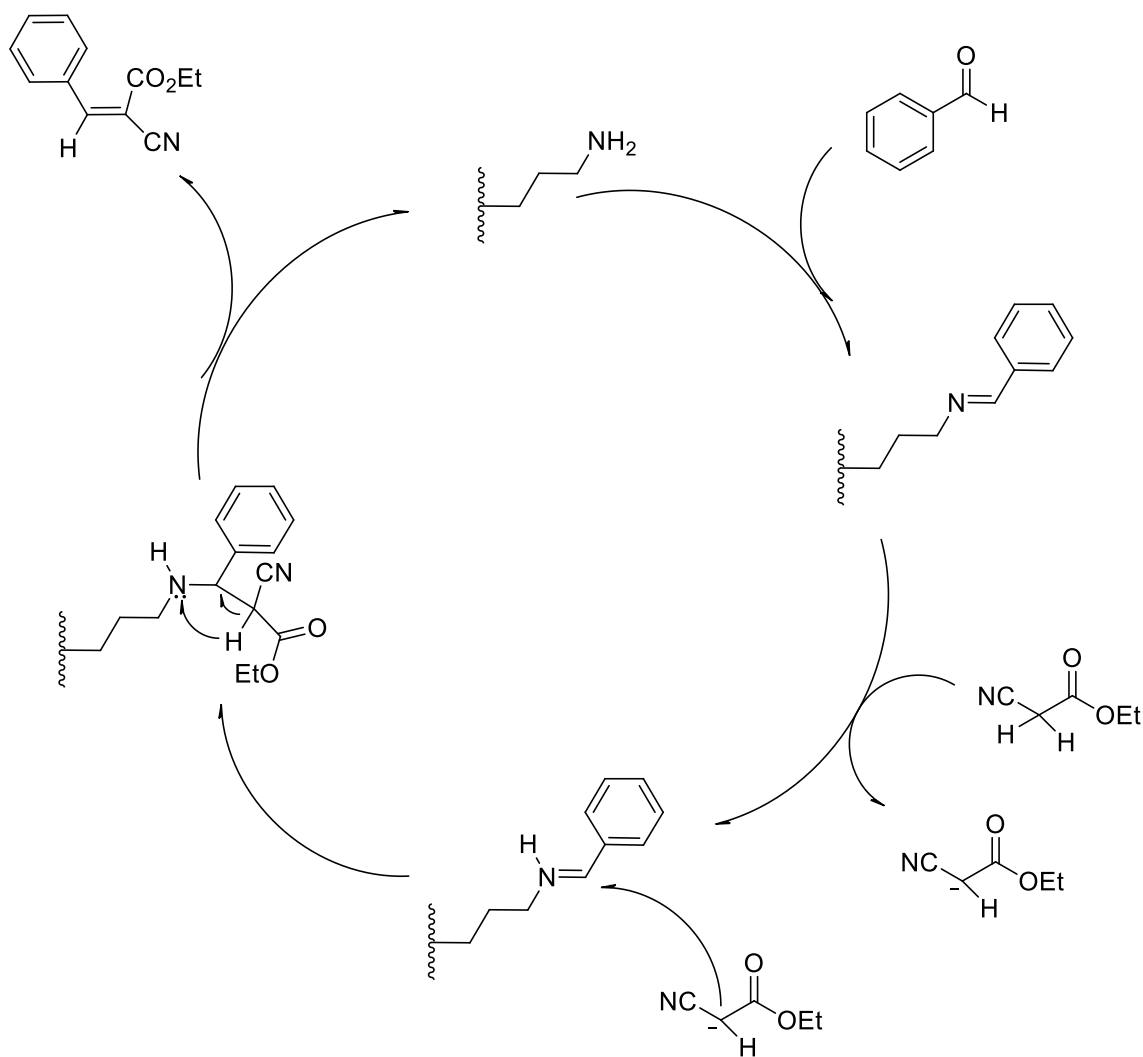
### 3.2.4 Catalysis

Once the SPC chemistry was shown to be viable on the nano scale, and some improvement was seen in metal capacity, a simple catalysis experiment was performed to see if the nano materials would perform as well as the micro materials in a more dynamic process. As one of the goals for the SPCs is to use them as a heterogeneous catalysis platform, it was decided that a simple catalytic experiment would determine if the nano scale materials were also a viable platform. The chosen reaction was the Knoevenagel condensation between benzaldehyde and ethyl cyanoacetate, which is catalyzed by amines.<sup>109</sup>

**Table 7. Variation in Copper Capacities for Nano-SPC Made with PEI (MW=300-25k)**

Polymer	mmol Cu/gram composite
PEI 300 MW	0.64
PEI 600 MW	0.55
PEI 1200 MW	0.54
PEI 1800 MW	0.48
PEI 10,000 MW	0.62
PEI 25,000 MW	0.61
PAA 15,000 MW	2.14
PAA 15,000 MW	2.04





**Scheme 5 Knoevenagel Catalytic Cycle**

Initial testing was done with the micro scale materials between the commercially available PEI material and the PAA material as well as the 3-Aaminopropyl material. The results of these tests showed that the aminopropyl had the fastest rate at  $.50 \text{ M}^{-1}\text{s}^{-1}$  while PAA and PEI materials had rates of  $.25 \text{ M}^{-1}\text{s}^{-1}$  and  $.11 \text{ M}^{-1}\text{s}^{-1}$  respectively. This result can be explained by the fact that the 3-AP material has amines that are in a much more freely accessible and more properly oriented manner than the PAA and PEI. The PEI was the worst catalyst as not only is it the most hindered system of the 3 but it also has the fewest primary amines available for catalysis.

For comparison to the nanoparticles the **NAP** material was chosen as it had shown the best performance on the microscale. Initial experiments seemed to show that the nanoparticles were very poor catalytic platforms as they had a very slow rate initially that would only increase after ~30 minutes, however, it was realized that this is likely due to the nanoparticles having to individualize from the aggregates that form when they are dry. By sonicating for 30 minutes prior to addition of the reactants the performance of the material improved, but still had a slightly lower rate,  $.33\text{M}^{-1}\text{s}^{-1}$ , than the microparticle analog. Even with the presonation there was still some lag time before the nanoparticles began catalyzing the reaction. The result of the microparticles outperforming the nanoparticles could be due to the slightly lower loading of 3-AP on the microparticle surface than the nanoparticles. By having a much higher density on the nanoparticles access to amines by reactants in solution could be hindered by the reactants already complexed with the surface.

We also tested how 2 materials performed on a second cycle of catalysis, the **MPA** and **MAP** materials were collected after their first cycle, dried and reacted for a second cycle. Again the **MAP** material performed best, with a slight drop in rate, now  $.33\text{M}^{-1}\text{s}^{-1}$ , and conversion. The **MPA** material on the other hand showed a significant decrease in both rate,  $.056\text{M}^{-1}\text{s}^{-1}$ , and percent conversion. This is likely due to the **MPA** have a more stable imine intermediate, Scheme 5, that doesn't convert back into the primary amine the way the **MAP** material does, allowing only one cycle of reaction to occur at most amine sites (Table 8).

**Table 8. Second order rate constants for the SPC catalyzed Knoevenagel reaction**

<b>Material</b>	<b>Particle Size</b>	<b>Run No.</b>	<b>Reactant Conc.</b>	<b>%Conversion<sup>a</sup></b>	<b>Rate Constant (M<sup>-1</sup>s<sup>-1</sup>)</b>	<b>R<sup>2</sup></b>
<b>MPA</b>	Micro	1	.1M	79	0.25	0.99
<b>MPE</b>	Micro	1	.1M	45	0.11	0.94
<b>MAP</b>	Micro	1	.1M	95	0.50	0.97
<b>Silica</b>	Micro	1	.1M	0	0	N/A
<b>NAP</b>	Nano <sup>b</sup>	1	.1M	85	0.33	0.95
<b>Silica</b>	Nano	1	.1M	0	0	N/A
<b>MPA</b>	Micro	2	.1M	24	0.056	0.81
<b>MAP</b>	Micro	2	.1M	90	0.33	0.98

<sup>a</sup> reactions were monitored for 1 hour in toluene at room temperature using 0.1g of catalyst.

<sup>b</sup> nano reaction was sonicated for 30 minutes before starting the reaction

### 3.3 Materials and Methods

#### 3.3.1 Materials

Microparticle silica gel was obtained from INEOS Chemical and sieved to obtain particles in the 150-250 micron range and dried at 120°C before use. SiO<sub>2</sub> nanoparticles, 10-20nm diameter, were obtained from Sigma-Aldrich, and dried at 120°C before use. The monomer 3-aminopropyl trimethoxy silane was obtained from Alfa Aesar, while the methyl trimethoxy silane and 3-chloropropyl trimethoxy silane, were obtained from Gelest. The polyallyl amine, 15,000MW was purchased from Polysciences Inc, and the polyethylene imine, varying molecular weights, was purchased from Nikon Shokubai. The polymers and silanes were used without any further purification. Toluene was obtained from Alfa Aesar and dried using molecular sieves before use.

### 3.3.2 Methods

$^{29}\text{Si}$  and  $^{13}\text{C}$  Solid state NMR were performed on a Varian 500MHz at 125 and 99.4MHz respectively. Samples were spun at the magic angle at a speed of 10KHz on a 4mm narrow bore rotor. Copper capacities were determined using the method previously reported in the literature, using a Thermo Scientific Corporation AA spectrometer.

### 3.3.3 Synthesis

The micro scale BP-1 and WP-1 were previously synthesized in the lab by published procedures, using a 7.5:1 mixture of methyltrichlorosilane to 3-chloropropyltrichlorosilane.

#### 3.3.3.1 Synthesis of 3-aminopropyl coated microparticles (MAP)

1g of dried INEOS silica particles were added to 20mL of a 10% (v/v) mixture of 3-aminopropyl trimethoxysilane in toluene. The mixture was then top stirred at room temperature for 30min. The particles were then filtered and washed with 20mL of toluene 3 times by top stirring for 30 min. After the final wash the particles were dried on a Hi-Vacuum line overnight.  $^{13}\text{C}\{^1\text{H}\}$  SSNMR  $\delta$  8(Propyl C<sub>1</sub>), 25(Propyl C<sub>2</sub>), 42 (Propyl C<sub>3</sub>).

#### 3.3.3.2 Synthesis of 3-aminopropyl coated nanoparticles. (NAP)

1g of dried silica nanoparticles were added to 20mL of a 10% (v/v) mixture of 3-aminopropyl trimethoxysilane in toluene. The mixture was then sonicated at room temperature for 30min. The particles were then centrifuged down at 16,000 RPM and washed with 20mL of toluene 3 times by sonication for 30 min followed by centrifugation. After the final wash the particles were dried on a Hi-Vacuum line overnight.  $^{13}\text{C}\{^1\text{H}\}$  SSNMR  $\delta$  8(Propyl C<sub>1</sub>), 25(Propyl C<sub>2</sub>), 42 (Propyl C<sub>3</sub>)

### 3.3.3.3 Synthesis of 3-Chloropropyltrimethoxysilane coated nanoparticles

1g of dried silica nanoparticles were added to 20mL of a 10% (v/v) solution of 3-chloropropyltrimethoxysilane in toluene and sonicated at room temperature for 30 min. The particles were then centrifuged down at 16,000 RPM and washed with 20mL of toluene 3 times by sonication for 30 min followed by centrifugation. After the final wash the particles were dried on a Hi-Vacuum line overnight.  $^{13}\text{C}\{^1\text{H}\}$  SSNMR  $\delta$  8(Propyl C<sub>1</sub>), 23(Propyl C<sub>2</sub>), 43 (Propyl C<sub>3</sub>).

### 3.3.3.4 Synthesis of 7:1 Methyltrimethoxysilane to 3-Chloropropyltrimethoxysilane coated nanoparticles

1g of dried silica nanoparticles were added to 20mL of a 10% (v/v) solution of 7:1 methyltrimethoxysilane to 3-chloropropyltrimethoxysilane in toluene and sonicated at room temperature for 30 min. The particles were then centrifuged down at 16,000 RPM and washed with 20mL of toluene 3 times by sonication for 30 min followed by centrifugation. After the final wash the particles were dried on a Hi-Vacuum line overnight.  $^{13}\text{C}\{^1\text{H}\}$  SSNMR  $\delta$  8(Propyl C<sub>1</sub>), 23(Propyl C<sub>2</sub>), 43 (Propyl C<sub>3</sub>), -6(Si-Me).

### 3.3.3.5 Synthesis of WP-1 nanoparticles (NPE)

500mg of either CPTMS only or 7:1 MTMS:CPTMS coated nanoparticles were added to 11mL of 18% (w/w) solution of PEI of varying molecular weights in DI water and .5mL of MeOH was added to prevent foaming. The mixture was sonicated at room temperature for 24hrs. After the reaction the nanoparticles were centrifuged down at 16,000 RPM and washed 2x with 20mL of a 1:1 mixture of MeOH and DI water, and 1x was with DI water only, washes were done by sonication for 30 min followed by centrifugation.  $^{13}\text{C}\{^1\text{H}\}$  SSNMR  $\delta$  8(Propyl C<sub>1</sub>), 23(Propyl C<sub>2</sub>), 43 (Propyl C<sub>3</sub>), -6(Si-Me), 50-20(polymer).

### 3.3.3.6 Synthesis of BP-1 nanoparticles (NPA)

500mg of either CPTMS only or 7:1 MTMS:CPTMS coated nanoparticles were added to 11mL of 18% (w/w) solution of 15,000 MW PAA in DI water and .5mL of MeOH was added to prevent foaming. The mixture was sonicated at room temperature for 24hrs. After the reaction the nanoparticles were centrifuged down at 16,000 RPM and washed 2x with 20mL of a 1:1 mixture of MeOH and DI water, and 1x was with DI water only, washes were done by sonication for 30 min followed by centrifugation.  $^{13}\text{C}\{^1\text{H}\}$  SSNMR  $\delta$  8(Propyl C<sub>1</sub>), 23(Propyl C<sub>2</sub>), 43 (Propyl C<sub>3</sub>), -6(Si-Me), 60-20(polymer).

## Chapter 4 Studying the Effects of Surface Properties on the Photophysical Properties of Ruthenium Mono-diimine Complexes Bound to SPCs

### 4.1 Introduction

Surface and materials chemistry is becoming an increasingly studied field as the industrial and research sectors look into creating new materials that are useful in the areas of separations, catalysis, and sensors.<sup>31,35,37-39,111</sup> Knowledge of how binding a molecule to a surface affects different molecular properties is the key to being able to design and control the features needed for individual materials applications.<sup>112</sup>

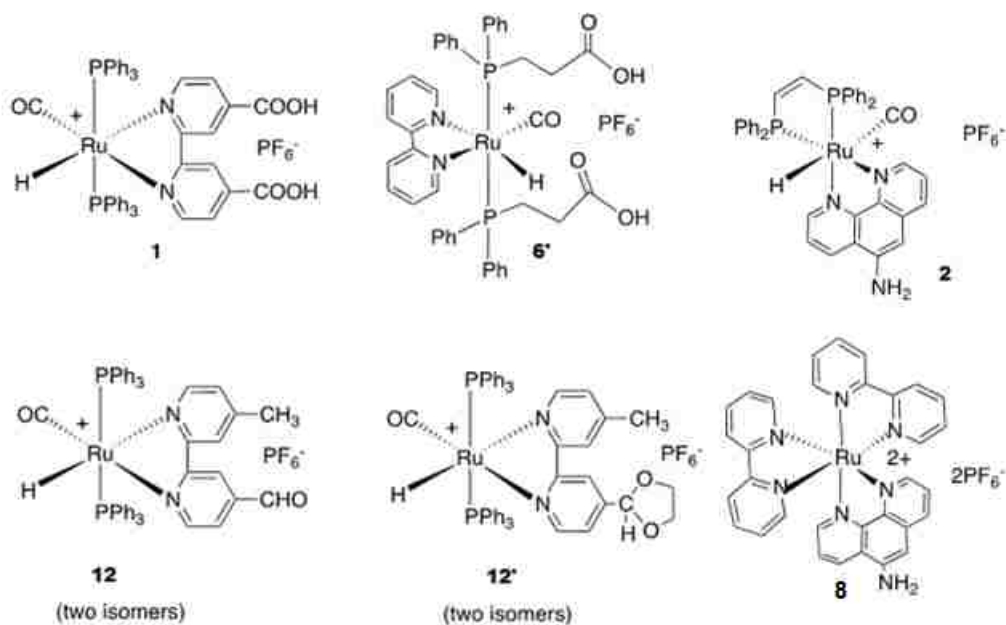
One of the most promising opportunities for surface chemistry in both industry and academic research is the development of heterogeneous catalysts based on currently well-known homogeneous catalysts.<sup>31,35,37-39,112</sup> Any catalyst that can be bound to a surface and can maintain its ability to catalyze a reaction leads to an increase in efficiency as time would no longer have to be spent separating catalyst from the products. Surface immobilization could also result in longer lasting catalysts as the increased stability of a surface could protect the catalyst from degrading as quickly as it would in solution by intermolecular reactions. On the other hand, by placing the catalyst on a surface, access to reactants is hindered and the electron distribution could be affected by the surface in a deleterious way. Understanding what factors affect the surface-bound molecule and its electronic states is important in designing both the surfaces to bind catalysts, as well as designing analogs of these catalysts that can take advantage of certain surface features.

Amorphous silica gels are a common platform for surface chemistry as they are readily available and their surfaces are easily modified through silanization chemistry.<sup>43,44,50,51,56,58,97,98,106,113-118</sup> We have previously reported that modification of silanized

silica gels with a range of polyamines results in materials that selectively bind a wide range of metal ions after modification with metal-selective chelator ligands.<sup>56,98,106</sup>

These silica polyamine composites (SPCs) have also been shown to act as hydrogenation catalysts after adsorption of late transition-metal salts.<sup>31</sup> Related studies have also shown that organometallic complexes covalently bound to a silica particle through a linker can be used as catalysts for various organic reactions.<sup>68</sup> Recently, luminescent Ru complexes have been covalently bound to silicon and silica nanoparticles for potential use as photo-optical devices.<sup>119,120</sup>

### Chart 2 Structures of the Ruthenium Complexes Studied



We report here the immobilization of the series of complexes  $\text{Ru}(\text{CO})(\text{H})(\text{L}_2)(\text{L}'_2)[\text{PF}_6]$  ( $\text{L}_2 = \text{trans-2PPh}_3$ ,  $\text{L}'_2 = \eta^2\text{-4,4'}$ -dicarboxy-bipyridine (**1**);  $\text{L}_2 = \text{trans-2Ph}_2\text{PCH}_2\text{CH}_2\text{COOH}$ ,  $\text{L}'_2 = \text{bipyridine}$  (**6'**);  $\text{L}_2 = \text{Ph}_2\text{PCH}_2\text{CH}_2\text{PPh}_2$  ( $\text{L}'_2 = \eta^2\text{-5-amino-1,10-phenanthroline}$  (**2**);  $\text{L}_2 = \text{trans-2PPh}_3$ ,  $\text{L}'_2 = \eta^2\text{-4-carboxaldehyde-4'-methyl-bipyridine}$  (**12**)) on the SPC surface (Chart 2).

These complexes have been previously been shown to have long excited-state lifetimes and higher quantum yields than the traditional tris-diimine ruthenium complexes such as



[Ru(bpy)<sub>3</sub><sup>2+</sup>].<sup>30</sup> Most recently, we reported that this series of complexes showed significant changes in lifetime and emission wavelength when conjugated to lipids, in organic solvents and when incorporated into lipid vesicles.<sup>3</sup>

The complexes were chosen to provide both different luminophores and anchoring motifs. The luminophores chosen were the diimine ligands, bipyridyl and phenanthroline, and the binding motifs include single-point anchoring and double-point anchoring via the luminophore and through the ancillary phosphine ligands. Immobilization of the complexes on the SPC was accomplished using standard bioconjugation techniques. These same techniques were recently used to bind this series of complexes to both lipids and to cholesterol.<sup>3</sup>

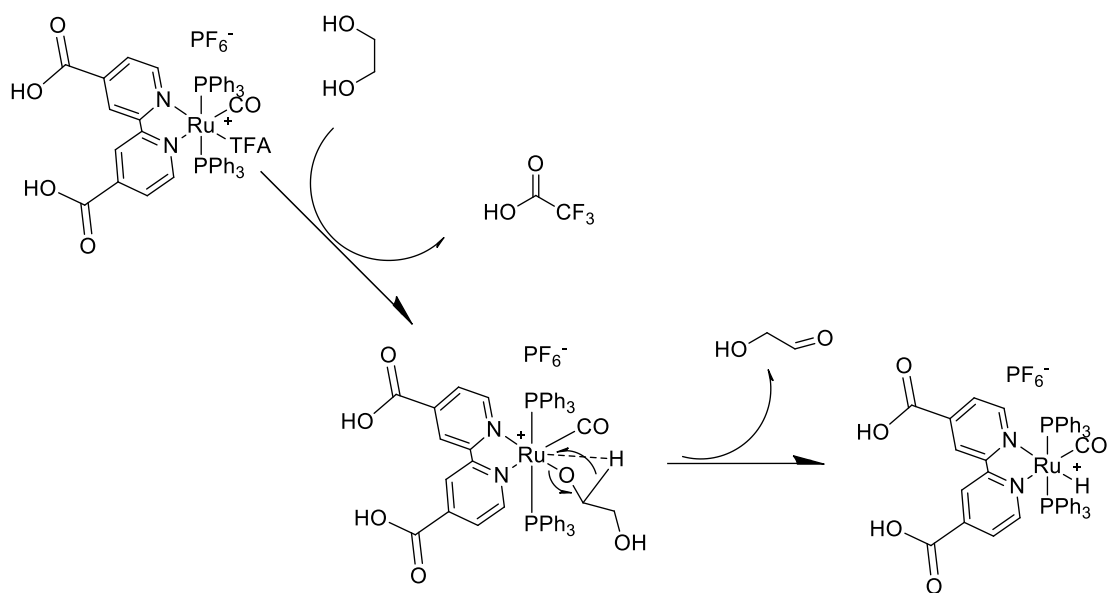
The surfaces used in this study were SPC made from both 300-500 μm and 10-20 nm particles. The polyamines used were high molecular weight (25,000) poly(ethyleneimine) (PEI), which has the designation, WP-1 and poly(allylamine) (PAA) (15,000 MW) which has the designation BP-1 after grafting to the silanized silica surface (Scheme 1). These designations are derived from the commercially produced materials made according to published patents.<sup>43,44,50,51,58</sup> We also report the immobilization of the complexes on a 3-aminopropyl-silica composite to gauge the role of the polyamines in determining the photophysical properties of the SPC-Ru complex systems. In our previous studies we found that the complex [Ru(bpy)<sub>2</sub>(5-amino-1,10-phenanthroline)][PF<sub>6</sub>]<sub>2</sub> (**8**)<sup>67</sup> did not exhibit the anomalous changes in lifetime and emission wavelength observed for the phosphine substituted complexes. We therefore include here the results for immobilization of this complex on the SPC as well.

## 4.2 Results

### 4.2.1 Synthesis

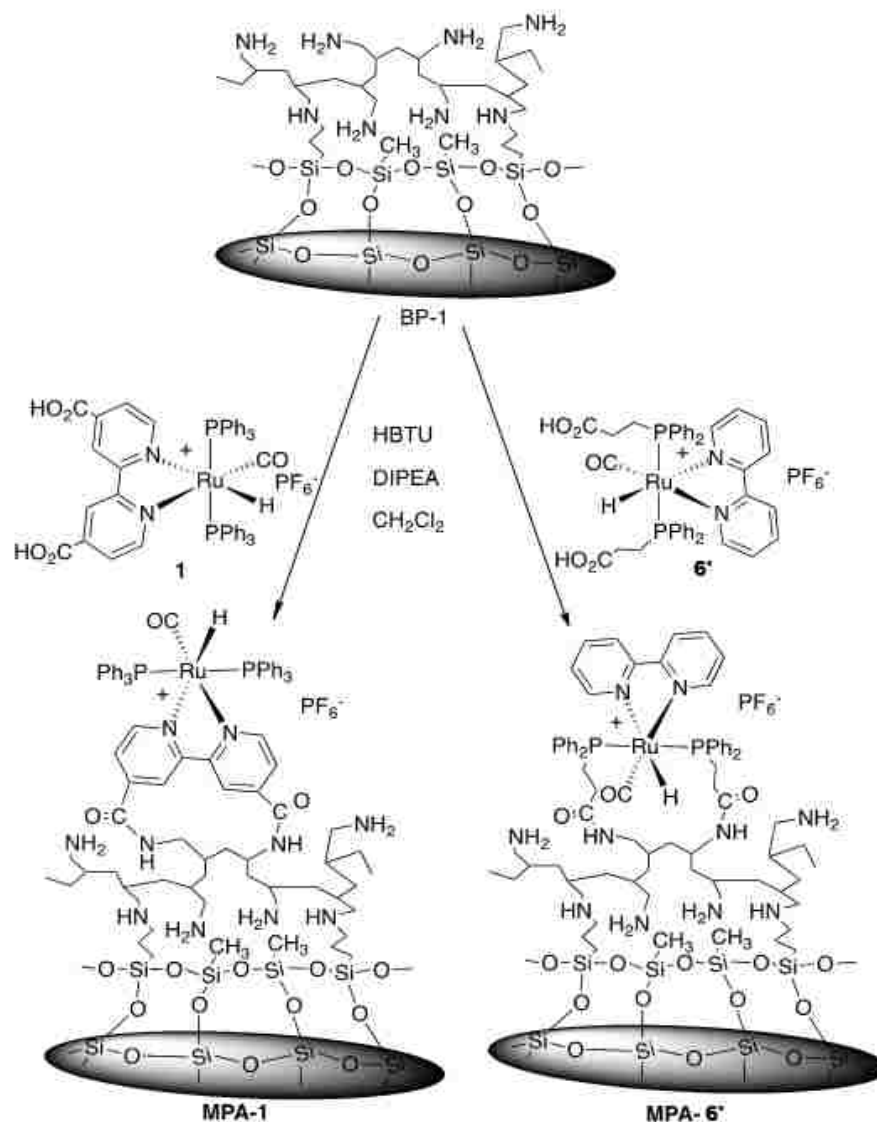
The unbound complexes were synthesized based upon previously published work, in which the same family of complexes were synthesized and characterized with a TFA ligand instead of a hydride.<sup>30</sup> It was found that at higher temperatures (140 °C), over the 72 hour reaction period, that the complexes **1,2,6'**, **12** and **12'** converted to a hydride via formation an alkoxy complex, followed by  $\beta$ -hydride elimination.<sup>3</sup> This approach eliminated the extra step given in the paper<sup>30</sup> for converting the TFA to the hydride (Scheme 6)

**Scheme 6 Hydride Formation for Complex 1**



Using the published procedure<sup>3</sup> for synthesizing complex **12** was complicated by competitive formation of the corresponding acetal, **12'** and by the fact that the compound and the acetal both exist as two isomers (see Chart 2 and Scheme B1 in Appendix B). The compounds **12** and **12'** could not be separated by chromatography on alumina. The presence of the acetal is confirmed by the presence of two singlets at  $\delta$  4.73 and 4.86 assignable to the CH proton in the two isomers that together integrate 1:2:2 with two multiplets at  $\delta$  3.45 and 3.70 (see Figure B1a).

### Scheme 7 Coupling of 1 and 6' to BP-1



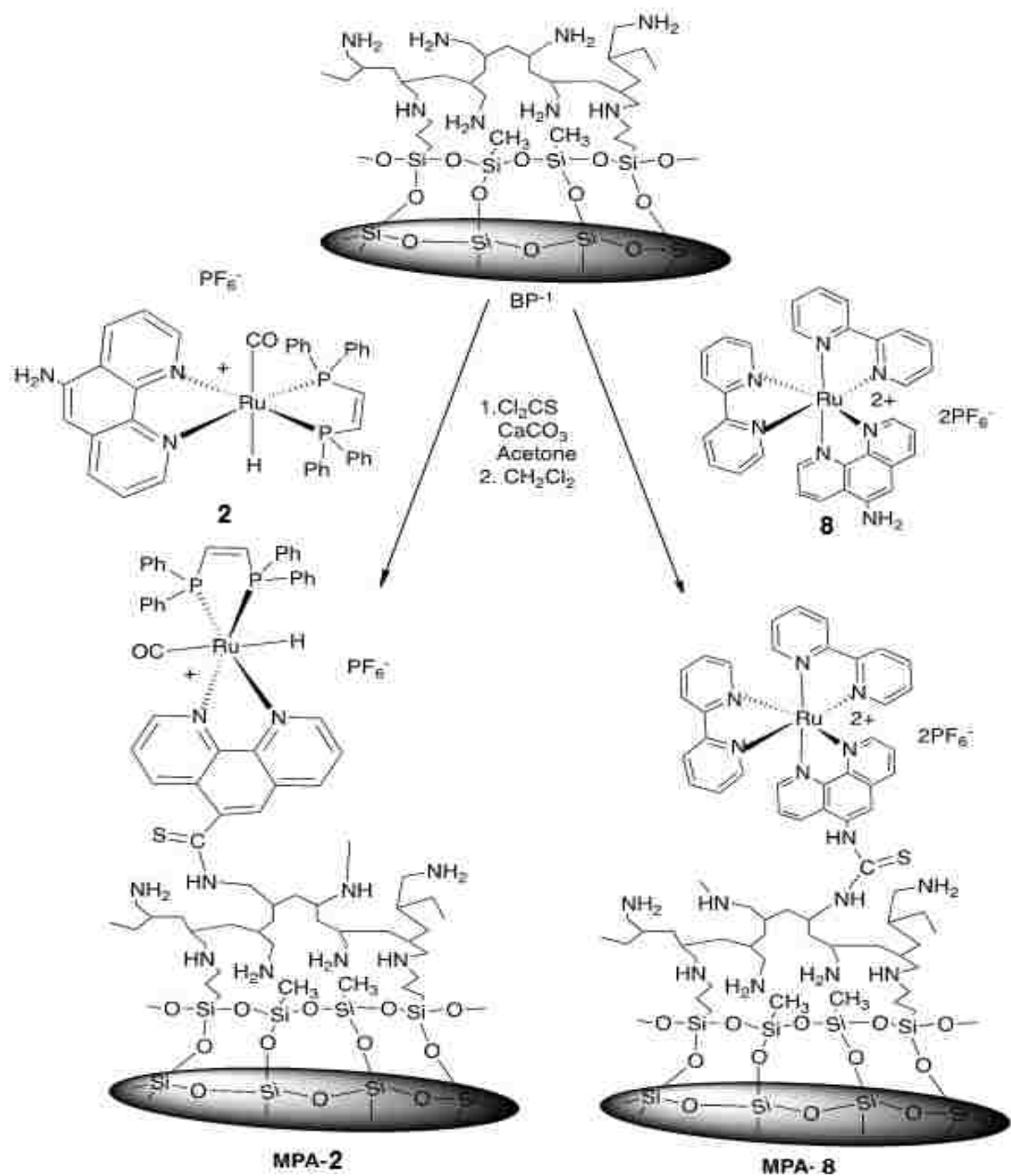
HBTU = O-(Benzotriazol-1-yl)-N,N,N',N'-tetramethyluronium hexafluorophosphate  
 DIPEA = di-Isopropylethyl amine

The aldehyde resonance appears as a broad singlet at  $\delta$  8.65 that is assigned to an overlap of the two-aldehyde isomers see (Figure B1b). Integration of the aldehyde resonance relative to the two CH resonances of the acetal gives a ratio of approximately 2:3. The hydride resonances appear as a broad, equally spaced, asymmetric sextuplet at  $\delta$  -11.18 to -11.42 that we assign to an overlap of the expected 4 triplets of the two sets of two isomers (Figure B1b). The bipyridyl

resonances also appear, as overlapping doublets and scaling the hydride to a value of one proton gives the correct integration for the overlapping bipyridyl and phenyl phosphine resonances, consistent with the presence of the two sets of two isomers (Figure B1b). The  $^{13}\text{C}$  NMR shows resonances entirely consistent with these assignments and the presence of the isomers (Figure B2). The quaternary phosphine carbon resonance in the  $^{13}\text{C}$  NMR appears as a triplet owing to the  $^{31}\text{P}$ - $^{31}\text{P}$  *trans*-virtual coupling and confirms the presence of two *trans* phosphines. The  $^{31}\text{P}$  NMR however, shows only one overlapping resonance for the phosphines at  $\delta$  46 along with expected multiplet for the  $\text{PF}_6^-$  at  $\delta$  -140, which integrates 1:2 with the phosphine. A complete assignment of the NMR data along with relative integrated intensities for the various isomers is given in the experimental section. The formation of the acetal can be avoided by doing the reaction in toluene, but subsequent attempts to convert to the hydride in refluxing ethanol result in hemiacetal formation. On reaction with the SPC surface we see the formation of the imine based on the spectroscopic data by reaction of the aldehyde or the aldehyde and the acetal with the primary amine groups on BP-1 (*vide infra*).

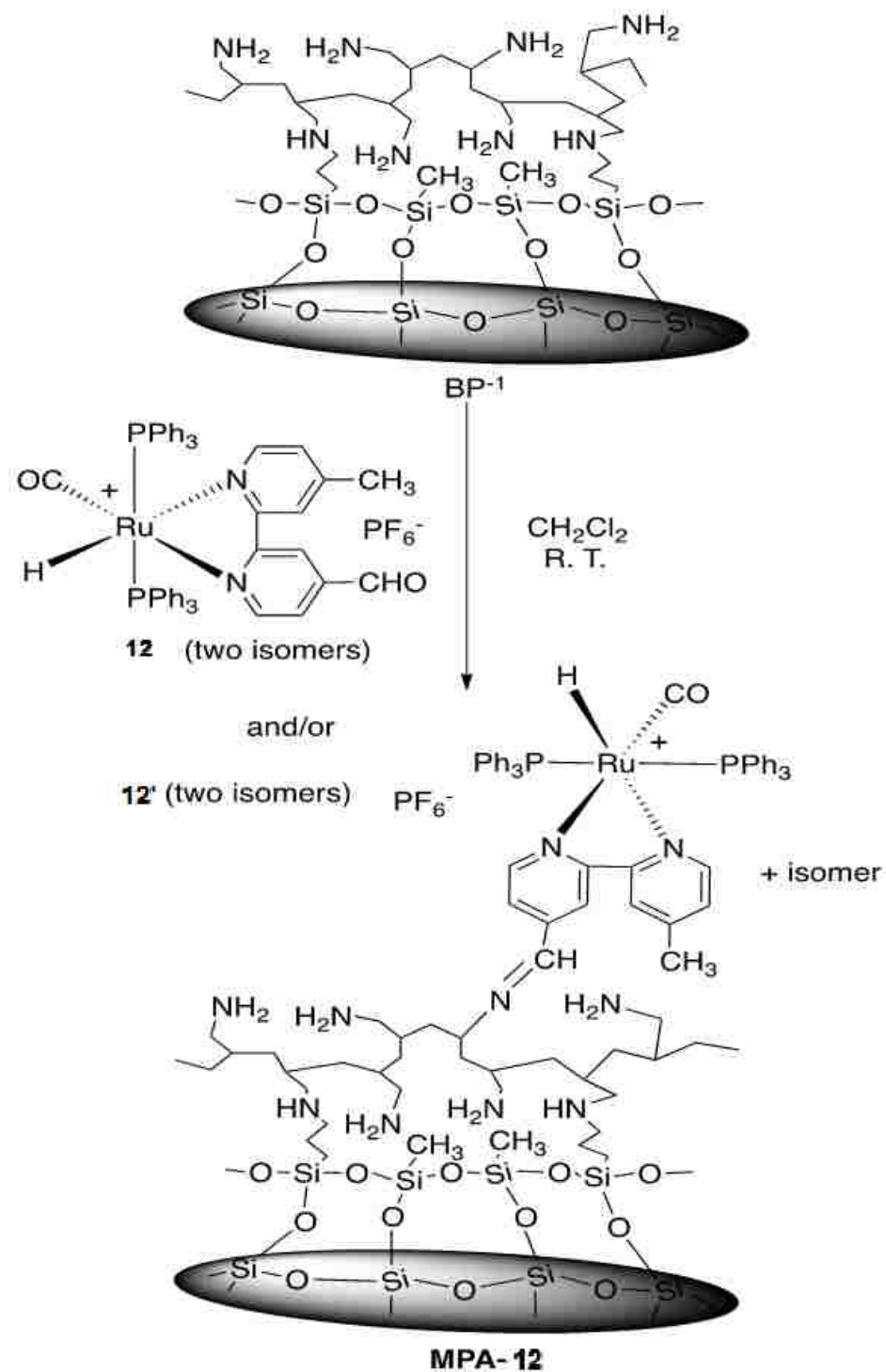
The complex  $[\text{Ru}(\text{bpy})_2(5\text{-amino-1,10-phen})][\text{PF}_6]$  (**8**, Chart 1) and its photophysical properties have been previously reported.<sup>67</sup> We report here the immobilization of this complex on composite surfaces with the goal of determining the role of the ancillary ligands on the photophysical properties for the surface-bound complexes.

The three synthetic routes used to achieve binding of the ruthenium complexes onto the surface of the SPC particles are shown in Schemes 7-9. First, for the carboxylic acid linkers a peptide coupling reagent, HBTU, was used to facilitate a one-pot reaction that created an amide linkage between the surface and the complex.<sup>1,2</sup> Second, for the amine-to-amine coupling the



**Scheme 8 Coupling of 2 and 8 to BP-1**

complex was converted to an isothiocyanate derivative. This allowed reaction with the amine surface to form a covalent linkage via a stable thiourea bond.<sup>4</sup> Third, the carbaldehyde coupling



**Scheme 9 Coupling of 12 and 12' to BP-1**

occurred via direct reaction of the 4-methyl-2,2'-bipyridine-4'-carbaldehyde with the amine surface. This reaction was carried out in chloroform at room temperature.

#### 4.2.2 IR, NMR and Solid-State NMR (SS-NMR)

The complexes in solution were previously characterized via IR and NMR and these data are reviewed here for comparison with the surface-bound species.<sup>3</sup> All the complexes, except the trisdiimine complex **8**, showed a strong metal CO stretch between  $\sim 1940\text{-}2000\text{ cm}^{-1}$ , as well as the strong diimine ring stretches between  $\sim 800\text{-}840\text{ cm}^{-1}$ .  $^1\text{H}$  NMR showed the presence of a hydride, split as a triplet, at  $\delta -11.1$  for the complexes **1** and **6'**, and  $\delta -6.9$  ppm for complex **2**, while the  $^{13}\text{C}$  NMR showed CO peaks between  $\delta 200\text{-}205$ , indicative of a metal bound CO.  $^{31}\text{P}$  NMR showed a single doublet in the  $\delta 40\text{-}50$  range and the  $\text{PF}_6^-$  septuplet at  $\delta -145$ , with a relative intensity of 2:1 ratio.

All the composites containing the immobilized complexes were characterized by IR and  $^{13}\text{C}$  and  $^{31}\text{P}$  SS-NMR that confirmed the presence of the complex on the surface, except **MPA-8**, which was characterized only by IR and  $^{13}\text{C}$  SS-NMR. In the IR all the composites, except **MPA-8**, showed a weak CO stretching peak in the carbonyl,  $1940\text{-}2000\text{ cm}^{-1}$ , which corresponds to the same stretch as the complex in solution (Figure 18). In the case of **1** the band at  $1729\text{ cm}^{-1}$  is due to the carboxyl groups in **1** and on reaction with the surface the carboxyl group is converted to an amide that shows a strong broad band at  $1637\text{ cm}^{-1}$  in **MPA-1**

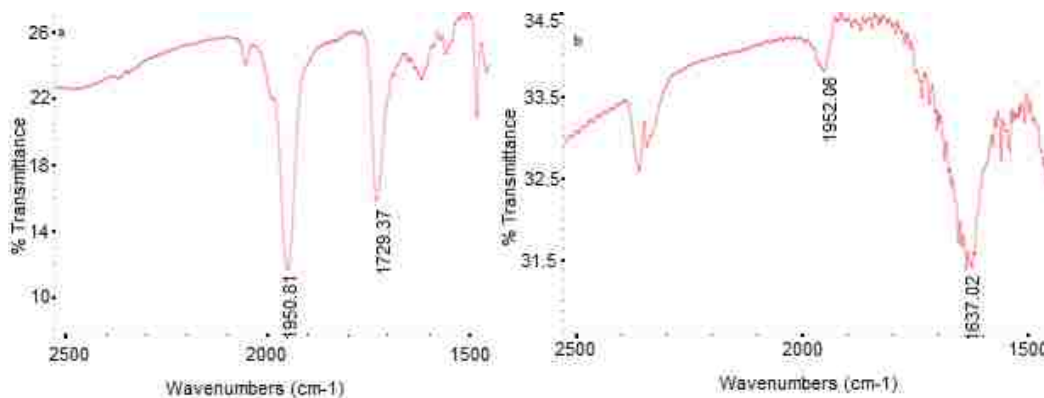


Figure 18 Comparison of the Metal-CO Stretching frequency between a) Compound **1** as a KBr Pellet and (b) analog **MPA-1** on the surface

Each compound also shows the very strong band at  $\sim 840\text{ cm}^{-1}$ , indicative of the diimine rings, which is consistent with the intact complex being on the surface. **MPA-6'**, with its much longer tether, shows only one such band at  $1640\text{ cm}^{-1}$ . **MPA-1**, **NPA-1** and **NPA-6'** also show weak carboxylate ion stretches at  $1530\text{ cm}^{-1}$  and  $1399\text{ cm}^{-1}$ . Surprisingly, **MPE-1** also shows only one amide CO stretch in this region at  $1672\text{ cm}^{-1}$  where free carboxylate might be expected due to the lower number for primary amines (*vide infra*). Compounds **MPA-2**, **NPA-2** and **MPA-9**, show the stretches for the C=S bond at  $1399\text{ cm}^{-1}$  and a C=N bond can be seen and  $1630\text{ cm}^{-1}$  imine bond in **MPA-12**.  $^{13}\text{C}$  SS-NMR resonances at  $\delta$  100-150 also confirmed the presence of aromatics on the surface. However, due to the broadness of the peaks the difference between the diimine carbons and the phenyl groups on the phosphines are indistinguishable.  $^{13}\text{C}$ -NMR of  $^{13}\text{CO}$  enriched composites show the presence of the CO ligand at  $\delta$  200-210 in the composites tested (**MPA-1-MPA-2**).  $^{31}\text{P}$  SS-NMR of the complexes on the composites shows a single peak in a similar chemical shift range to that observed in solution. The presence of multiple spinning side bands suggests a high degree of anisotropy and that the complexes are in a fairly rigid environment (Figure 19). A complete set of SS  $^{13}\text{C}$  NMR spectra for the complexes on the composites is provided in the Appendix B.



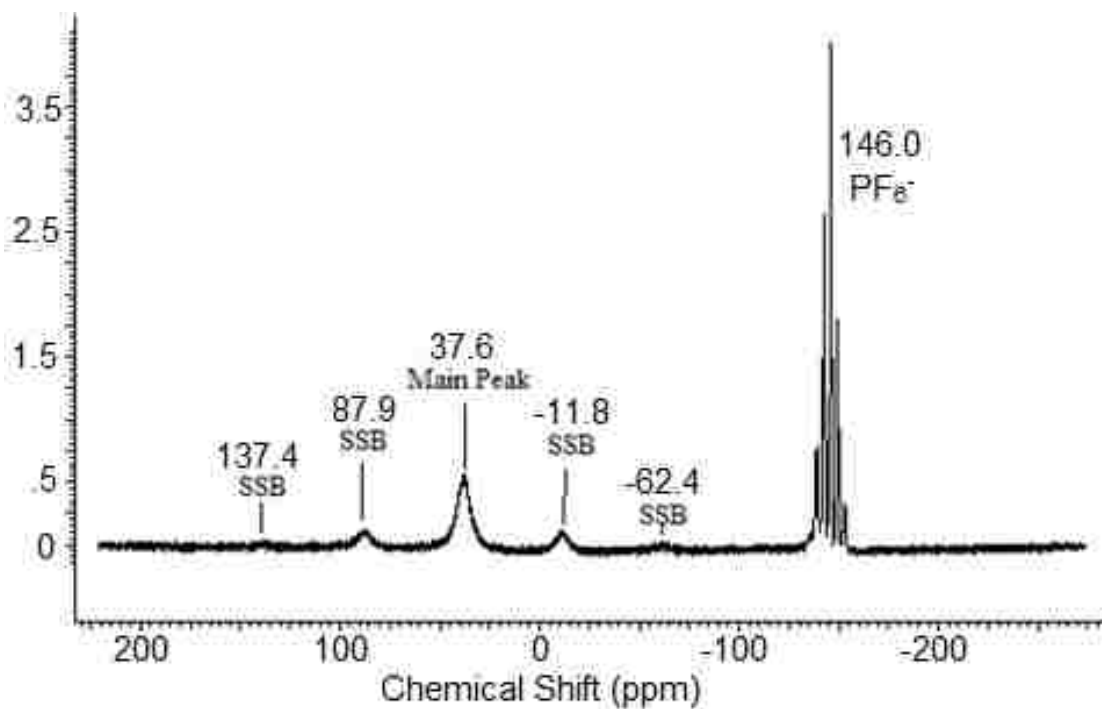
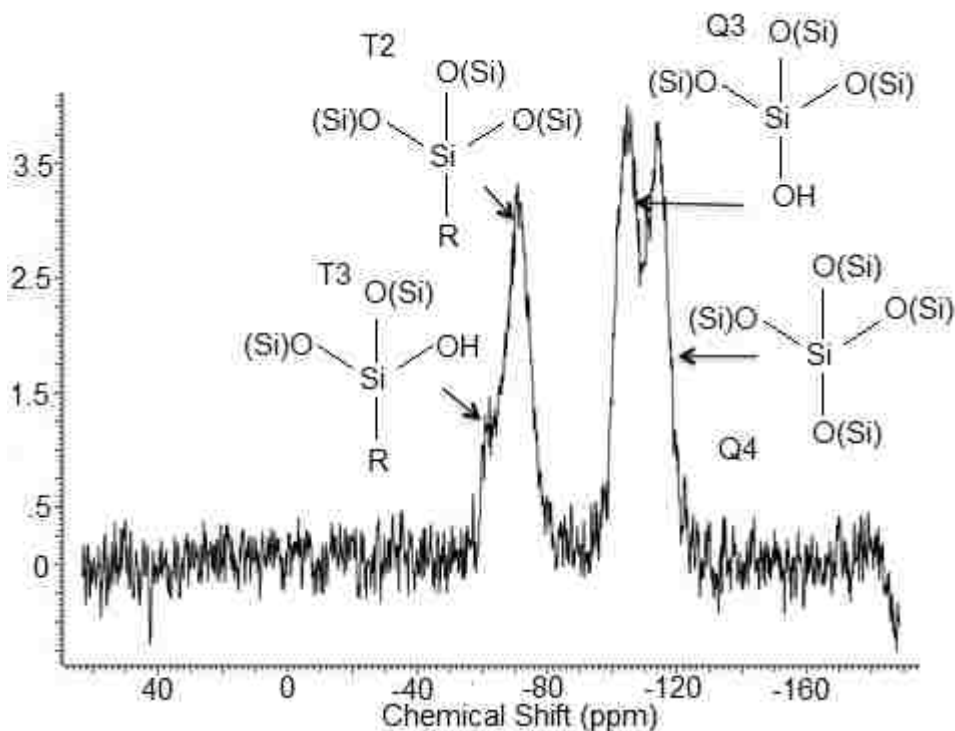


Figure 19  $^{31}\text{P}$  SSNMR of MPA-2 at 202.5 MHz

$^{29}\text{Si}$  SS-NMR was performed primarily on the aminopropyl analogs for the micro- and nanoparticles and for the nanoparticle analogs of BP-1 and WP-1.  $^{29}\text{Si}$  SS-NMR of BP-1 and WP-1 micro particles have been previously reported.<sup>56,111</sup> The aminopropyl micro particles show a high ratio of T to Q peaks on the surface after reaction with aminopropyltrimethoxy silane. The  $T_n$  peaks indicate a silica bound to one alkyl and  $n$  Si-O-Si bonds, while the Q peaks represent bulk silica ( $Q_4$ ) and surface silica having one ( $Q_3$ ) and two ( $Q_2$ ) surface hydroxyl groups respectively (Figure 20). The assignments for the different species vary only within 1-2 ppm for different modified silicas and those reported here are



**Figure 20**  $^{29}\text{Si}$  SSNMR showing the resonances peak difference between bulk and surface silanes

based on prior work.<sup>98,111</sup> In the case of the aminopropyl composites the ratio of T/Q decreases after reaction with the complexes, indicating that the surface aminopropyl groups are being lost due to hydrolysis during the reaction. The hydrolysis of the groups is much greater for the nanoparticles' as shown by the complete disappearance of the T peaks in the  $^{29}\text{Si}$  SS NMR and loss of the propyl chain carbons in the  $^{13}\text{C}$  SS-NMR (Figure 21). We suggest that this is due, in part, to the nanoparticles' spherical shape and small size, which results in a large curvature allowing easier access of nucleophiles (the isothiocyanate in the case of complex **2**) to the surface Si-O bonds, thereby enhancing hydrolysis. The relatively flat sections of the much larger microparticles allow the aminopropyl groups to pack more tightly and provide a more protective layer.

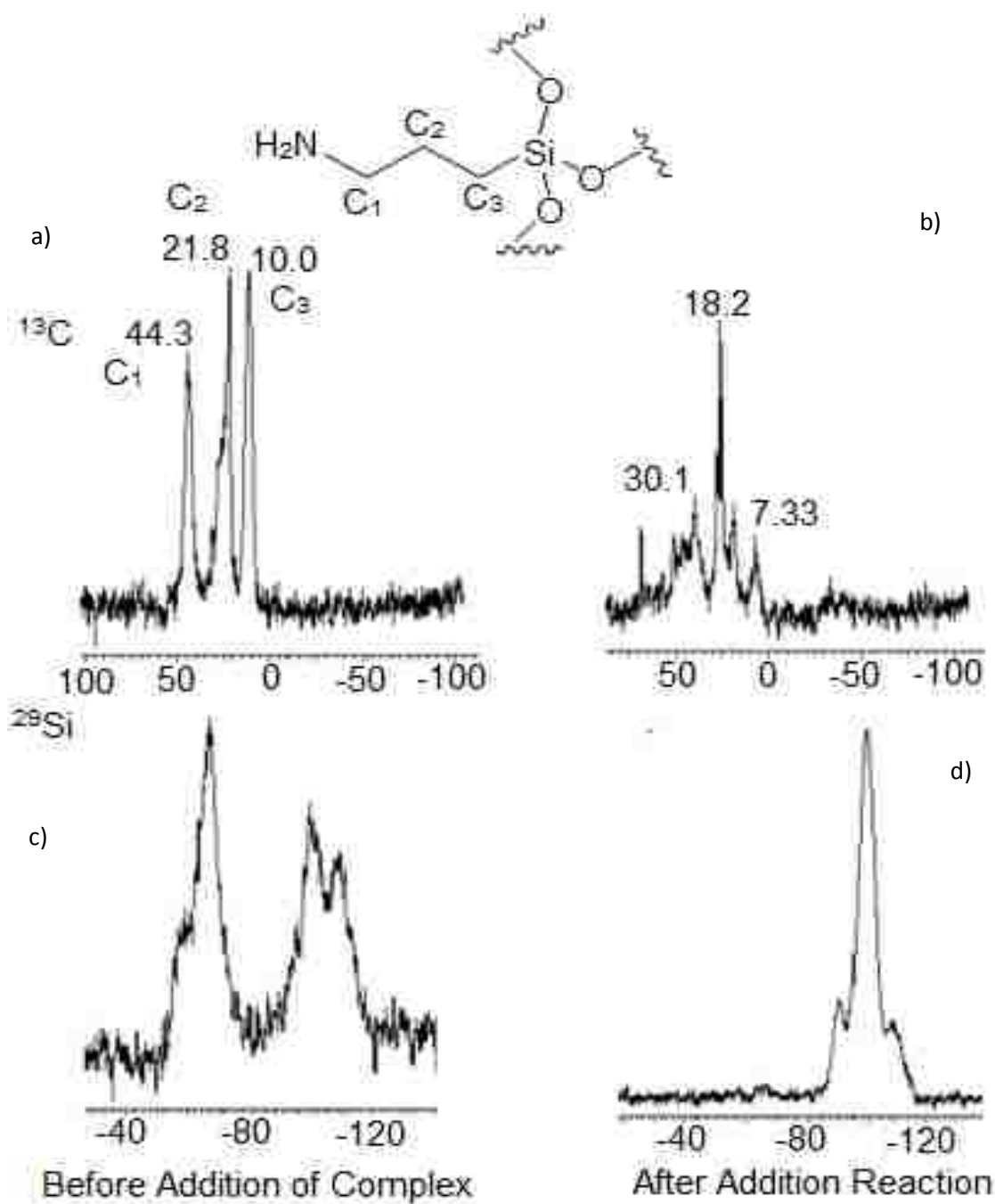


Figure 21 a) <sup>13</sup>C SSNMR of NAP prior to reaction with complex 3. b) <sup>13</sup>C SSNMR of NAP after reaction with complex 2 showing loss of the aminopropyl groups. c) <sup>29</sup>Si SSNMR of NAP prior to reaction with complex 2. d) <sup>29</sup>Si SSNMR after reaction with complex 2 showing loss of Tn site

### 4.2.3 Loading

The loading of the complexes on the SPC was evaluated by atomic absorption analysis of the Ru content after complete digestion of the samples. The microparticles **MPA-1**, **MPA-6'** and **MPA-2** load at 0.013 mmol/g, 0.039 mmol/g, and 0.044 mmol/g respectively, while the nanoparticle analogs, **NPA-1**, **NPA-6'** and **NPA-2** load at 0.015, 0.048, 0.023 mmol/g respectively. The loadings are similar except in case the amino-phenanthroline analogs, where loading is significantly higher for the microparticles (Figure 22). These loadings are in the range of 1-3% based on the mmol of N per gram of BP-1 (1.6 mmol/g) and do not compare favorably with the ligand loadings of ligands such as chloroacetate, where loadings are in the range 40-70 % of the available amines on similar composites.<sup>48</sup> This is not too surprising in light of the greater bulk of the complexes **1,2** and **6'** and the lower efficiency of the linker chemistry compared with simple nucleophilic displacement chemistry used with chloroacetate.

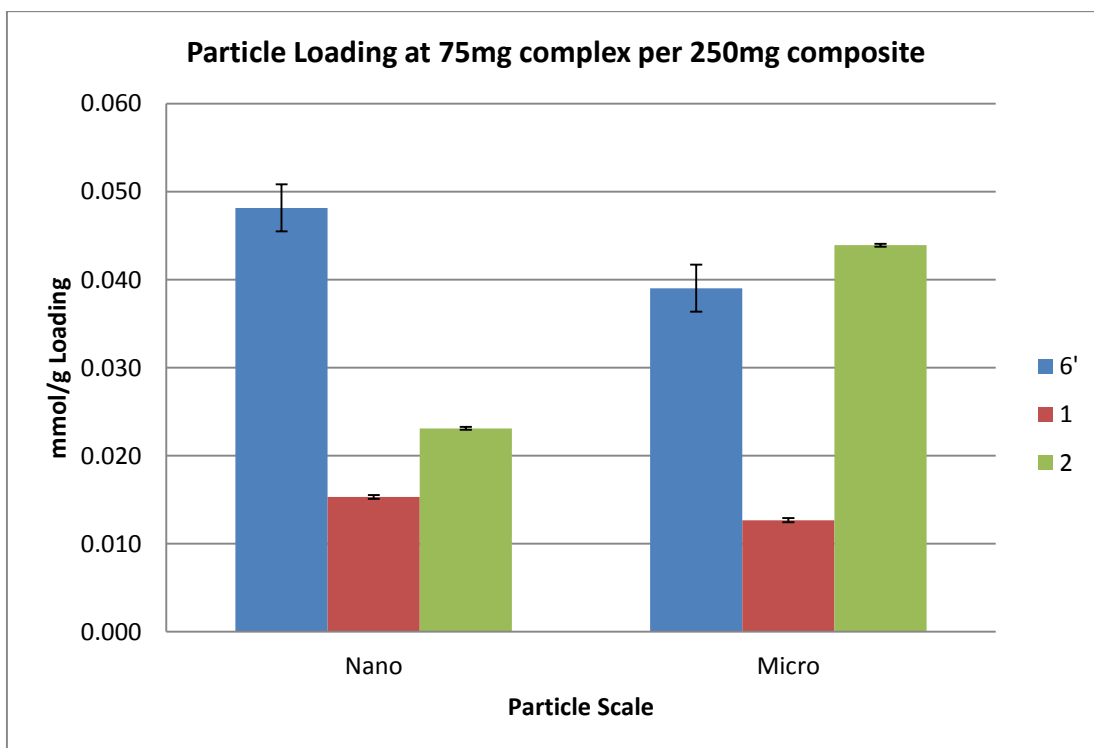


Figure 22 Bar Graph showing the loading levels of complex 1,2 and 6' on Micro and Nano SPCs

The loading studies also revealed that the complexes coupled to the surface with HBTU reach a saturation point after which no further loading is realized. For the nanoparticles, once the ratio of complex to composite reaches 75 mg per 250 grams of composite, loading actually decreases. This is likely due to the higher base concentration required for the coupling reaction. This causes increased degradation of the surface in the case of the more sensitive nanocomposites (Figure 23).

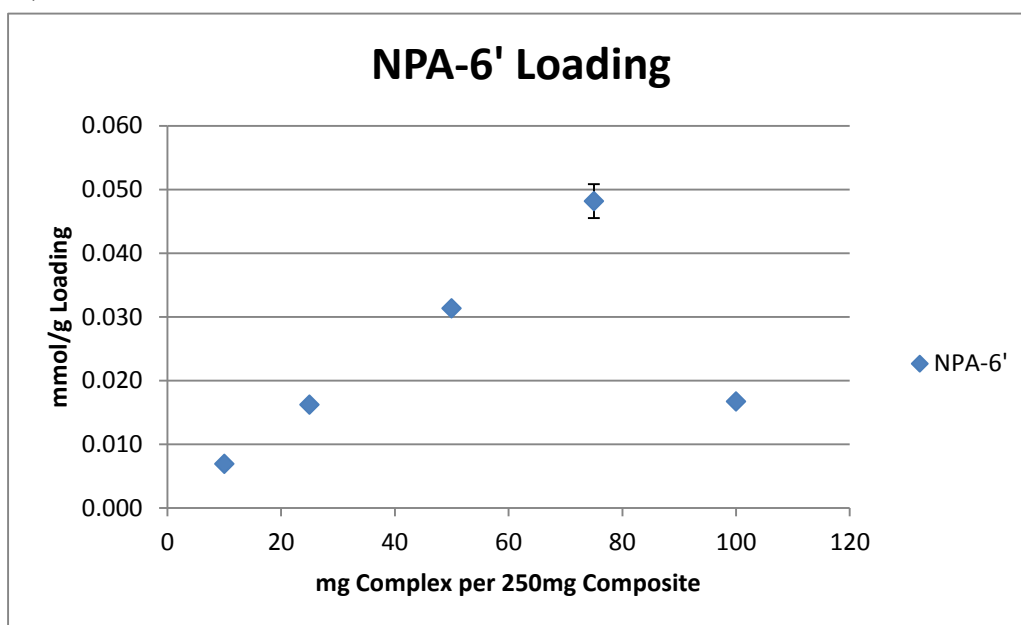


Figure 23 Graph showing the loading levels of complex 6' on reaction with NPA

#### 4.2.4 Luminescence Studies

The emission of the complexes was measured by irradiation at 470 nm using the configuration described in the experimental section. This wavelength targets the metal-to-ligand charge-transfer band (MLCT) usually found between 430-470 nm.<sup>3,29</sup> The MLCT bands for the complexes reported here in solution are given in Table 9.

**Table 9. Comparison of Emission Maxima for Complexes in Solution and Complexes on BP-1**

<b>Compound</b>	<b>Emission Maximum(nm) in ETOH Solution</b>	<b>Emission Maximum (nm) on BP-1</b>
<b>MPA-1</b>	647	634
<b>MPA-6'</b>	600	600
<b>MPA-2</b>	590	590
<b>MPA-12</b>	612	604
<b>MPA-8</b>	635	612

Attempts to measure the absorption spectra of the particles using diffuse reflectance techniques were unsuccessful. However, **MPA-1**, was sent to On-Line Instrument Systems (OLIS) and using their CLARiTY absorbance spectrometer they measured the absorbance spectra of **1** on the BP-1 surface. A comparison of the emissions from the complexes observed in solution and on the composite surface is shown in Table 9. Both show absorption maxima in the same MLCT region. The surface-bound **MPA-1**, however, shows two partially resolved bands while **1** in solution shows one maximum. This could be due to vibronic structure, electronic bands becoming apparent due to environment-dependent shifts and band narrowing, or the presence of several differently bound species; it has been observed in solution for some of these complexes (Figure 24).<sup>3,18,29,30,94,121</sup>

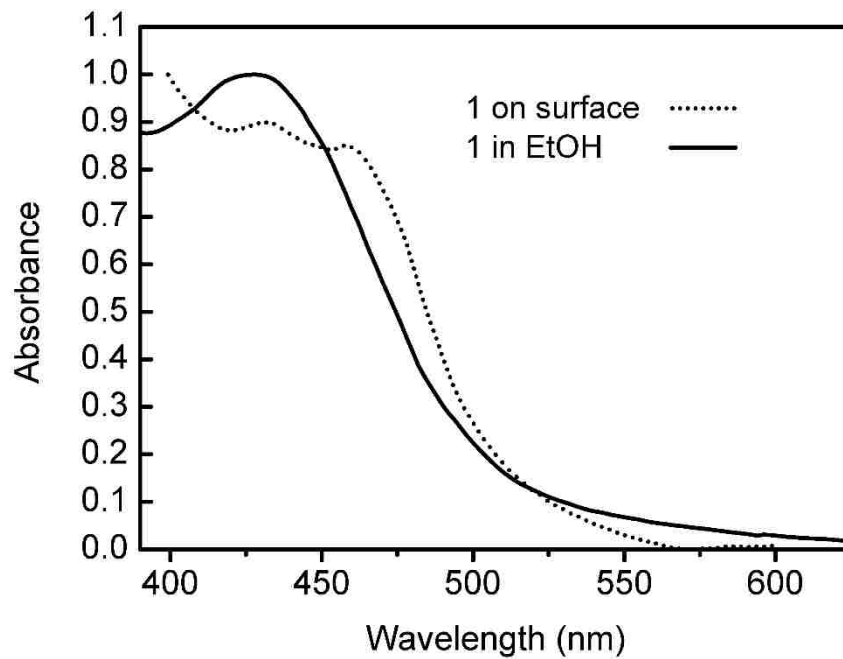


Figure 24 Absorption spectra of complex 1 in solution (----) and the MPA-1 analog (-----).

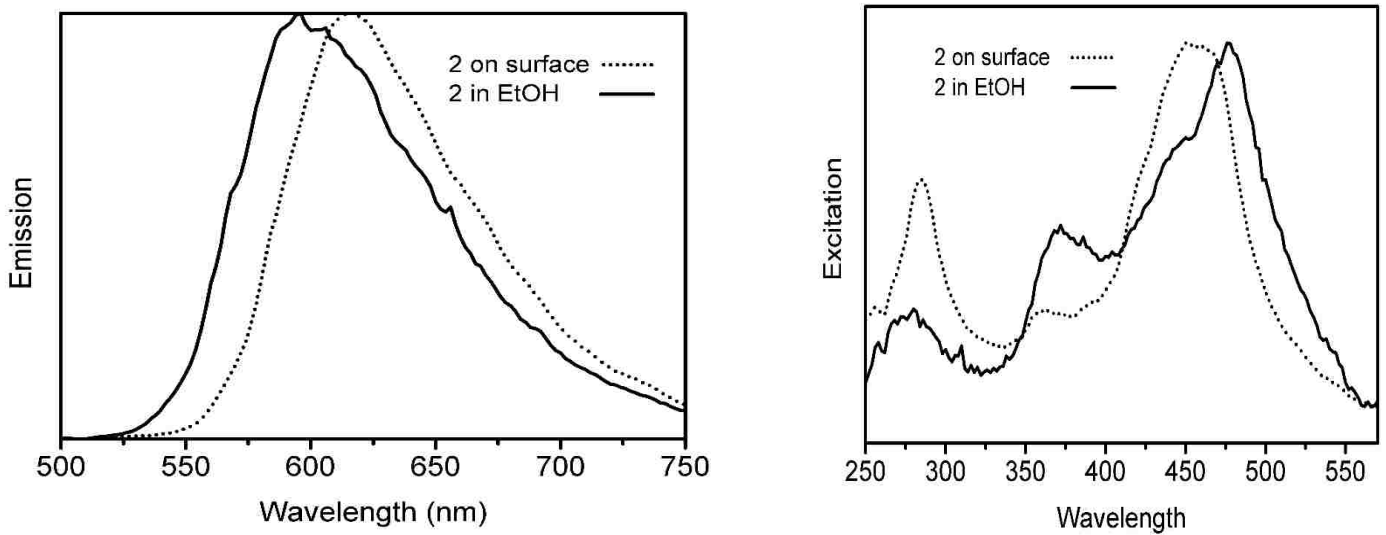


Figure 25 Top: peak normalized emission spectra of complex 6' in solution (----) and on the composite BP-1 (MPA-6') (-----). Bottom: Excitation spectra of complex 6' in solution (-----) and on the composite BP-1 (MPA-6') (-----).

Complexes **1**, **12** and **8** showed small but significant changes in their emission wavelength on binding to the BP-1 surface while **6'** and **2** showed emission wavelengths identical to that observed in the solution (Table 9). The shape of the emission curves is the same in both cases and this is illustrated for **6'** and **MPA-6'** in Figure 25 (bottom left). From the excitation spectra, it is observed that the major contribution to the excited state comes from the MLCT absorption band, as expected, but in the case of complexes **1**, **2**, **6'**, and **12** there is an additional contribution from absorption bands at 280 and 350 nm that can be assigned to the intraligand transitions on the diimine and phosphine ligands both in solution and on the surface (Figure 16b). Interestingly, for the surface-bound complex **6'** the contribution from the diimine ligand noticeably increases while that of the band at 350 nm decreases (Figure 16, bottom right). These changes report on the relative efficiencies of pathways populating the emissive state from the optically populated ones. From Fig. 25 bottom, it follows that population of the emitting  $^3\text{MLCT}$  from the intraligand state excited around 280 nm is more efficient than in solution. In the case of **5**, which does not have phosphine ligands the excitation spectra show only contributions from transitions around 300 nm.<sup>3</sup> The broadening of the excitation spectrum on the surface relative to solution is indicative of a very heterogeneous environment (Figure 25, bottom right).

The emission wavelengths for the complexes **1**, **2**, **6'**, and **12** coupled to the silica nanoparticles (NPA-1, NPA-2, NPA-6' and NPA-12), were identical to those on the microparticles (MPA-1, MPA-2, MPA-6' and MPA-12) and their excitation spectra are similar. In the case of the complexes **1**, **2** and **12** coupled to the branched polymer composite WP-1 (MPE-1, MPE-2 and MPE-12) the emission wavelength of MPE-1 shifts to 616 nm from 634 nm in MPA-1, while the other two complexes had the same emission maximum as MPA-2 and MPA-12. Complexes **6'** and **2** were also coupled to aminopropyl-modified silica microparticles.



Complex **6'** on this surface (**MAP-6'**) showed a shift to 616 nm from 600 nm, also observed for **MPA-6'**, while complex **MAP-3** had the same emission as **MPA-3**. These results indicates that, in general, the surface environment has only a slight effect on the emission wavelength relative to the complex in solution, which suggests that the transition energies of the metal and the ligands are relatively insensitive to surface immobilization

#### 4.2.5 Lifetime Measurements

A comparison of the excited-state lifetimes of the complexes **1, 2, 6', 8** and **12** in solution and on the composite BP-1 is shown in Table 2. It can be seen that, with the exception of **5**, all the complexes show increases in average lifetime of four to six-fold that in solution (Table 10).

**Table 10. Comparison of Lifetimes for Complexes in Solution and Complexes on BP-1**  
**Microparticles**

Compound	Lifetime (ns) in ETOH Solution	Lifetime on BP-1 (PAA) <sup>a</sup> (μs)	Lower and Upper 95% Confidence Limits on BP-1 (μs)
<b>MPA-1</b>	720	3.45 (4.8x Increase)	3.29/3.63
<b>MPA-6'</b>	236	1.28 (5.4x Increase)	1.26/1.30
<b>MPA-2</b>	240	0.93 (3.9x Increase)	0.85/1.01
<b>MPA-12</b>	225	1.43 μs (6.3x Increase)	1.30/1.57
<b>MPA-8</b>	220	0.270 (1.2xincrease)	0.250/0.330

<sup>a</sup> Increases are calculated as ratio of (composite lifetime/solution lifetime)

The observed large increases in lifetime likely arise from several factors. First, limiting the accessible vibrational modes will reduce internal conversion and lengthen lifetime. Second, lifetime lengthening upon surface binding can also be due to lack of solvation, because coupling of molecular and solvent vibrational modes provides an effective deactivation pathway. This is a well-known effect, observable also when transition-metal chromophores are placed in

constrained supramolecular media. The magnitude of the increase is large and potentially useful in electron transfer chemistry.

In comparison with the other complexes, **8** showed only a slight increase in lifetime. This could be due to a number of factors. First, the molecular volume of **8** is much less than the other complexes, which would lead to less steric interaction with the surface and relatively greater mobility (Figure 26). Increased solvent collisions or easier population of deactivating dd states would result in a dynamic quenching and faster decay. Second, the likely electron acceptor ligands in **8** are the bipyridyl ligands and the absence of the phosphines could result in less electron delocalization in the excited-state, making the complex less sensitive to changes in accessible modes of relaxation. These interpretations, however, must be considered only tentative as the factors contributing to excited-state lifetimes are many and complex.<sup>3,29</sup>

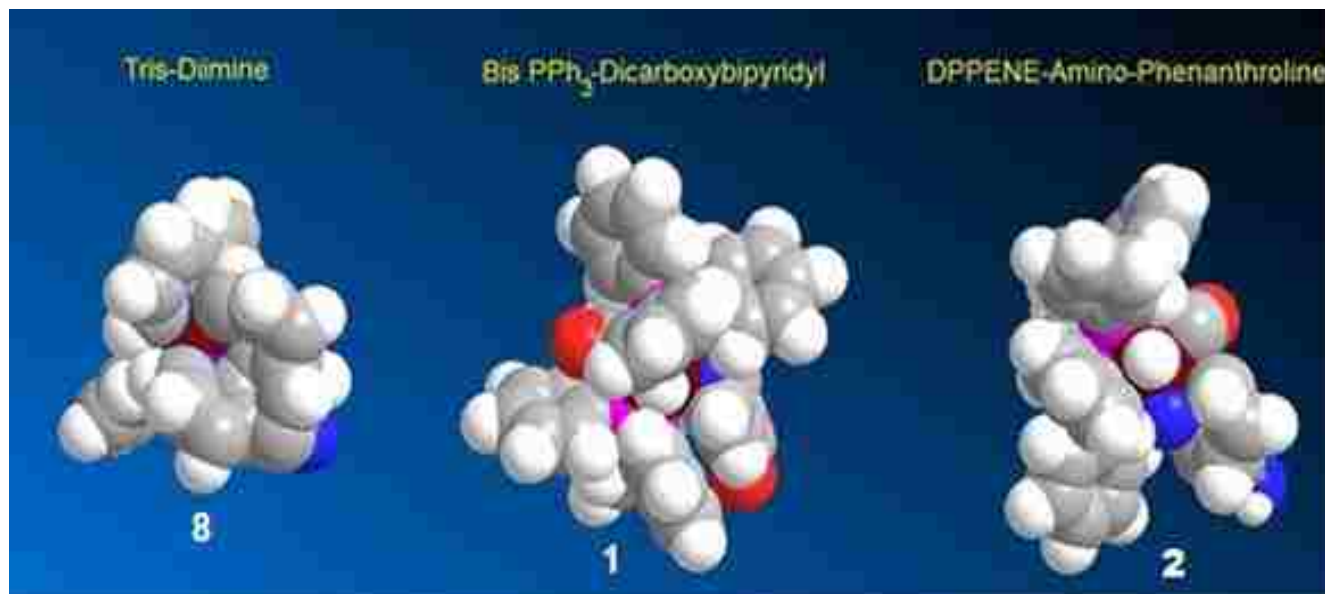
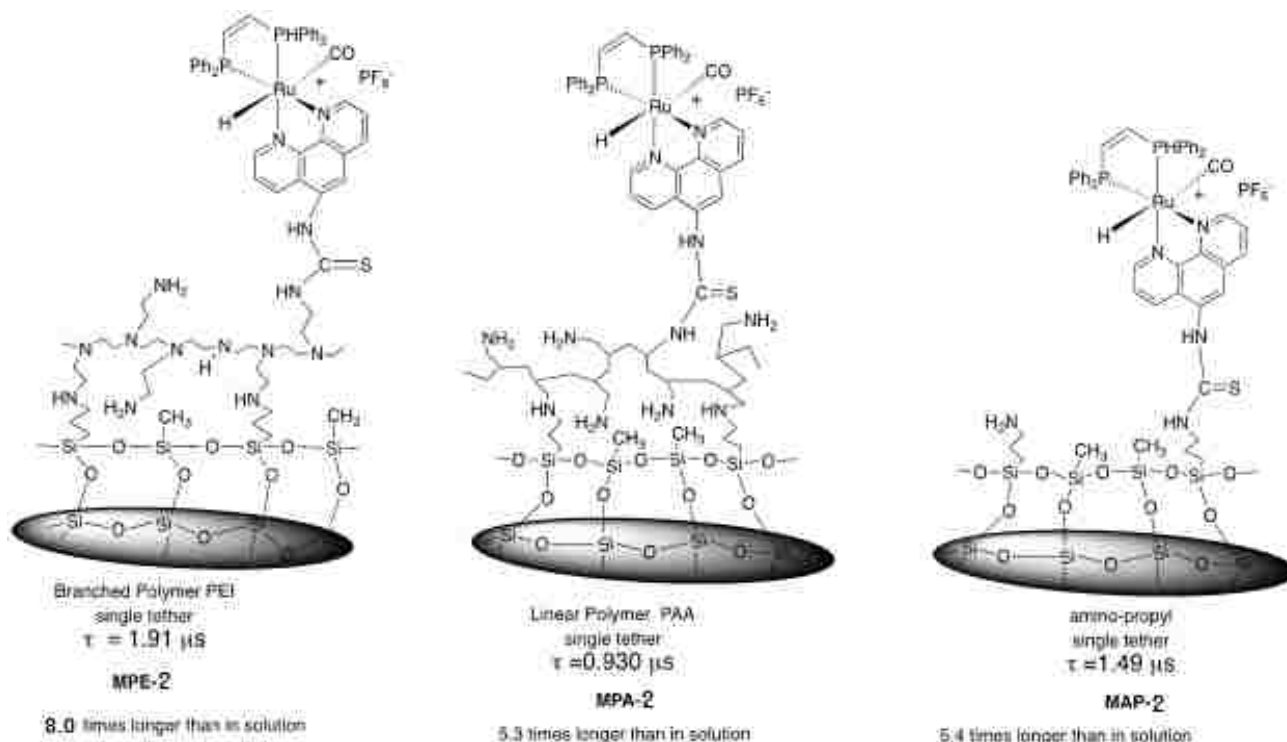


Figure 26 Close packed sphere models of Complexes 9, 1 and 2

To gain a better understanding of how the nature of the surface influences the excited state lifetime of the immobilized complexes, we have compared the lifetime of the single-tethered complex **2** on BP-1, WP-1 and amino-propyl micro-particles. BP-1 is made with the linear PAA and has pendent primary amine groups. WP-1 is a branched polymer consisting of approximately equal amounts of primary, secondary and tertiary amine groups with the secondary and tertiary amines in the backbone of the polymer, a much more rigid network, overall; the amino propyl group probably provides the most flexible environment for the immobilized complex. On the PEI-coated microparticles the single-anchor complex **2** showed an increase in average lifetime, on the order of 8.0x compared with that of the complex in solution. The aminopropyl and PAA-modified surfaces showed smaller increases in average lifetime, indicating that local mobility is a determining factor for the observed increases in lifetime (Scheme 10). Complex **2** bound to the most flexible surface, aminopropyl, showed a significantly larger increase relative to the same complex on the linear polymer PAA. This could be the result of direct interactions of the complex with the silica surface, a phenomenon noted with other aminopropyl-modified silicas.<sup>122</sup>



### Scheme 10 Lifetimes of Complex 2 on different surfaces

We then examined the lifetime of two other complexes, **1** and **12** on the more rigid surface of WP-1. These complexes showed respectively, only about half to three-fold increases in average lifetime, less than that observed on BP-1 (Table 11).

**Table 11. Comparison of Lifetimes for Complexes on Different Micro-particle Surfaces**

Compound	Lifetime on WP-1 (PEI) <sup>a</sup> ( $\mu\text{s}$ ) MPE-1, MPE-2, MPE-12	Lower and Upper 95% Confidence Limits ( $\mu\text{s}$ )	Lifetime on Amino-propyl <sup>a</sup> ( $\mu\text{s}$ ) MAP-6', MAP-2	Lower and Upper 95% Confidence Limits ( $\mu\text{s}$ )
<b>1</b>	1.02 (1.4xIncrease)	0.90/1.15		
<b>6'</b>			1.20 (5.1Increase)	0.99/1.4
<b>2</b>	1.91 (8.0xIncrease)	1.86/2.01	1.49 (6.2xIncrease)	1.17/1.92
<b>12</b>	0.71 (3.1xIncrease)	0.66/0.75		

<sup>a</sup> Increases are calculated as ratio of (composite lifetime/solution lifetime)

This is likely due to the fact that the isothiocyanate can react with secondary as well as primary amines while the carboxylate and carbaldehyde linkers in **1** and **12** only react with primary amines. As a result, complex **3** is at least partially bound to secondary amines (~30-35 % of the total) in the PEI polymer backbone, therefore giving an intensity averaged lifetime that is much longer than that of other two complexes, which can only react with the more mobile terminal primary amines. Although **1** has two potential tethers that would be expected to result in less surface mobility, in WP-1 the primary amines (~30-35 % of the total) are present on the surface at widely spaced intervals and statistically it is likely that only one of the two tethers is surface bound at each site. That the lifetime of **1** on the more rigid WP-1 is shorter than on BP-1 could be due to the fact that the primary amines in PEI are linked to the backbone by a two carbon tether, while in BP-1 the amine is linked to the backbone by a one carbon tether. These studies indicate that it is the structure of the polymer and its relative rigidity on the surface rather than the type of tether on the complex that is more important in determining the extent of the increases in the average excited -state lifetime.

To gain insight as to how particle size and shape influence the excited-state lifetimes of the immobilized complexes photophysical measurements were performed on complexes **1**, **2**, **6'** and **12** immobilized on silica nanoparticles modified with PAA (vide supra). The emission spectra for these complexes on the nanoparticles were identical with those on the microparticles. The lifetimes measured for **NPA-1**, **NPA-6'**, **NPA-2** and **NPA-12** were 1.59, 1.51, 0.880 and 0.550 $\mu$ s respectively, which gave the ratios of 2.2, 6.3, 3.6 and 2.5x compared with the lifetimes of the complexes in solution (Table 12).

**Table 12. Comparison of Lifetimes for Complexes in Solution and Complexes on BP-1 Nanoparticles**

<b>Compound</b>	<b>Lifetime <sup>a</sup>(<math>\mu</math>s)</b>	<b>Lower and Upper Confidence Limit(<math>\mu</math>s)</b>
<b>NPA-1</b>	1.59 (2.2x Increase)	1.37/1.90
<b>NPA-6'</b>	1.51 (6.3x Increase)	1.30/1.74
<b>NPA-2</b>	0.88 (3.6x Increase)	0.65/1.20
<b>NPA-12</b>	0.55(2.5x Increase)	0.50/0.55

<sup>a</sup> Increases are calculated as ratio of (composite lifetime/solution lifetime)

This suggests that surface shape has a significant influence on the excited-state lifetime. The microparticles have a local surface that at any given point is relatively flat compared with the radii of the complexes. However, due to the small size of the nanoparticles there is a significant local curvature that can affect interaction of the complexes with the surface. In the case of complex 6', the longer tether is able to extend around the curvature in order to get both anchors attached. By contrast, the shorter tethered dicarboxylate linker in **1** can only anchor at one point due to the small radius of curvature of the nanoparticles. This is consistent with the higher loading of **6'** on the nano and microparticles relative to **1**. In the case of complex **2** on the nanoparticles, the loading is about half that of the microparticles (Figure 18). Although both loadings are quite low relative to the available amines the lower loadings apparently result in a higher mobility on the surface and smaller increases in lifetime. Furthermore, the greater curvature of the nanoparticles could result in less surface interaction of the bulky phosphines with the poly(allylamine), and that would increase surface mobility.

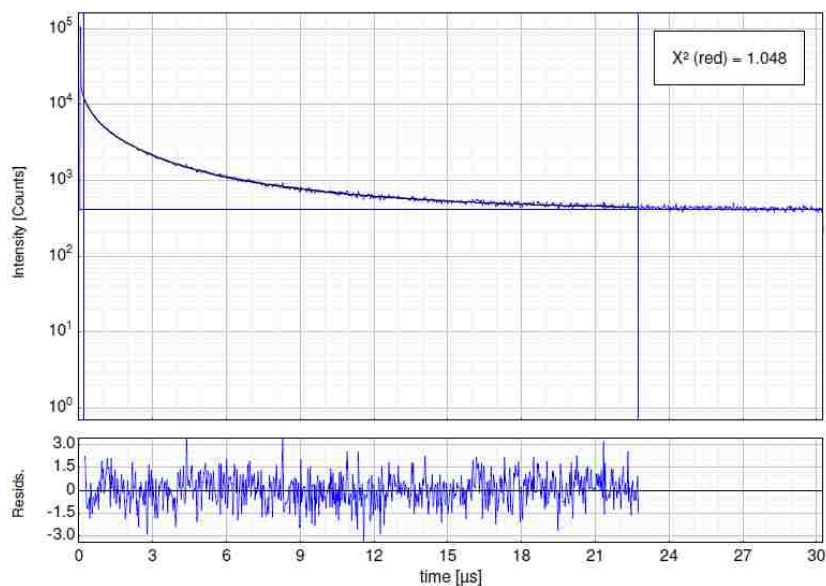


**Figure 27** Lifetime decay curve for MPA-1, with a fitted average lifetime of 3.45us

#### **4.2.6 CO Exchange and Orthometallation**

In order for these complexes to be viable catalytically they require a labile ligand. The likely choice for these complexes was the CO ligand, as has been seen in other published work. In order to test the lability of the CO a simple CO exchange experiment was designed, to see if the natural abundance complexes could be enriched with  $^{13}\text{C}$  after complete synthesis. The results of this test showed that the complex underwent not just simple CO exchange, but instead orthometallation, in which a bond formed between the Ru center and a carbon on the phenyl rings of the  $\text{PPh}_3$  (Figure 28).

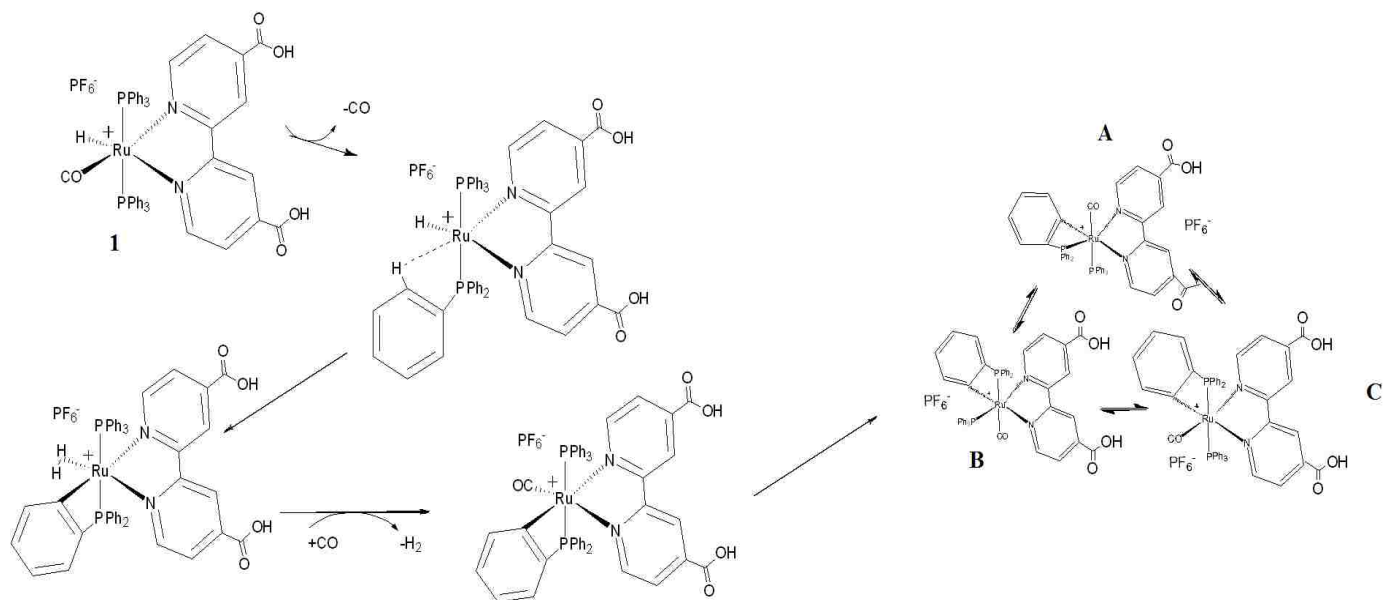


**Figure 28 Mechanism for formation of orthometallated species, and possible isomers**

The orthometallation process occurs when the CO of the complex dissociates, and an intermediate is formed where coordination of an H atom from a phenyl ring takes place, via an agnostic interaction, (Figure 28, I). This hydrogen is then abstracted from the ring and forms a dihydrogen molecule with the original hydride proton. The dihydrogen is then eliminated and a CO molecule replaces it. Three isomers are formed (Figure 28, A,B, and C) as evidenced by the

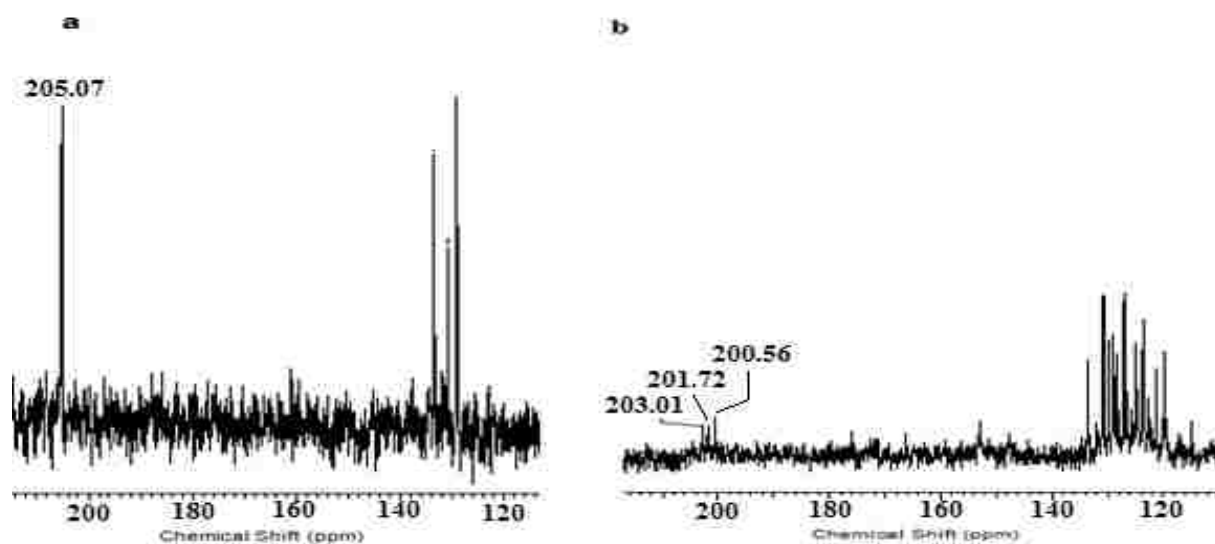


**Figure 29  $^{13}\text{C}$  NMR of complex 1 before orthometallation(a) and after(b)**



appearance of 2 additional metallic CO peaks, and an increase in the complexity of the aromatic region of the NMR, and loss of the hydride signal (Figure 29). NMR evidence has also shown that the more rigid DPPENE chelating phosphine does not have the flexibility to bring a phenyl ring to the proper coordination position to undergo orthometallation. It was also found that under an inert atmosphere of N<sub>2</sub>, without the excess CO available for binding after the dihydrogen molecule is released the complex undergoes rapid decomposition.

These results provided a quick and easy method to determine if the solution state lability of the CO was carried onto the composites once the complex was bound. The exchange experiments were carried out under the same conditions on **MPA-1** with similar results. While the SSNMR data are not as clear as the solution data due to the broad peaks a clear change occurs in both the CO region of **MPA-1** as well as the aromatic region (Figure 30). This supports the idea that the lability of the CO ligand is maintained even after the complex is bound to the surface, supporting the idea that these composites could be catalytically active.

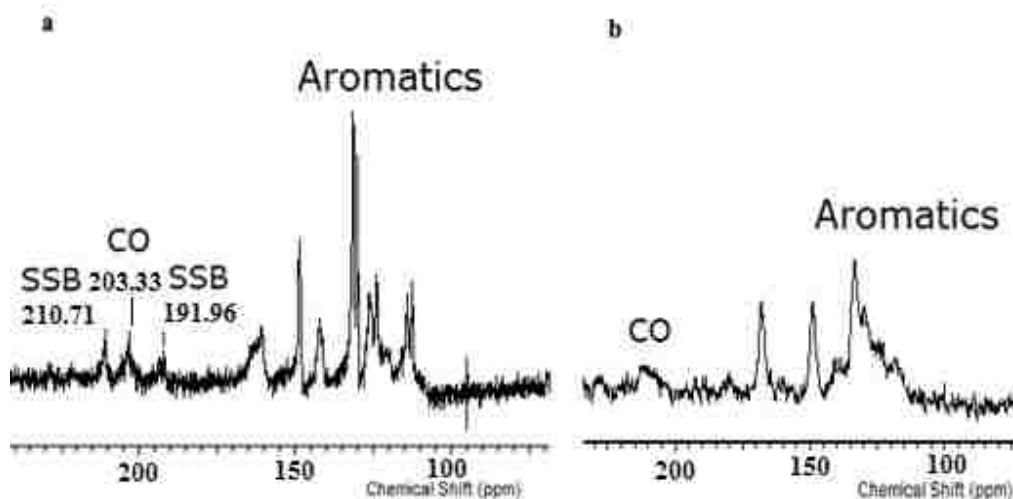


Figure 30 <sup>13</sup>C SSNMR of MPA-1 before(a) and after(b) orthometallation

## 4.3 Experimental

### 4.3.1 Materials

Tetrahydrofuran was distilled from a sodium/benzophenone and methylene chloride and acetonitrile were distilled from calcium hydride. Ruthenium carbonyl was purchased from Strem Chemicals. Diisopropyl ethyl amine (DIPEA), 4,4'-dicarboxy-2,2'-bipyridyl(DcBpy), 3-Diphenylphosphino propionic acid (DPPA), 5-amino-1,10-phenanthroline, 4,4'-Dimethyl-2,2'-dipyridyl and O-benzotriazole-N,N,N',N'-tetramethyl-uronium-hexafluoro-phosphate (HBTU) (Aldrich) were used as received. The SPC, BP-1 and WP-1 microparticles were synthesized by previously reported methods using a 7.5 : 1 mixture of methyltrichlorosilane and 3-chloropropyltrichlorosilane for the silanization step.<sup>56</sup> Silica gel (26.7 nm average pore diameter, 2.82mL/g pore volume, 84.7% porosity, 422m<sup>2</sup>/g surface area) was obtained from INEOS enterprises Ltd., UK, and was sieved to 300-550  $\mu\text{m}$ . The SiO<sub>2</sub> nanoparticles (10-20nm) (Aldrich) were dried at ~200°C before use. The polymers poly(allylamine) (PAA) (PolySciences, MW = 15,000), poly(ethyleneimine) (PEI) (Aldrich, MW=25,000) and the monomer aminopropyltrimethoxysilane (Alfa Aesar) were used as received. The aminopropyl modified micro and nano silica composites were synthesized according to published literature procedures.<sup>123</sup> Complexes **1-3**, **3'** and **5** were synthesized by published literature procedures.<sup>3,67</sup> Silanization of the nanoparticles was done according to published literature procedures with the addition of sonication of the reaction mixtures.<sup>56</sup>

### 4.3.2 Methods

#### 4.3.2.1 Spectroscopic measurements

<sup>1</sup>H and <sup>31</sup>P solution NMR were performed on a Varian NMR Systems spectrometer at 500 and 202.6 MHz respectively. Solid-state CPMAS <sup>13</sup>C, <sup>31</sup>P and <sup>29</sup>Si NMR were obtained on the same

spectrometer at 125, 202.5 and 99.4 MHz respectively using a 4mm rotor at a spin speed of 10 KHz. IR spectra were taken on a Thermo-Nicolet 633 FT-IR spectrometer as KBr pellets. Luminescence data were obtained on a Molecular Devices Spectra Max M2 and by using double-sided carbon tape silica particles were mounted on a glass slide cut to the size of the 1 cm cuvette holder. The angle of the glass slide relative to the excitation beam was adjusted to give maximum emission. Absorbance spectra for the coated silica particles were performed at OLiS Systems using a CLARiTY Spectrometer and were run as suspensions in glycerol.

#### **4.3.2.2 Metal Analysis**

Ruthenium loading data was determined by atomic absorption on an S series Thermo Electron Corporation AA spectrometer after digesting the silica particles. The digestion was performed by first calcining 40mg of the coated particles in an oven at 500°C overnight. The calcined particles were then transferred to polypropylene tubes and combined with 0.5 mL conc. HF acid and 0.5 mL modified aqua regia (6:1 conc. HCl acid : HNO<sub>3</sub> acid), and diluted to 4.5mL total volume with DI water.<sup>124</sup> After dilution each sample was vortexed until particles had completely dissolved and the solution was translucent. Each sample was run in duplicate and standards were run approximately every 12 samples, spanning a linear range on the AA spectrometer of 5-50 ppm.

#### **4.3.2.3 Excited-State Lifetime Measurements**

Time-resolved luminescence decay measurements were performed by time-correlated single-photon counting (TCSPC), using the Quantum Northwest FLASC 1000 fluorimeter (Spokane, WA). The dry silica particles were held in place by double sided carbon tape on the surface of a triangular cuvette 45° to the incident beam. Pulsed excitation at 470 nm and a repetition rate of 50 KHz (external trigger) from a LDH-P-C 470 laser diode (PicoQuant, Berlin,

Germany) was used to excite the complexes for time-dependent studies. In the FLASC 1000 the luminescence decays were collected orthogonal to the excitation beam path and at the magic angle polarization condition<sup>29,94</sup> using a 620/50 nm bandpass filter (Chroma, Rockingham VT) to isolate the emissions and eliminate excitation scatter. Measurements were taken at room temperature under ambient air conditions. The decay curves were collected until  $4 \times 10^4$  counts were reached using the NanoHarp 250 PCI board (PicoQuant, Berlin) with a timing resolution of 560 ps/ channel. Luminescence lifetimes were determined using the FluoFit Pro V4.2.1 (PicoQuant, Berlin) analysis software package<sup>18</sup> and reported as the intensity average based on a multiexponential model, where the magic-angle intensity decay is given by

$$I(t) = \sum_{i=1}^n \alpha_i e^{-t/\tau_i}$$

In this model,  $\tau_i$  is the lifetime and  $\alpha_i$  is the amplitude of the  $i$ th component, and the intensity average lifetime is given by

$$\langle \tau \rangle = \frac{\sum \alpha_i \tau_i^2}{\sum \alpha_i \tau_i}$$

The estimated error in the average was calculated from the upper and lower 95% confidence limits of the individual decay components, which were determined by the support-plane method.<sup>121</sup>

A representative decay curve and the goodness to fit is shown below as Figure 10.

### 4.3.3 Synthesis

All reactions were carried out under inert atmosphere, N<sub>2</sub> or Ar, except during washes and any purification procedures. Overhead stirring was used for all the reactions involving the SPC microparticles as this minimizes particle fragmentation. Sonication of the nanoparticle reactions was carried out with a VWR B1500A-MTH sonicator.

#### 4.3.3.1 Synthesis of *trans*-[(H)Ru(CO)(4'-methyl-2,2'-bipyridine-4-carbaldehyde)(PPh<sub>3</sub>)<sub>2</sub>][PF<sub>6</sub>] (12) and *trans*-[(H)Ru(CO)(4'-methyl-2,2'-bipyridine-4-ethylene glycol acetal)(PPh<sub>3</sub>)<sub>2</sub>][PF<sub>6</sub>] (12')

The ligand 4'-methyl-2,2'-bipyridine-4-carbaldehyde (mbpyc) was synthesized according to previously published procedures.<sup>125</sup> 250mg of Ru(CO)<sub>2</sub>(PPh<sub>3</sub>)<sub>2</sub>(TFA)<sub>2</sub><sup>30</sup> (0.28 mmol) and 70mg (0.28 mmol) of mbpyc were combined in 20mL of ethylene glycol. The mixture was heated to 140°C and stirred for 72hrs. After 72hrs the reaction was cooled to room temperature and the compound was precipitated from solution by the dropwise addition of 1mL of an aqueous solution of NH<sub>4</sub>PF<sub>6</sub> containing 1g/10mL. The precipitate was collected by centrifugation at 3000 rpm and washed 2x in DI H<sub>2</sub>O, followed by centrifugation and then washed 1x with diethyl ether. Following the ether wash and rotary evaporation the product was dissolved in 5:2:2 hexane: MeOH: CH<sub>2</sub>Cl<sub>2</sub> and then chromatographed on neutral alumina using the same solvent as eluent. A single product band containing **4** and **4'** was obtained (35 mg, 13%). IR in KBr: 1986(vs), 1614(vs) 1435 (m) 836(vs). <sup>1</sup>H, <sup>13</sup>C, <sup>31</sup>P and <sup>19</sup>F NMR spectra are shown in Appendix B (Figures B1 – B4). NMR data in CD<sub>2</sub>Cl<sub>2</sub>. <sup>1</sup>H NMR Shifts (δ, relative to TMS): Aldehyde Proton: 8.65 (bs, 0.4H); Bipyridyl Protons: 8.65 (d, 1H), 8.49 + 8(.41 (2d, 1H)), 6.98+6.91(2d, 1H), 6.27+6.19(2d, 1H); Phosphine Phenyl Protons: 7.6-7.2 (m, 32H, includes 2 overlapping bipyridyl protons); Acetal Protons: 4.86(s, 0.3H) 4.73(s, 0.3H) 3.70(m, 0.6H) 3.45(m, 0.6H); Acetal Methyl Protons: 2.54 (s, 0.9H), 2.50(s, 0.9H) Aldehyde methyl protons: 2.48(s, 0.6H), 2.43(s, 0.6H), Hydride: -11.32(m, 1H). <sup>13</sup>C NMR shifts (δ relative to TMS): Metal CO: 205.2; 8 Bipyridyl quaternary carbons: 155.07, 154.77, 154.26, 154.08, 151.91, 151.49, 151.26, 150.92; 8 Bipyridyl CH carbons: 127.82, 127.56, 125.84, 125.69, 124.26, 123.99, 122.00, 121.79; Aldehyde: 152.6,

152.5; PPh<sub>3</sub> quaternary carbons: 132.20(t); PPh<sub>3</sub> CH + 4 bpy CH carbons: 133.65, 130.61, 128.92; Acetal CH: 73.98 (bs); Acetal carbons: 70.61(CH), 70.35(CH), 61.46(CH<sub>2</sub>), 61.35(CH<sub>2</sub>); Methyl: 21.3, 21.2. <sup>31</sup>P NMR shifts (δ relative to external H<sub>3</sub>PO<sub>4</sub>): PPh<sub>3</sub>, 46.04 (2P), PF<sub>6</sub><sup>-</sup>, 139 (1P). <sup>19</sup>F NMR shifts (δ relative to external CFCl<sub>3</sub>): PF<sub>6</sub><sup>-</sup>: -74(d).

#### **4.3.3.2 General procedure for coupling of complexes 1 and 6' to the composites with HBTU:<sup>1,2</sup> synthesis of MPA-1, MPE-1, MPA-6', MAP-6', NPA-1, NPA-6'**

75 mg of the complex **1**<sup>30</sup>(0.07mmol), was dissolved in 20 mL of CH<sub>2</sub>Cl<sub>2</sub> in a round-bottom flask, along with 35 mg HBTU (0.09mmol), and 0.09 mL DIPEA (.5mmol). The reaction mixture was top stirred for a 30-minute activation period at 25°C, after which 250 mg of **BP-1** microparticles was added to the flask. Following the addition of the **BP-1**, the reaction mixture was top stirred for an additional 3 hours. The reaction was then stopped by removing the solvent from the particles, and ~20 mL of MeCN were added and the mixture stirred for 1 hour. This process was repeated 3 times after which the particles were collected and dried on a vacuum line.

**Spectroscopic data for MPA-1:** IR in KBr: 2956 (m, C-H), 2926(m, C-H), 1952 (w, metal CO), 1675 (s, amide CO), 1620 (m, amide CO), 1534(w, carboxylate ion), 1399 (w, carboxylate ion), 840(s, diimine ring) cm<sup>-1</sup>. <sup>31</sup>P{<sup>1</sup>H} SS NMR δ 44.2, -145. <sup>13</sup>C{<sup>1</sup>H} SSNMR δ 203 (metal CO), 170-160 (amide), 150-110 (aromatics), 55-20 (polymer), -6 (Si-Me).

**Spectroscopic data for MPE-1:** IR in KBr: 2964(m, C-H), 2918(m, C-H), 1938 (w, metal CO), 1672 (s, amide CO), 800(s, diimine ring). <sup>31</sup>P{<sup>1</sup>H} SSNMR δ 46, -145. <sup>13</sup>C{<sup>1</sup>H} SSNMR δ 203 (metal CO), 160-170 (amide), 150-120 (aromatics), 50-20 (polymer), -6 (Si-Me).

**Spectroscopic data for MPA-6'**: IR in KBr: 2926(m, C-H), 1944(w, metal CO), 1674 (s, amide CO), 799 (s, diimine ring)  $\text{cm}^{-1}$ .  $^{31}\text{P}\{^1\text{H}\}$  SSNMR  $\delta$  38, -145.  $^{13}\text{C}\{^1\text{H}\}$  SSNMR  $\delta$  203 (metal CO), 170-160 (amide), 150-110 (aromatics), 60-15 (polymer), -6 (Si-Me).

**Spectroscopic data for NPA-1**: IR in KBr: 2926(m, C-H), 1947(w, metal CO), 1672 (s, amide CO), 1558 (w, carboxylate ion), 1397 (w, carboxylate ion), 840(s, diimine ring)  $\text{cm}^{-1}$ .  $^{31}\text{P}\{^1\text{H}\}$  SSNMR  $\delta$  38, -145.  $^{13}\text{C}\{^1\text{H}\}$  SSNMR  $\delta$  170-160 (amide), 150-110 (aromatics), 11.1(C<sub>1</sub>), 21.5(C<sub>2</sub>), 44.6(C<sub>3</sub>) (Aminopropyl Chain).

**Spectroscopic data for NPA-6'**: IR in KBr: 2924(m, C-H), 1956(w, metal CO), 1733 (w) 1646 (s, amide CO), 1540 (w, carboxylate ion) 1399 (w, carboxylate ion), 798(s, diimine ring)  $\text{cm}^{-1}$ .  $^{31}\text{P}\{^1\text{H}\}$  SSNMR  $\delta$  46, -145.  $^{13}\text{C}\{^1\text{H}\}$  SSNMR  $\delta$  203 (Metal CO), 170-160 (amide), 155-110 (Aromatics), 44.8 (C<sub>3</sub>), 24.3 (C<sub>2</sub>), 8.6 (C<sub>1</sub>), (aminopropyl Chain) 50-15 (polymer), -6 (Si-Me).

#### **4.3.3.3 General Procedure for coupling complexes 2 and 8 to the composites via the isothiocyanate intermediate:<sup>3,4</sup> synthesis of MPA-2, MPE-2, MPA-8, NPA-2**

75mg (0.13 mmol) of complex **3**<sup>3</sup> was dissolved in 3 mL of dry acetone. Finely crushed  $\text{CaCO}_3$  (30 mg, 0.45 mmol) was added to the solution followed by addition of thiophosgene (7.5  $\mu\text{L}$ , 0.07 mmol). The reaction mixture was stirred at room temperature for 1 hour and then refluxed for 2.5 hour. After cooling to room temperature,  $\text{CaCO}_3$  was removed using a 0.45- $\mu\text{m}$  filter, and acetone removed by rotary evaporation. Compound  $[(\text{H})\text{Ru}(\text{CO})(\text{dppene})(1,10\text{-phen-5-NCS})][\text{PF}_6]$  (**3'**)<sup>23</sup> obtained in 94% yield. IR in KBr: CO stretching frequency at 1990 (vs),  $\text{N}=\text{C}=\text{S}$  at 2119 (m) and 2046 (m)  $\text{cm}^{-1}$ .

Conversion of **3'** to **3** was performed by dissolving 75mg of **3'** in 20mL of  $\text{CH}_2\text{Cl}_2$  in a round bottom flask, along with 250mg of BP-1 microparticles. The reaction mixture was stirred at 25°C overnight. The reaction was stopped by separating the particles from the solvent and

washing 3x with fresh 20mL aliquots of CH<sub>2</sub>Cl<sub>2</sub> with stirring for 1 hr. each wash. After washing the particles were collected and vacuum dried.

**Spectroscopic data for MPA-2:** IR in KBr: 2924(m C-H), 2000(w, C-H), 1646 (s), 1399 (m, C=S), 798(s, diimine) cm<sup>-1</sup>. <sup>31</sup>P{<sup>1</sup>H} SSNMR δ 45, -145. <sup>13</sup>C{<sup>1</sup>H} SSNMR δ 203 (metal CO), 162 (C=S), 150-110 (aromatics), 60-15 (polymer), -6 (Si-Me).

**Spectroscopic data for MPE-2:** IR in KBr: 2964(m, C-H), 2921(m, C-H), 1991 (w, metal CO), 1676 (s), 1399 (m, C=S), 796(s, diimine ring) cm<sup>-1</sup>. <sup>31</sup>P{<sup>1</sup>H} SSNMR δ 66, -145. <sup>13</sup>C{<sup>1</sup>H} SSNMR δ 207 (Metal CO), 162 (C=S), 150-120 (Aromatics), 55-20 (Polymer), -6 (Si-Me).

**Spectroscopic data for MPA-8:** IR in KBr: 2950(s, C-H), 2935(s, C-H), 1400 (s, C=S), 790(vs, diimine) cm<sup>-1</sup>. <sup>13</sup>C{<sup>1</sup>H} SSNMR δ 163(C=S), 100-160 (Aromatics), 60-20 (Polymer), -6 (Si-Me).

**Spectroscopic data for NPA-2** IR in KBr: 2945(s, C-H), 2932(s, C-H), 1996 (w, metal CO), 1644(s), 1398 (s, C=S), 795(vs, diimine) cm<sup>-1</sup>. <sup>31</sup>P{<sup>1</sup>H} SSNMR δ 60, -145. <sup>13</sup>C{<sup>1</sup>H} SSNMR δ 202 (Metal CO), 162(C=S), 135-110 (Aromatics), 45 (C<sub>3</sub>), 24.3 (C<sub>2</sub>), 8.3 (C<sub>1</sub>), 50-15 (Polymer), -6 (Si-Me).

#### **4.3.3.4 General procedure for the coupling of complex 12 to the composites by direct reaction with the composites: synthesis of MPA-12, MPE-12 and NPA-12**

75 mg of the complex 4 (0.07 mmol), was dissolved in 20 mL of CH<sub>2</sub>Cl<sub>2</sub> in a round-bottom flask along with 250 mg of BP-1 microparticles. Following the addition of the BP-1, the reaction mixture was top stirred for an additional 3 hours. The reaction was then stopped by removing the solvent from the particles, and ~20mL of fresh CH<sub>2</sub>Cl<sub>2</sub> were added to wash the particles. The wash was achieved by top stirring the particles for 1 hour and then removing the solvent, repeating the process 3 times. After the third wash the particles were collected and dried on a vacuum line.



**Spectroscopic data for MPA-12:** IR in KBr: 2926(m, C-H), 1986 (w, metal CO), 1634 (s, C=N), 1562 (m), 798(s)  $\text{cm}^{-1}$ .  $^{31}\text{P}\{^1\text{H}\}$  SSNMR  $\delta$  44, -145.  $^{13}\text{C}\{^1\text{H}\}$  SSNMR  $\delta$  203 (Metal CO), 162 (C=N), 140-120 (Aromatics), 40-20 (Polymer), -6 (Si-Me).

**Spectroscopic data for MPE-12:** IR in KBr: 2970(m, C-H), 2920(m, C-H), 1957 (w, metal CO), 1672 (s, C=N), 1584 (m), 798(s, diimine)  $\text{cm}^{-1}$ .  $^{31}\text{P}\{^1\text{H}\}$  SSNMR  $\delta$  45, -145.  $^{13}\text{C}\{^1\text{H}\}$  SSNMR  $\delta$  163 (C=N), 140-120 (aromatics), 40-20 (polymer), -6 (Si-Me).

**Spectroscopic data for NPA-12:** IR in KBr: 2926(m, C-H), 1989 (w, metal CO), 1650 (s, C=N), 798(s, diimine)  $\text{cm}^{-1}$ .  $^{31}\text{P}\{^1\text{H}\}$  SSNMR  $\delta$  59, -145.  $^{13}\text{C}\{^1\text{H}\}$  SSNMR  $\delta$  202 (metal CO), 151 (C=N), 135-110 (Aromatics), 45 ( $\text{C}_3$ ), 24.3 ( $\text{C}_2$ ), 8.3 ( $\text{C}_1$ ), 50-15 (Polymer), -6 (Si-Me).

#### 4.3.3.7 Orthometallation Procedure in Solution

100mg (0.1mmol) of complex **1** was dissolved in 15mL of THF with  $^{13}\text{CO}$  gas bubbling through. The mixture was then refluxed overnight, ~16hrs. After cooling to room temperature and venting excess CO, the THF was removed by rotary evaporation and the product was dried overnights under vacuum. IR in KBr: CO stretches at 1995(s), 1958(s), 1902(s), Diimine ring; 840(s)  $\text{cm}^{-1}$ .  $^1\text{H}$  NMR (d6-Acetone  $\delta$ ) 7-8.2 Aromatics.  $^{12}\text{C}\{^1\text{H}\}$  202.92 (Metal CO), 201.71 (Metal CO), 200.56 (Metal CO), 136-115 (Aromatics).  $^{31}\text{P}\{^1\text{H}\}$  49 (2P), 144 (1P)

#### 4.3.3.8 Ortho Metallation on MPA-1

100mg of MPA-1 was placed in 15mL of THF with  $^{13}\text{CO}$  bubbling through. The reaction mixture was then refluxed overnight with no stirring, using only the reflux and bubbling for agitation. After refluxing overnight the mixture was cooled to room temperature and the composite was collected via filtration. The composite was then washed 3x with clean THF and dried overnight under vacuum. IR in KBr: CO stretches at 1995 (w), 1956 (w), Amide stretch

1660 (s)  $\text{cm}^{-1}$ .  $^{13}\text{C}$  SSNMR 206(bs) Metal CO's, 166(s) Amide, 150-100(m) Aromatics.  $^{31}\text{P}$   
SSNMR 60 (s)  $\text{PPh}_3$ , -140 (q)  $\text{PF}_6$ .

## Chapter 5 Applications of Surface Bound Ruthenium Complexes

### 5.1 Introduction

In recent years the idea that our society may soon be reaching the point where the raw materials for the goods and services we depend on, will one day run out, has been becoming more widespread. Even more important still is how connected all our goods and services have become, especially in a spatial sense, as society grows, goods that were once widely dispersed have now begun to be produced in the same areas. In order to maintain and improve our way of living the focus of a great deal of research has been on either using materials more efficiently with less waste, or being able to reclaim and recycle what was once considered waste into new raw materials. Another big step has been in insuring that what is disposed of as waste does not contaminate or pollute other systems and ruin those sources of raw materials.

As stated previously SPC's were designed to selectively target and extract metals from mining waste streams. It has also been shown that the emission intensity of a luminescent complex can be either diminished or enhanced by the presence of certain atoms<sup>11,26,126-128</sup>. So SPC's in conjunction with a luminescent probe could lead to the development of a metal selective sensor that can be measured by UV-Vis Spectroscopy, particularly, luminescence. The advantage that this could have over current methods is, the relative simplicity and low cost of UV-Vis spectroscopy over other detection methods, along with its low limit of detection and low background interference. UV-Vis spectroscopy also has an advantage of the speed at which samples can be measured. This would lead to a low cost quick method of determining levels of metal runoff in waste streams, to determine whether they are worth reclaiming or are within safe limits.

The work currently being done has shown that the effect on emission intensity is applicable to surface bound probes and the selectivity of the surface does play some role in the level of change. We have undertaken a study to fully understand the processes that occur when a metal ion in solution is adsorbed onto the coordinating amines of an SPC that has a luminescent Ru complex bound to its surface.

## 5.2 Results

### 5.2.1 Metal Sensing

The material chosen to be tested was **MPA-1**, due to its high yields in synthesis as well as strong luminescence. The initial studies began with the testing of divalent metals, which were

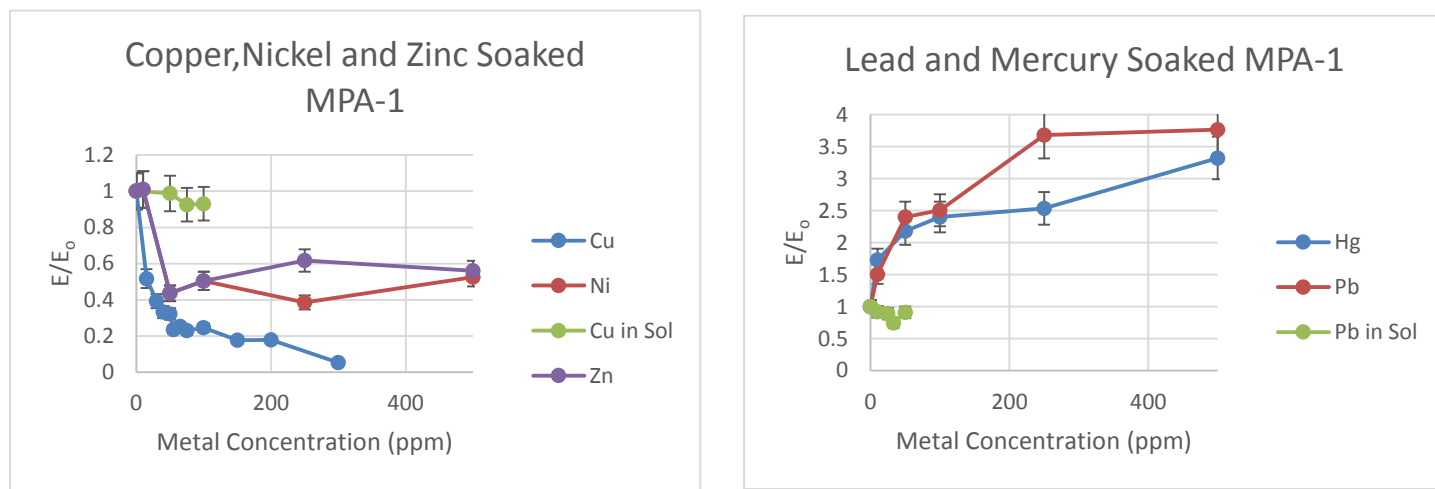


**Figure 31** Graphs showing change in emission for MPA-1 composite after soaking in various concentrations of toxic metals

known to have a good binding affinity to the BP-1 surface. We have found that the presence of lighter transition metals, such as  $\text{Cu}^{2+}$ ,  $\text{Ni}^{2+}$ , and  $\text{Zn}^{2+}$  resulted in a loss of emission intensity. Heavier divalent metals tested such as  $\text{Pb}^{2+}$  and  $\text{Hg}^{2+}$  showed an enhancement of the emission from the bound ruthenium complex. (Figure 31)

The quenching and enhancement process were shown to be static, requiring the binding of the metal ion to the surface in close proximity to the complex. This was shown by repeating

some of the experiments in solution where neither quenching nor enhancement occurred, as well as by comparing the Stern-Volmer plot of the quenching by  $\text{Cu}^{2+}$  to its normalized lifetime. This plot shows that while the emission of the complex is dependent on the concentration of the quenching metal, the lifetime does not change significantly as concentration increases. (Figure 32) Both quenching and enhancement have a maximum level of effect that appears to be based upon the loading capacity of a given metal to the surface. (Figure 31)

While it is shown that the quenching is a static process the actual mechanism through which the quenching occurs is still under study, there are two possibilities discussed in the literature, a redox-reaction of the Ru(II)-M(II) couple or an energy transfer between the MLCT state and the quenching metal center.<sup>127-129</sup> At the moment the most likely theory is that after the metal to ligand charge transfer occurs on the luminescent complex, the excited electron is transferred to the nearby quencher and undergoes non-radiative decay back to the ground state.

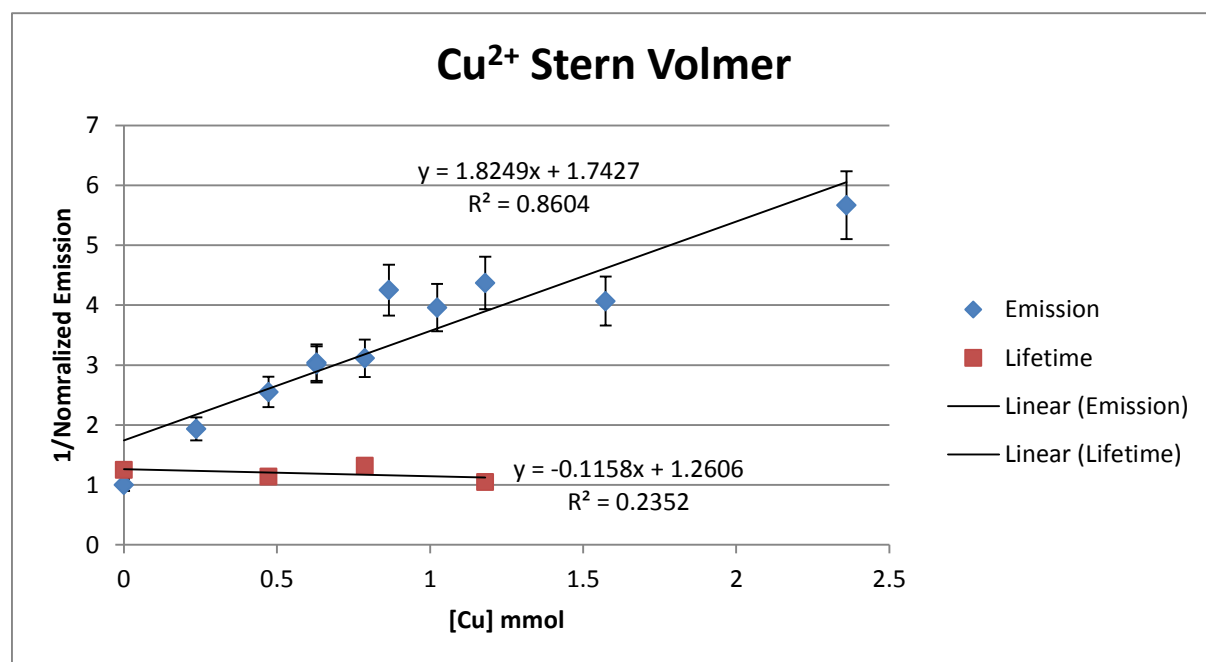
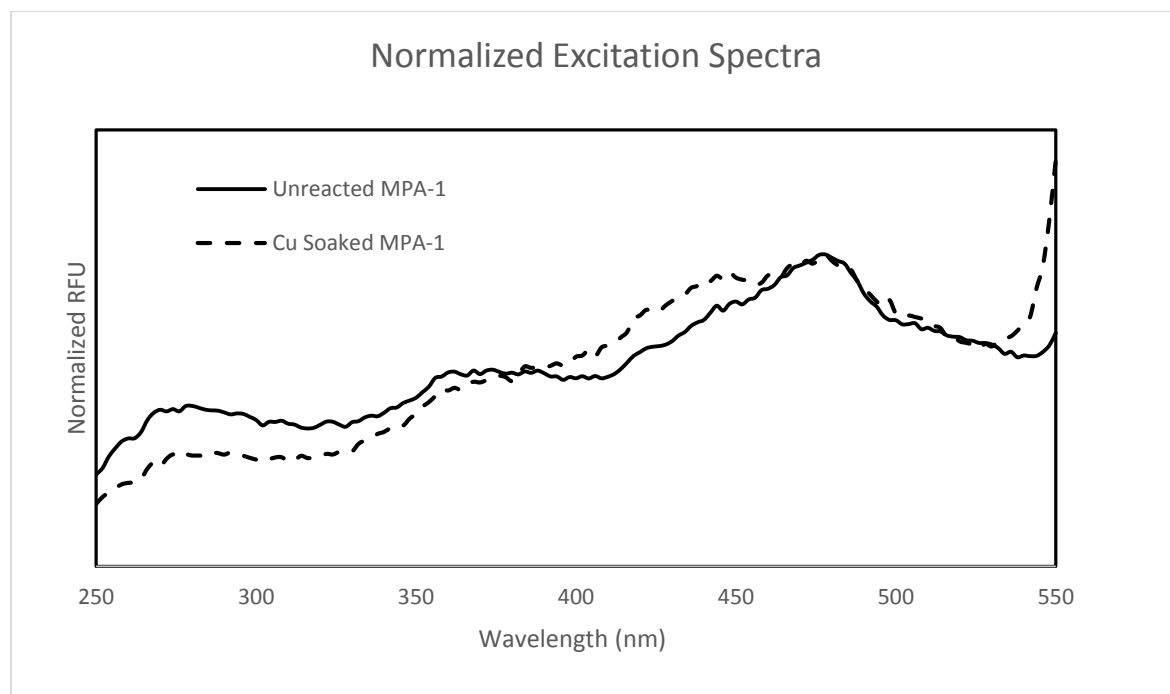


Figure 32 Stern Volmer Plot showing change in emission vs [quencher] without change in lifetime which is indicative of a static quenching mechanism

Initial EPR data has also supported this mechanism as there is no Ru(III) detected on the surface after reaction with the quenching metal.



**Figure 33 Comparison of Unreacted and Cu Soaked MPA-1 Excitation spectra, showing the lack of change in energy levels contributing to the emission.**

The mechanism behind the enhancement is most likely an increase in intersystem crossing between the  $^1\text{MLCT}$  and the  $^3\text{MLCT}$  state by the external heavy atom effect. This effect arises from the ability of heavy atoms to engage in spin orbit coupling with the luminescent complex which stabilizes the excited triplet state and leads to an increase in electrons through this pathway. This theory is well documented in literature and again supported by a lack of change in the excitation spectra.<sup>129</sup>(Figure 33)

### 5.3 Methods

Metal salts were obtained from EMD Chemicals and used without further purification. 500ppm stock solutions were made for the  $\text{Ni}^{2+}$ ,  $\text{Zn}^{2+}$ ,  $\text{Pb}^{2+}$ ,  $\text{Hg}^{2+}$ , and  $\text{U}^?$ , and a 1500ppm stock solution was used for  $\text{Cu}^{2+}$ , by dissolving the correct amount of hydrated metal salt into 1 L of

DI water. From the stock solutions, sample concentrations were made by diluting an appropriate volume of the stock solution into DI water to a final volume of 10mL. The **MPA-1** material was synthesized according to previously reported methods.

For each sample ~50 mg of **MPA-1** was placed in a scintillation vial and covered with 10mL of a given concentration of the metal salt solution. These mixtures were then shaken on a Precision Scientific 360 Orbital Shaker Bath at room temperature, for 24hrs. After 24 hrs the liquid was decanted off and the material and ~10mL of DI water was added and the mixture was sonicated for ~1 min, this procedure was repeated 3 times. After washing the material was placed in an oven overnight at 60°C and .5 atm in order to remove any trace of water remaining. Once the samples were dried they were tested for luminescence levels using the same method as previously reported.

In solution trials were done by creating a .5ppm stock solution of the Ru complex in reagent grade acetone, this concentration when at the 10mL final volume is approximate to the ruthenium concentration on the surface. 1mL of the stock ruthenium solution was then combined with appropriate amounts of the metal salt stock solutions to achieve the desired concentration when the total volume was brought to 10mL with DI water. The solution was then shaken for 24hrs and tested using the previously reported method from Chapter 3. Lifetime measurements were performed by the same method as previously reported in Chapter 2. The error reported for the emission data for both quenching and enhancement is the dilution error, as the error in the emission spectra is significantly smaller.

## Chapter 6 Conclusions and Future Work

### 6.1 Conclusions

#### 6.1.1 Bioconjugation of Ruthenium Complexes

Three ruthenium-based luminescent bioconjugates with only one diimine ligand have been designed and synthesized as membrane probes. The steady-state and time-dependent photophysical properties of these complexes were studied in solution and in model membrane environments, in which the probes were distributed between the inner and outer surfaces of the lipid bilayer (see Figure 12). An important part of the design of the conjugates was the use of phosphine ligands, which have previously been shown to improve luminescence quantum yields.<sup>79,80</sup> Lipid conjugates **3**, **4**, and **7** showed unexpectedly blue-shifted, relatively intense emissions with short, nanosecond excited state lifetimes in solution and in the LUVs. In the LUVs these emissions were sensitive to changes in membrane viscosity. These complexes would not be useful for studying the microsecond-time scale dynamics on membranes, but could be useful for nanosecond-time scale processes. These results sharply contrast with the previously reported tris-diimine lipid conjugates, which exhibited the typical red-shifted, long-lived emissions.<sup>60,62,63,67</sup> The cholesterol complexes **5**, **9**, and **10** could be used as probes for studying the slower dynamics. Our results point to the sensitivity of the transition-metal complex–lipid interaction to the ancillary ligands of the complex. A similar blue shift and short decay time were recently observed for the related complex  $[\text{Ru}(\text{bpy})_2(\text{dpp})]^{2+}$  (dpp = 2,3-bis(2-pyridyl)pyrazine) upon protonation of the pyrazine nitrogen.<sup>130</sup> This suggests that these blue shifts are due to perturbations in the orbital energies of the diimine ligand, and this suggestion is further supported by the absence of the blue shift in complexes **9** and **10**. The cholesterol conjugate **5** incorporated in phosphatidylcholine LUVs had lifetime and anisotropy decays that were



sensitive to temperature-dependent motions, and conjugation to cholesterol did not significantly perturb the fundamental anisotropy. In addition, the comparison with the tris-diimine cholesterol conjugate 9 revealed that having only one diimine results in a greater fundamental luminescence anisotropy. In summary, the unusual behavior of lipid conjugates **3**, **4**, and **7** relative to complex **10** points to the importance of the phosphine ligands in controlling photophysical properties via their contribution to the excited state electron distribution when present in combination with multiple vibrational modes of the attached lipids. These contributions are not apparent in the excitation spectra of complexes **8–10**.

### **6.1.2 SPC Nanomaterials**

The work done on creating nano scale SPCs showed that it was possible to do the same surface chemistry on both micrometer and nanometer sized particles. It was also shown that the increase in the surface area to volume ratio that the nanoparticles provided an increase in copper capacity for the material. One drawback that was seen for the use of nanoparticles over microparticles was in the catalysis study, where the nanoparticles were not as effective at catalyzing the Knoevenagel reaction as the microparticle analogs.

This lack of effectiveness is likely due in part to two factors, initial aggregation, and surface crowding. The experiments showed that in order for the nano materials to reach their maximum rate of conversion, they needed to be sonicated before addition of the reactants, in order to break up any aggregates. Even after being presonicated there was still some lag time before catalysis was seen, indicating that it required time for the reactants to access an active surface on the nanoparticles.

Further conclusions from this study showed that while the polymer surface is less effective as a catalyst itself when compared to the monomeric analog, 3-aminopropyl, the

benefits the polymer adds in the terms of physical and chemical stability are important. This was seen on both the micro and nano scale materials. With the micro scale it was evident that the monomer could not provide the same physical stability as the materials would grind into powder under normal reaction conditions. The nanoparticles did not face the compromise of their physical stability as much as their chemical stability. Through SSNMR it was shown that the anchors of the chloropropyl groups would hydrolyze off the surface more readily from the nanoparticles than the microparticles.

### **6.1.3 Binding of Ruthenium Complexes to SPCs**

The results of this study have shown that binding of an organometallic ruthenium complex to a surface does not significantly affect its absorbance or emission properties. This indicates that interactions with the polyamine and aminopropyl/silica surfaces do not affect the transition energies involved in the MLCT bands of these complexes. However, the average excited-state lifetime is markedly affected. The studies reported here suggest that the relative rigidity of the surface is a major contributor to this phenomenon. In addition, there are significant differences between the excited-state lifetimes when on micro- versus nano-particles. We have tentatively assigned these differences to the different surface shapes of the micro- and nano-SPC.

In the case of complex **5**, there is only a slight difference in excited-state lifetime relative to its solution value. This result points to the importance of the ancillary ligands in increasing the excited-state lifetime of the immobilized complex. The origin of this effect could be steric or electronic, or both. Complex **5** has a smaller molecular volume than the phosphine-containing complexes as can be seen from the closed-packed, hard-sphere models shown in Figure 9. Thus the bulky phosphines could interact more with the surface polyamine, for example, while **5** might

move more freely on the surface. On the other hand, excited-state lifetimes are subject to a number of electronic effects. The excitation spectra clearly indicate the participation of the phosphine ligand in the MLCT and this affects the degree of spin-orbit coupling, delocalization of electron density in the excited state as well as the perturbation of LUMO and HOMO energies. We have observed differences in the photophysical properties between **5** and complexes **1-3** on bioconjugation and on incorporation into liposomes, which perhaps are related electronic effects.<sup>3</sup> These are complex issues that might be addressed by TDDFT in combination with molecular mechanics calculations. This is planned for the future. These studies open the door for detailed investigation of the electron transfer properties of the immobilized complexes **1-4**. The longer lifetimes promise lower activation energies for electron transfer which could increase the rates of carbon dioxide reduction, a transformation where ruthenium diimine complexes have been shown to be promising.<sup>69</sup> The complexes are air stable, and so far, show no decomposition when irradiated after immobilization on SPC.<sup>30,116,131</sup> These studies are under way in our laboratory.

#### **6.1.4 Applications of SPC Bound Ruthenium Complexes**

##### **6.1.4.1 Metal Sensing**

Though there is still a great deal of work to be done regarding the use of these complexes as a possible metal sensors in aqueous solutions, some important results have already been discovered. The biggest conclusion that can be drawn from the work done so far is that the luminescent properties of the complexes are affected by the binding of transition metals to the surface. The effects each metal has on the complex has been shown to be dependent on several different factors.

The results have shown that luminescence is either enhanced or quenched depending on whether or not the transition metal ion bound is able to engage in spin orbit coupling with the ruthenium complex, with those that are able to, creating an enhancement in luminescence. The maximum level of effect on the luminescence is also dependent on the metal ion and its affinity for binding to the surface. Both processes have been shown to be static, requiring that the metal is bound to the surface, through comparison of the changes in emission levels on the surface and in solution.

## **6.2 Future Work**

### **6.2.1 Optimization**

#### **6.2.1.1 Loading**

One of the biggest improvements that needs to be made with these materials, is a true optimization of the loading on a larger scale. Some minor optimizations were done previously but on a small scale that is impractical for the variety of experiments these materials are now being used for.

This comprehensive optimization needs to be done at a practical scale and needs to take into account all the major components that the materials were designed for, emission, lifetime and loading. The optimization will also need to take into account what the materials are being used for. For example the metal sensing may require a lighter loading of the material, as high density loading will create pockets of inaccessible luminescent complexes for the transition metal ions, and lead to less change in the emissions. The catalysis on the other hand will likely benefit from higher density loading, both thermally and photochemically.

### 6.2.1.2 Metal Sensing

Optimization for the metal sensing needs to focus on optimizing the method used. The most important factor to optimize is time. The rapid speed of UV-Vis measurements as well as the low cost required is what gives this material an advantage over systems such as AA and ICP, however, if the time required to create a sample is significantly slower this will offset the savings significantly. In order to optimize the time required several tests need to be done varying not only the time the material is in contact with the solution but also in the number of washes, as well as drying time and temperature.

Another important optimization for these materials is sample amount. The luminescent materials are expensive to make, so using as little as possible should be a key goal. Reducing the amount of test solution as much as possible should also be addressed. This would limit exposure to possibly harmful solutions as well as reduce disposal, and handling costs.

### 6.2.1.3 Catalysis

Work done over the course of the previous projects has shown that the ruthenium complexes anchored to the SPC composites have the potential to be a new heterogeneous catalysis platforms. There are several factors that need to be considered and optimized prior to their use as catalysts. One important consideration is the choice of reaction to be catalyzed. Complexes such as **1-4** these have been shown to be effective dehydrogenation and transfer catalyst for primary alcohols<sup>32-36</sup>. The problem this platform will have with these types of reactions though is the final product of the catalysis is an aldehyde, which we know through the coupling of compound **4**, is a very reactive functional group to the primary amines on the surface. In order to utilize these materials as effective catalysts it will be necessary to modify the

surface in some way that prevents the reaction of the product aldehyde with the amines remaining on the surface.

### **6.2.2 Metal Sensing Selectivity**

In order to truly determine if luminescent SPC's have a possibility of being used as metal sensors in real world applications several more studies need to be done. The first study that should be done is an understanding of how the luminescence of the materials is affected by a mixed metal solution, as at the moment all studies have been done using a single metal ion solution. Along the same lines, attempts need to be made to modify the material with additional ligands that have been previously shown to increase the affinity of certain metals to the surface. This could possibly increase efficiency but also selectivity of detection. Other studies that should be performed involve the use of different valencies for the metal ions, as of writing only +2 metals have been studied, as well as the effects of various aminoic species.

## Bibliography

- (1) Carpino, L. *J. Am. Chem. Soc.* **1993**, 4397.
- (2) Zhan, W.; Jiang, K.; Smith, M.; Bostic, H.; Best, M.; Auad, M.; Ruppel, J.; Kim, C.; Zhang, X. *Langmuir* **2010**, 15671.
- (3) Sharmin, A.; Salassa, L.; Rosenberg, E.; Ross, J. B. A.; Abbott, G.; Black, L.; Terwilliger, M.; Brooks, R. *Inorg. Chem.* **2013**, 52, 10835.
- (4) Szmecinski, H.; Terpetschnig, E.; Lakowicz, J. R. *Biophys. Chem.* **1996**, 109.
- (5) Lippincott-Schwartz, J.; Patterson, G. H. *Science* **2003**, 300, 87.
- (6) Martin, L. J.; Hähnke, M. J.; Nitz, M.; Wöhnert, J.; Silvaggi, N. R.; Allen, K. N.; Schwalbe, H.; Imperiali, B. *Journal of the American Chemical Society* **2007**, 129, 7106.
- (7) Giepmans, B. N. G.; Adams, S. R.; Ellisman, M. H.; Tsien, R. Y. *Science* **2006**, 312, 217.
- (8) Allen, K. N.; Imperiali, B. *Current Opinion in Chemical Biology* **2010**, 14, 247.
- (9) Cohen, B. E.; McAnaney, T. B.; Park, E. S.; Jan, Y. N.; Boxer, S. G.; Jan, L. Y. *Science* **2002**, 296, 1700.
- (10) Saxton, M. J.; Jacobson, K. *Annual Review of Biophysics and Biomolecular Structure* **1997**, 26, 373.
- (11) Fernández-Argüelles, M. T.; Jin, W. J.; Costa-Fernández, J. M.; Pereiro, R.; Sanz-Medel, A. *Analytica Chimica Acta* **2005**, 549, 20.
- (12) Lehmann, O.; Kömpe, K.; Haase, M. *Journal of the American Chemical Society* **2004**, 126, 14935.
- (13) Dadak, V.; Vanderkooi, J. M.; Wright, W. W. *Biochim. Biophys. Acta* **1992**, 110, 33.
- (14) Bartholdi, M.; Barrantes, F. J.; Jovin, T. M. *Eur. J. Biochem.* **1981**, 120, 389.
- (15) Che, A.; Cherry, R. J. *Biophys. J.* **1995**, 68, 1881.
- (16) Kinoshita, K.; Kawato, S.; Ikegami, A. *Biophys. J.* **1977**, 20, 289.
- (17) Kinoshita, K.; Ikegami, A.; Kawato, S. *Biophys. J.* **1982**, 37, 461.
- (18) Minazzo, A. S.; Darlington, R. C.; Ross, J. B. A. *Biophys. J.* **2009**, 96, 681.
- (19) Karakhanov, E.; Maximov, A.; Kardashev, S.; Kardasheva, Y.; Zolotukhina, A.; Rosenberg, E.; Allen, J.; Nanostructured Macromolecular Metal Containing Materials in Catalysis in *Macromolecular Symposia*, 304(Macromolecular Complexes) 2011
- (20) Koch, F.; Petrova-Koch, V.; Muschik, T. *Journal of Luminescence* **1993**, 57, 271.
- (21) Townsend, P. D., Maghrabi, M., Yang, B. *Nuclear Instruments and Methods in Physics Research B* **2002**, 767.
- (22) Wang, Y.; Yang, B.; Townsend, P. D. *Luminescence : the journal of biological and chemical luminescence* **2013**, 28, 253.
- (23) Richards, B. S. *Solar Energy Materials and Solar Cells* **2006**, 90, 1189.
- (24) Huang, X.; Han, S.; Huang, W.; Liu, X. *Chemical Society Reviews* **2013**, 42, 173.
- (25) Wahler, D.; Reymond, J.-L. *Current Opinion in Biotechnology* **2001**, 12, 535.
- (26) Valeur, B.; Leray, I. *Coordination Chemistry Reviews* **2000**, 205, 3.
- (27) Lippitsch, M. E.; Draxler, S.; Kieslinger, D. *Sensors and Actuators B: Chemical* **1997**, 38, 96.
- (28) Rurack, K.; Resch-Genger, U. *Chemical Society Reviews* **2002**, 31, 116.
- (29) Lakowicz, J. R. *Principles of Fluorescence Spectroscopy*, 2006.

- (30) Sharmin, A.; Darlington, R. C.; Hardcastle, K. I.; Ravera, M.; Rosenberg, E.; Ross, J. B. A. *J. Organomet. Chem.* **2009**, 988.
- (31) Allen, J.; Rosenberg, E.; Karakhanov, E.; Kardashev, S.; Maximov, A.; Zolotukhina, A. *Appl. Organometal. Chem.* **2011**, 245.
- (32) Gallezot, P.; Chaumet, S.; Perrard, A.; Isnard, P. *Journal of Catalysis* **1997**, 168, 104.
- (33) Heeres, H.; Handana, R.; Chunai, D.; Borromeus Rasrendra, C.; Girisuta, B.; Jan Heeres, H. *Green Chemistry* **2009**, 11, 1247.
- (34) Jung, C. W.; Garrou, P. E. *Organometallics* **1982**, 1, 658.
- (35) Jurss, J.; Concepcion, J.; Norris, M.; Templeton, J.; Meyer, T. J. *Inorg. Chem.* **2010**, 3980.
- (36) Zhang, J.; Gandelman, M.; Shimon, L. J. W.; Rozenberg, H.; Milstein, D. *Organometallics* **2004**, 23, 4026.
- (37) Jal, P. *Talanta* **2002**, 1005.
- (38) Lu, X.; Manners, I.; Winnik, M. *Macromolecules* **2001**, 1917.
- (39) Susha, A.; Javier, A.; Parak, W.; Rogach, A. *Colloids Surfaces Physiochem. Eng. Asp.* **2006**, 40.
- (40) Allen, J.; Berlin, M.; Johnston, E.; Kailasam, V.; Rosenberg, E.; Sardot, T.; Wood, J. *Mat. Chem. Phys.* **2011**, 973.
- (41) Allen, J.; Johnston, E.; Rosenberg, E. *ACS Appl. Mat. and Interf.* **2012**, 1573.
- (42) Berlin, M.; Allen, J.; Kailasam, V.; Rosenberg, D.; Rosenberg, E. *Appl. Organometal. Chem.* **2011**, 530.
- (43) Fischer, R.; Rosenberg, E. Materials and Methods for the Separation of Copper Ions and Ferric Iron in Liquid Solutions, U.S. Patent, 6,576,590, (2003)
- (44) Fischer, R.; Rosenberg, E. Materials and Methods for the Separation of Copper Ions and Ferric Iron in Liquid Solutions, U.S. Patent, 7,008,601, (2006)
- (45) Hughes, M.; Mirand, P.; Nielsen, D.; Rosenberg, E.; Gobetto, R.; Viale, A.; Burton, S.; Silica Polyamine Composites: New Supramolecular Materials for Cation and Anion Recovery and Remediation in *Recent advances and Novel Approaches in Macromolecul-Metal Complexes* Weinheim, 2006
- (46) Hughes, M.; Nielsen, D.; Rosenberg, E.; Gobetto, R.; Viale, A.; Burton, S. *Ind. and Eng. Chem. Res* **2006**, 6538.
- (47) Hughes, M.; Rosenberg, E. *Sep. Sci. and Tech* **2007**, 261.
- (48) Hughes, M.; Wood, J.; Rosenberg, E. *Ind. and Eng. Chem. Res* **2008**, 6765.
- (49) Kailasam, V.; Rosenberg, E. *Hydrometallurgy* **2012**, 97.
- (50) Pang, D.; Rosenberg, E. System for Extracting Soluble Heavy Metals from Liquid Solutions, U.S. Patent, 5,695,882, (1997)
- (51) Pang, D.; Rosenberg, E. System for Extracting Soluble Heavy Metals from Liquid Solutions, U.S. Patent, 5,997,748, (1999)
- (52) Rosenberg, E.; Fischer, R.; Deming, J.; Anderson, C. *Alta 2000 Technical Proceedings, SX/IX-1, ALTA Metallurgical Services* **2000**.
- (53) Rosenberg, E.; Fischer, R.; Deming, J.; Hart, C.; Mirand, P.; Allen, B.; Silica Polyamine Composites: Advanced Materials for Heavy Metal Recovery, Recycling and Removal in *Symposium Proceedings of the International Conference on Materials and Advanced Technologies* Singapore, 2001



- (54) Rosenberg, E.; Hart, C.; Mine Waste Clean-up with Novel Organic-Inorganic Hybrid Materials in *Proceedings 72nd International Water Conference* 2011
- (55) Rosenberg, E.; Hart, C.; Hughes, M.; Kailasam, V.; Allen, J.; Wood, J.; Cross, B.; Performance Improvement through Structural Design and Comparison with Polystyrene Resins of Silica Polyamine Composites in *Proceedings of the 67th International Water Conference* 2006
- (56) Rosenberg, E.; Hughes, M.; Nielsen, D.; Gobetto, R.; Viale, A.; Burton, S.; Ferel, J. *Ind. and Eng. Chem. Res* **2006**, 6538.
- (57) Rosenberg, E.; Hughes, M.; Wood, J.; Structural Design of Nanoporous Silica Polyamine Composites for Metal Separations in Water in *Proceedings of the 68th International Water Conference* Orlando, Florida, 2007
- (58) Rosenberg, E.; Miranda, P.; Wong, Y. O. Oxine Modified Silica Polyamine Composites for the Separation of Gallium from Aluminum, Ferric from Nickel and Copper from Nickel, U.S. Patent, 8,343,446, (2012)
- (59) Rosenberg, E.; Nielsen, D.; Mirand, P.; Hart, C.; Cao, Y.; Silica Polyamine Composites: Advanced Materials for Ion Recovery and Remediation in *Conference Proceedings of the 66th Annual International Water Conference* 2005
- (60) Guo, X. Q.; Castellano, F. N.; Li, L.; Lakowicz, J. R. *Biophys. Chem.* **1998**, *71*, 51.
- (61) Johnson, P.; Garland, P. B. *Biochem. J.* **1982**, *203*, 313.
- (62) Li, L.; Szmecinski, H.; J. R. Lakowicz, J. R. *Anal. Biochem.* **1997**, *244*, 80.
- (63) Li, L.; Szmecinski, H.; J. R. Lakowicz, J. R. *Biospectroscopy* **1997**, *3*, 155.
- (64) Lippincott-Schwartz, J.; Snapp, E.; Kenworthy, A. *Nat Rev Mol Cell Biol* **2001**, *2*, 444.
- (65) Klug, C. S.; Feix, J. B. *Methods Cell Biol.* **2008**, *84*, 617.
- (66) Gobetto, R.; Caputo, G.; Garino, C.; Ghiani, S.; Nervi, C.; Salassa, L.; Rosenberg, E.; Ross, J. B. A.; Viscardi, G.; Martra, G. *Eur. J. Inorg. Chem.* **2006**, 2839.
- (67) X. Guo, L. L.; F. N. Castellano, H.; Szmecinski, H.; Lakowicz, J. R. *Anal. Biochem.* **1997**, *254*, 179.
- (68) Keles, M.; Keles, T.; Serindag, O.; Yasar, S.; Ozdemir, I. *Phosphorus Sulfur Silicon Relat. Elem.* **2010**, 165.
- (69) Fujita, E. *Coord. Chem. Rev.* **1999**, 373.
- (70) Parker, C. A. *Photoluminescence of Solutions with Applications to Photochemistry and Analytical Chemistry*, 1968.
- (71) Chi, Y.; Chou, P. T. *Chem. Soc. Rev.* **2007**, *36*, 1421.
- (72) Kober, E. M.; Sullivan, B. P.; Dressick, W. J.; Caspar, J. V.; T, J.; Meyer, T. J. *J. Am. Chem. Soc.* **1980**, *102*, 7383.
- (73) Piszczek, G. *Arch. Biochem. Biophys.* **2006**, *453*, 54.
- (74) Dale, R. E.; Chen, L. A.; Brand, L. *J. Biol. Chem.* **1977**, *252*, 7500.
- (75) Chen, P.; Meyer, T. J. *Chem. Rev.* **1998**, *98*, 1439.
- (76) Shan, B. Z.; Zhao, Q.; Goswami, N.; Eichorn, D. M.; Rillema, D. P. *Coord. Chem. Rev.* **2001**, *211*, 117.
- (77) Stufkens, D. J.; Vleek, A. *Coord. Chem. Rev.* **1998**, *177*, 127.
- (78) Terpetschnig, E.; Szmecinski, H. M.; Lakowicz, J. R. *Biophys. J.* **1995**, *68*, 342.
- (79) Kober, E. M.; Meyer, T. J. *Inorg. Chem.* **1983**, *22*, 1614.
- (80) Kober, E. M.; Meyer, T. J. *Inorg. Chem.* **1984**, *23*, 3877.
- (81) Caspar, J. V.; Meyer, T. J. *J. Phys. Chem.* **1983**, *87*, 952.

- (82) Freed, K. F. *Acc. Chem. Res.* **1978**, *11*, 74.
- (83) Kober, E. M.; Casper, J. V.; Lumpkin, R. S.; Meyer, T. J. *J. Phys. Chem.* **1986**, *90*, 3722.
- (84) Kober, E. M.; Marshall, J. L.; Dressick, W. J.; Sullivan, B. P.; Casper, J. V.; Meyer, T. J. *Inorg. Chem.* **1985**, *24*, 2755.
- (85) Balaz, G. C.; Gurezo, G. C.; Schmehl, R. H. *Photochem. Photobiol. Sci.* **2005**, *4*, 89.
- (86) Boyde, S.; Strouse, G. F.; Jones, W. E.; Meyer, T. J. *J. Am. Chem. Soc.* **1990**, *112*, 7395.
- (87) Treadway, J. A.; Loeb, B.; Lopez, R.; Anderson, P. A.; Keene, F. R.; Meyer, T. J. *Inorg. Chem.* **1996**, *35*, 2242.
- (88) Garino, C.; Ghiani, S.; Gobetto, R.; Nervi, C.; Salassa, L.; Ancarani, V.; Neyroz, P.; Franklin, L.; Ross, J. B. A.; Seibert, E. *Inorg. Chem.* **2005**, *44*, 3875.
- (89) Li, L.; F. N. Castellano, F. N.; Gryczynski, I.; Lakowicz, J. R. *Chem. and Phys. of Lipids* **1999**, *99*, 1.
- (90) Youn, H. J.; Terpetschnig, E.; Szmecinski, H.; Lakowicz, J. R. *Anal. Biochem.* **1995**, *232*, 24.
- (91) Kim, J. C.; Bae, S. K.; Kim, J. D. *J. Biochem.* **1997**, *121*, 15.
- (92) Klauda, J. B.; Roberts, M. F.; Redfield, A. G.; Brooks, B. R.; Pastor, R. W. *Biophys. J.* **2008**, *94*, 3074.
- (93) Bonnet, S.; Limburg, B.; Meeldijk, J. D.; Klein-Gebbink, R. J. M.; Killian, J. A. *J. Am. Chem. Soc.* **2011**, *133*, 252.
- (94) Badaea, M. G.; Brand, L. *Methods Enzymol.* **1979**, *61*, 378.
- (95) Barkley, M. D.; Kowalczyk, A. A.; Brand, L. *J. Chem. Phys.* **1981**, *75*, 3581.
- (96) Paoletti, J.; Le Pecq, J. B. *Anal. Biochem.* **1969**, *31*, 33.
- (97) Anderson, C.; Rosenberg, E.; Hart, C.; Ratz, L.; Cao, Y.; Single Step Separation and Recovery of Palladium Using Nitrogen Species Catalysed Pressure Leaching and Silica Polyamine Composites in *Proceedings of the 5th International Symposium on Hydrometallurgy* Warendale, PA, 2003
- (98) Beatty, S.; Fischer, R.; Hagars, D.; Rosenberg, E. *Ind. and Eng. Chem. Res* **1999**, 4402.
- (99) Beatty, S.; Fischer, R.; Pang, D.; Rosenberg, E. *Sep. Sci. and Tech* **1999**, 2723.
- (100) Beatty, S.; Fischer, R.; Pang, D.; Rosenberg, E. *Sep. Sci. and Tech* **1999**, 3125.
- (101) Allen, J.; Rosenberg, E.; Chierotti, M.; Gobetto, R. *Inorg. Chim. Acta* **2010**, 617.
- (102) Badosz, T.; Seredych, M.; Allen, J.; Rosenberg, E. *Chem. of Mat.* **2007**, 2500.
- (103) Gleason, W.; Rosenberg, E.; Sharmin, A.; Hughes, M.; Coordination Analysis of Silica Polyamines by FT-IR in *Proceedings of SME (Society for Mining, Metallurgy and Exploration) Hydrometallurgy Conference* Phoenix, Arizona, 2008
- (104) Karakhanov, E.; Maksimov, A.; Zatochnaya, O.; Rosenberg, E.; Hughes, M.; Kailasam, V. *Petrol Chem* **2009**, 107.
- (105) Nielsen, D.; McKenzie, J.; Clancy, J.; Rosenberg, E. *Chimica Oggi* **2009**, 42.
- (106) Rosenberg, E. In *Macromolecules Containing Metal and Metal-Like Elements*; J. Wiley & Sons: New York, 2005; Vol. 4, p 51.
- (107) Wong, Y. O.; Mirand, P.; Rosenberg, E. *J. App. Poly. Sci.* **2010**, 2855.
- (108) Fletcher, P.; Holt, B. *Langmuir* **2011**, 12869.
- (109) House, H. *Modern Synthetic Reactions*; Benjamin, A.: Menlo Park CA, 1972.

- (110) Wang, S. G. *Catal. Commun.* **2003**, 469.
- (111) Allen, J.; Rosenberg, E.; Johnston, E.; Hart, C. *ACS Appl. Mat. and Interf.* **2012**, 1573.
- (112) Sautet, P.; Delbecq, F. *Chem. Rev.* **2010**, 1788.
- (113) Cousinie, S.; Gressier, M.; Alphonse, P.; Menu, M. *Chem. Mater.* **2007**, 6492.
- (114) Kramer, J.; Driessen, W.; Koch, K.; Riedek, J. *Sep. Sci. and Tech* **2004**, 63.
- (115) Shiraishi, Y.; Nishimura, G.; Hirai, T.; Komasaawa, I. *Ind. and Eng. Chem. Res* **2002**, 5.
- (116) Soliman, E. *Analytical Letters* **1997**, 1739.
- (117) Yoshitake, H.; Joiso, E.; Tatsumi, T.; Horie, H.; Yoshimora, H. *Chem. Lett.* **2004**, 872.
- (118) Fischer, R.; Pang, D.; Beatty, S.; Rosenberg, E. *E. Sep. Sci. Technol.* **1999**, 312.
- (119) Menu, M.; Cousinie, S.; Mauline, L.; Gressier, M.; Kandibanda, S.; Datas, L.; Reber, C. *New J. Chem.* **2012**, 1355.
- (120) Rosso-Vassic, M.; De Cola, L.; Zuilhof, H. *J. Phys. Chem.* **2009**, 2235.
- (121) Johnson, M.; Frasier, S. In *Methods in Enzymology*; Academic Press: New York, 1985; Vol. 117, p 301.
- (122) Shiraishi, Y.; Nishimura, G.; Hirai, T.; Komasaawa, I. *Ind. and Eng. Chem. Res* **2002**, 5065.
- (123) Waddell, T.; DE, L.; DeBello, M. *J. Am. Chem. Soc.* **1981**, 5303.
- (124) Borisov, O.; Coleman, D.; Oudsema, K.; Carter III, R. *J. Anal. Atomic Spectrometry* **1997**, 239.
- (125) Strouse, G. F.; Schoonover, J.; Duesing, R.; Boyde, S.; Jones, W. E.; Meyer, T. J. *Inorg. Chem.* **1995**, 473.
- (126) Woznica, E.; Maksymiuk, K.; Michalska, A. *Analytical chemistry* **2014**, 86, 411.
- (127) Yuan, Z.; Cai, N.; Du, Y.; He, Y.; Yeung, E. S. *Analytical chemistry* **2014**, 86, 419.
- (128) Gong, Z.-L.; Zhong, Y.-W. *Organometallics* **2013**, 32, 7495.
- (129) McGlynn, S.; Azumi, T.; Kinoshita, M. *Molecular Spectroscopy of the Triplet State*; Prentice-Hall: Englewood Cliffs, NJ, 1969.
- (130) Zambrana, J. L.; Ferloni, E. X.; Colis, J. C.; Gafney, H. D. *Inorg. Chem.* **2008**, 47, 2.
- (131) Ross-Vasic, M.; De Cola, L.; Zuilhof, H. *J. Phys. Chem.* **2009**, 2235.

## Appendix A

### Time resolved luminescence spectroscopy methods

Time-resolved luminescence decay and anisotropy decay measurements were performed by time-correlated single-photon counting (TCSPC), using the Quantum Northwest FLASC 1000 sample chamber (Spokane, WA). In the FLASC 1000, the vertical (V or  $0^\circ$  to vertically polarized excitation) and horizontal (H or  $90^\circ$ ) emission components are separated on one side of the sample cuvette, orthogonal to the excitation path, by a beam-splitting Glan-Thompson polarizer (Karl Lambrecht, Chicago, IL). This allows simultaneous detection of the V and H anisotropy decay components by separate detectors, which assures data collection under identical excitation conditions. A variable-angle polarizer in the excitation path was rotated to the magic angle ( $54.7^\circ$  with respect to the vertically polarized component of the emission) for determination of the luminescence lifetime. Pulsed excitation at 470 nm and a repetition rate of either 250 KHz or 5.0 MHz from a LDH-P-C 470 laser diode (PicoQuant, Berlin, Germany) was used for the time-dependent studies. The H and V emission components were isolated through matched bandpass filters, using 590/25 nm (Andover, Salem NH) for complexes **1**, **2**, and **5 – 7** or 530/25 nm (Andover, Salem NH) for complexes **3** and **4**. The V and H decay curves were collected for equal lengths of time using the TimeHarp 200 PCI board (PicoQuant, Berlin) until  $4 \times 10^4$  counts were obtained at the maximum of the V curve. The timing resolution was 1120 ps/channel for the microsecond-timescale decays or 35 ps/channel for the nanosecond timescale decays. The luminescence intensity decays for the probes in organic solvent were calculated by fitting the data to a single exponential decay model, where  $I(t)$  is the time dependent intensity,  $I_0$  is intensity at time 0 and  $\tau$  is the excited-state lifetime.

$$I(t) = I_0 \exp(-t/\tau) \quad (\text{A1})$$

A multi-exponential decay model was required for fitting the lifetime data of these probes in model membrane environments. Here,  $\tau_i$  is the lifetime and  $\alpha_i$  is the amplitude of the  $i$  th component; the magic angle decay is  $I(t)$ :

$$I(t) = \sum_{i=1}^n \alpha_i e^{-t/\tau_i} \quad (\text{A2})$$

In the time-resolved anisotropy experiment, the depolarization of the emitted light that results from molecular rotation is given by

$$r(t) = \frac{I_{VV}(t) - I_{VH}(t)}{I_{VV}(t) + 2I_{VH}(t)} = \sum_{j=1}^5 \beta_j e^{-t/\phi_j} \quad (\text{A3})$$

where  $I_{VV}(t)$  and  $I_{VH}(t)$  represent the vertical and horizontal decays, respectively, obtained using vertical excitation. The pre-exponential factors,  $\beta_j$ , are trigonometric functions of the angles between the excitation and emission transition dipole moments of the probe and the symmetry axes of the ellipsoid of revolution [29], and the sum of  $\beta_j$  is the fundamental anisotropy at zero time,  $r_0$ , when no motion has occurred. The rotational correlation times,  $\phi_j$ , depend on the size and shape of the probe and also on the temperature and viscosity of the surrounding medium. The denominator of Equation S3 is the total intensity decay,  $I(t)$ , given by S2. The anisotropy decay data were analyzed using the software package FluoFit Pro (PicoQuant, Berlin). For anisotropy analysis, the individual vertical and horizontal decays,  $I_{VV}(t)$  and  $I_{VH}(t)$ , respectively, were fit simultaneously according to the following relationships:

$$I_{VV}(t) = G \frac{1}{3} \sum_{i=1}^n \alpha_i e^{-t/\tau_i} \left[ 1 + 2(r_\infty + \sum_{j=1}^n \beta_j e^{-t/\phi_j} \right] \quad (\text{A4a})$$

$$I_{VH}(t) = \frac{1}{3} \sum_{i=1}^n \alpha_i e^{-t/\tau_i} \left[ 1 - (r_\infty + \sum_{j=1}^n \beta_j e^{-t/\phi_j} \right] \quad (\text{A4b})$$

where  $r_\infty$  is the anisotropy at infinite time [30], and  $G = \int I_{HV} dt / \int I_{HH} dt$  is a factor, obtained using horizontal excitation, that corrects for the difference in the efficiencies of the V and H detection channels; under ideal conditions  $G \sim 1$ .<sup>74,95</sup>

### Synthesis of dcbpy-*N*-(DPPE)<sub>2</sub> (11)

The succinimidyl ester of 4,4'-dicarboxylic-2,2'-bipyridyl (dcbpy) was synthesized by reacting 50 mg (0.204 mmol) of dcbpy with 46 mg (0.408 mmol) of *N*-hydroxysuccinimide in the presence of *N,N'*-dicyclohexylcarbodiimide (126 mg, 0.61 mmol) for 3 hr at room temperature under N<sub>2</sub>. The precipitate (urea) was removed by filtering on 0.45- $\mu$ m filter paper and the filtrate was added to a large excess of stirring isopropanol at 4 °C resulted in crystallization of 40 mg of dcbpy-*N*-succinimidyl. After filtering and washing with dry ethylether, 31 mg of crystals were obtained (35% yield). 70 mg (0.10 mM) of DPPE in 7 mL chloroform was added to the dimethylformamide (DMF) solution of dcbpy-succinimidyl (20 mg, 0.05 mM) in the presence of a catalytic amount of triethylamine. The reaction was stirred for 24 hrs at room temperature under N<sub>2</sub>. Solvent was removed by rotary evaporation and the residue was purified by thin-layer chromatography on silica plates. Two elutions with the solvent mixture hexane/ methylene chloride/ethanol (6.5: 3.5: 0.5) yielded three bands. The fastest moving UV-absorbing band was identified as un-reacted dcbpy-*N*-succinimidyl, the second UV absorbing band was the un-reacted DPPE and the slowest moving pale-yellow band gave dcbpy- *N*-DPPE<sub>2</sub> (11) in 10%

yield (8 mg). IR in KBr: CO stretching frequency at 1732 (s), 1687 (s) and CH aliphatic 2963 (s), 2924 (s), 2851 (m)  $\text{cm}^{-1}$ ;  $^1\text{H}$  NMR ( $\text{CDCl}_3$ )  $\delta = 9.3\text{-}7.6$  (6 H), 4.8-2.3 (18H), 2.1-0.81 (124H).

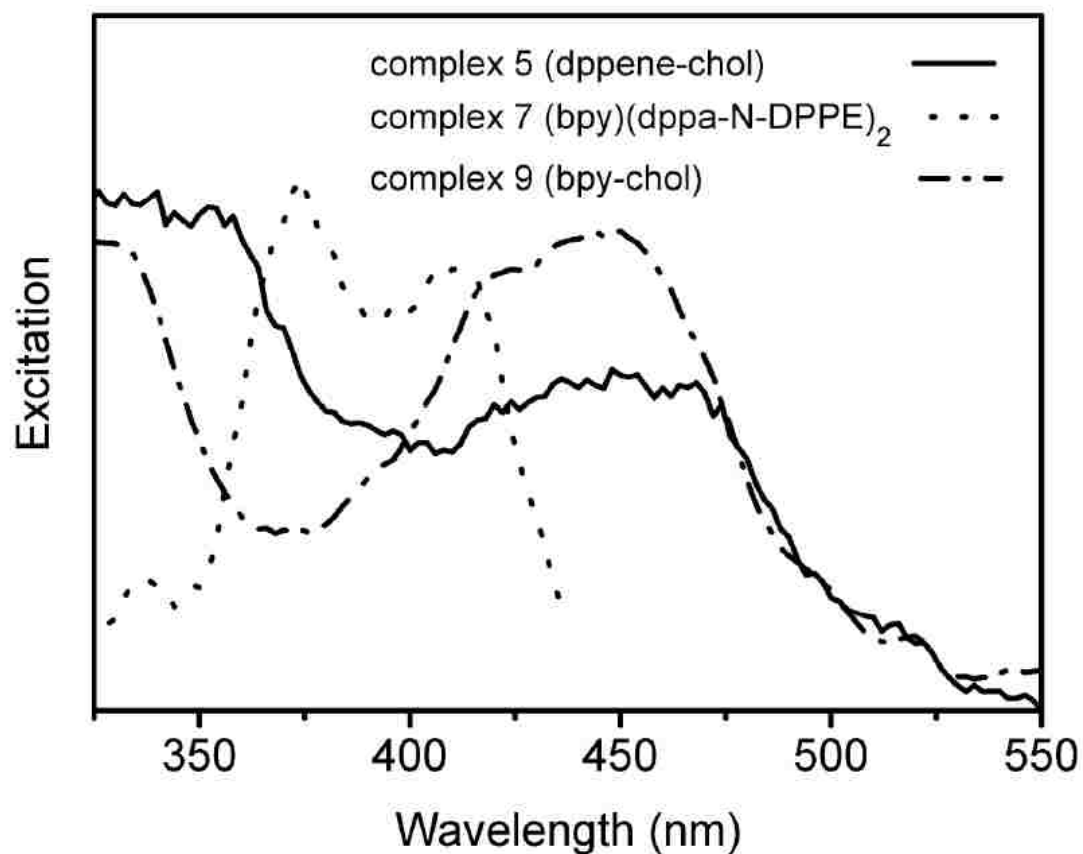


**Figure A1:** Excitation spectra of  $[(\text{H})\text{Ru}(\text{CO})(\text{dppene})(1,10\text{-phen-}5\text{-NHC}(\text{O})\text{OChol})][\text{PF}_6]$  (**5**),  $[(\text{H})\text{Ru}(\text{PPh}_2\text{C}_2\text{H}_4\text{C}(\text{O})\text{-}N\text{-DPPE})_2(\text{bpy})(\text{CO})][\text{PF}_6]$  (**7**), and  $\text{Ru}(\text{bpy})_2(\text{phen-}5\text{-NHC}(\text{O})\text{Chol})[\text{PF}_6]$  (**9**).

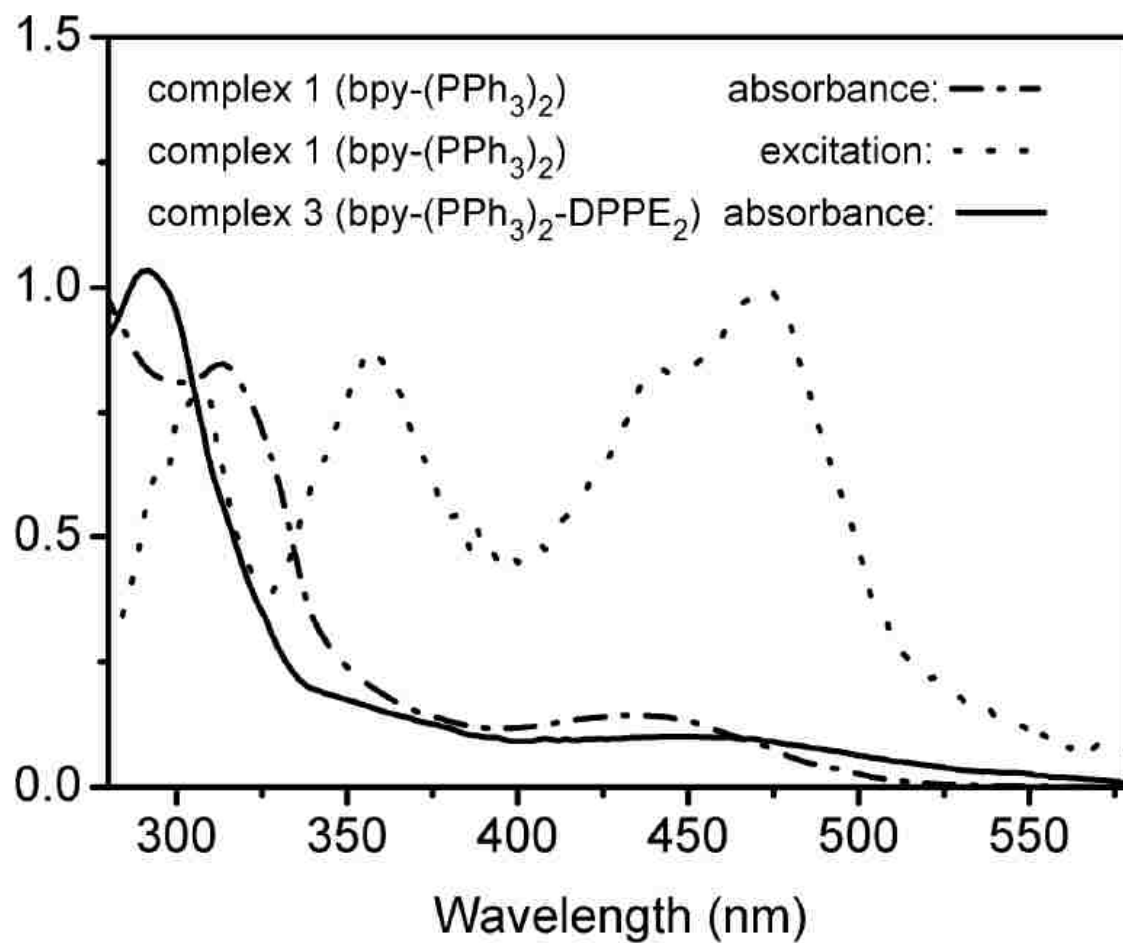


**Figure A2** Absorption and excitation spectrum for complex 1 and absorption spectrum for complex 3



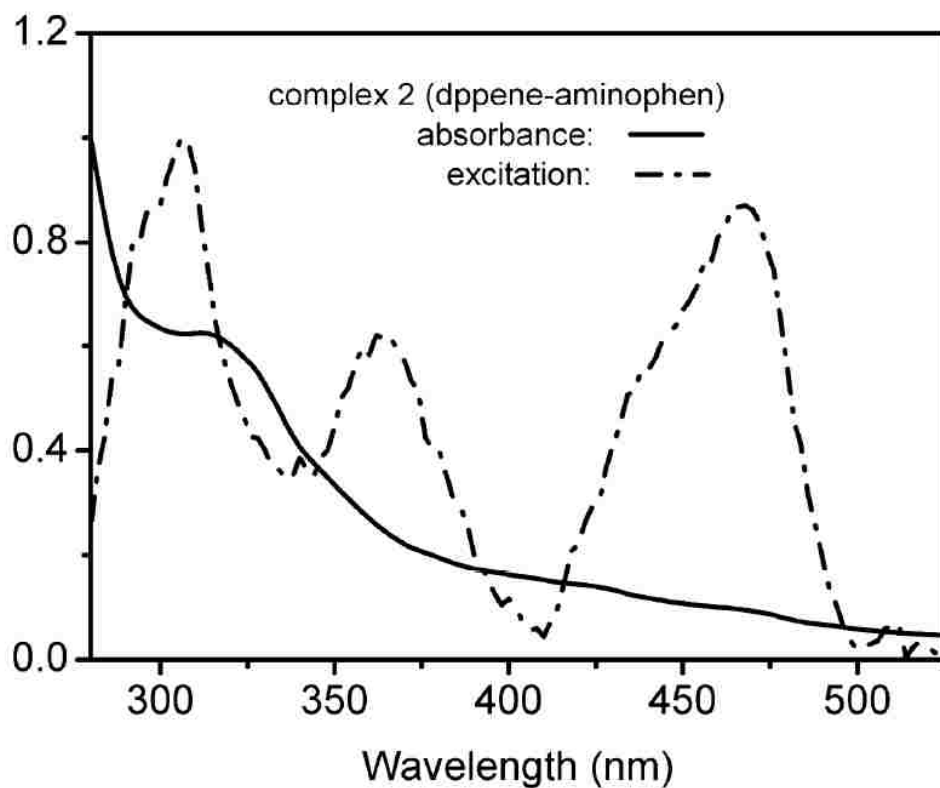


Figure A3. Absorption and excitation spectra for complex 2

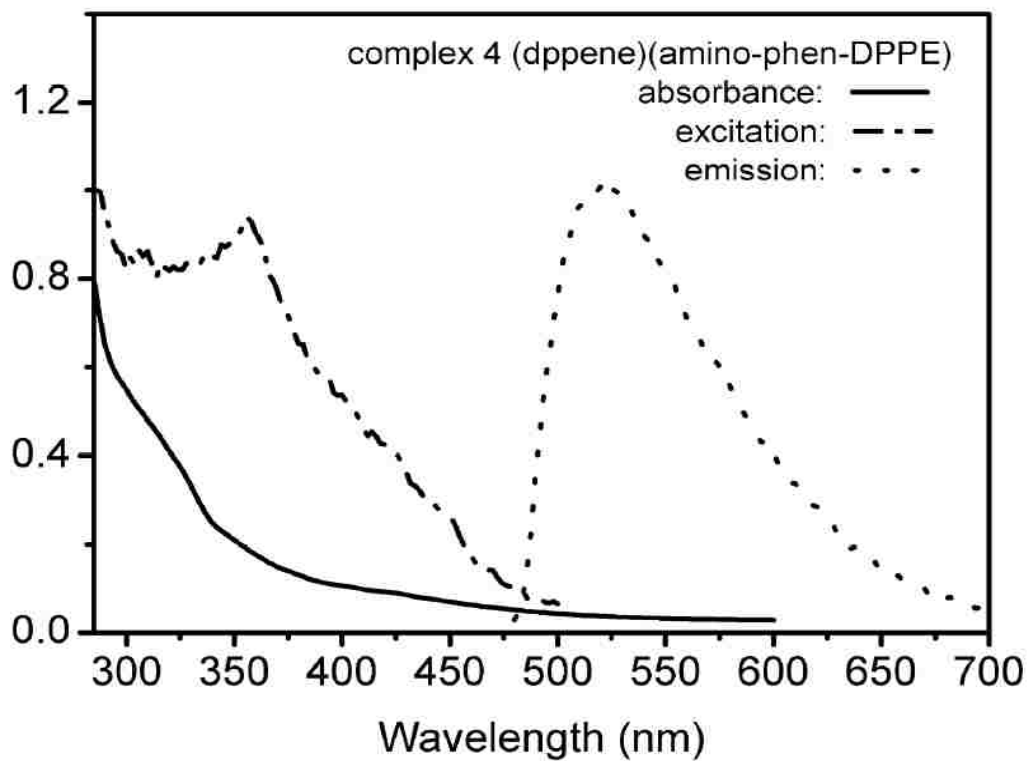
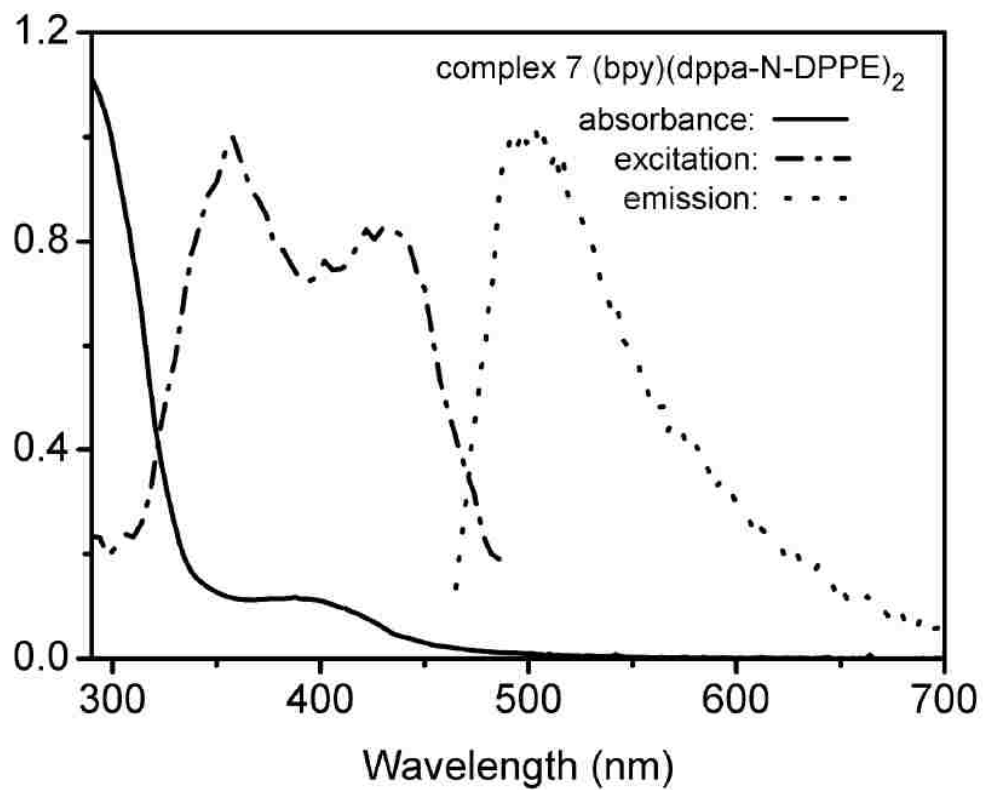


Figure A4 Absorption, excitation and emission spectra for complex 4



A5. Absorption, excitation and emission spectra for complex 7

## 500 MHz Proton NMR of Compounds 4,5,7 and 9

### Figure A6 Compound 4

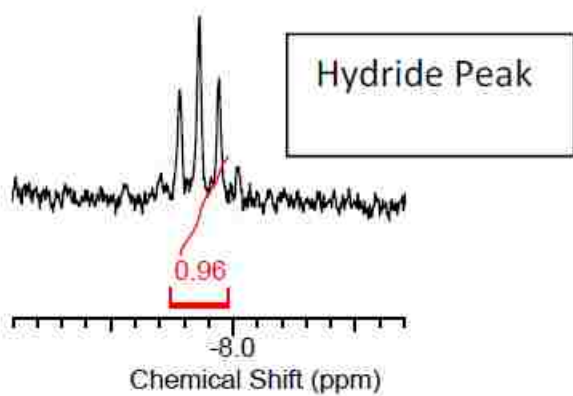
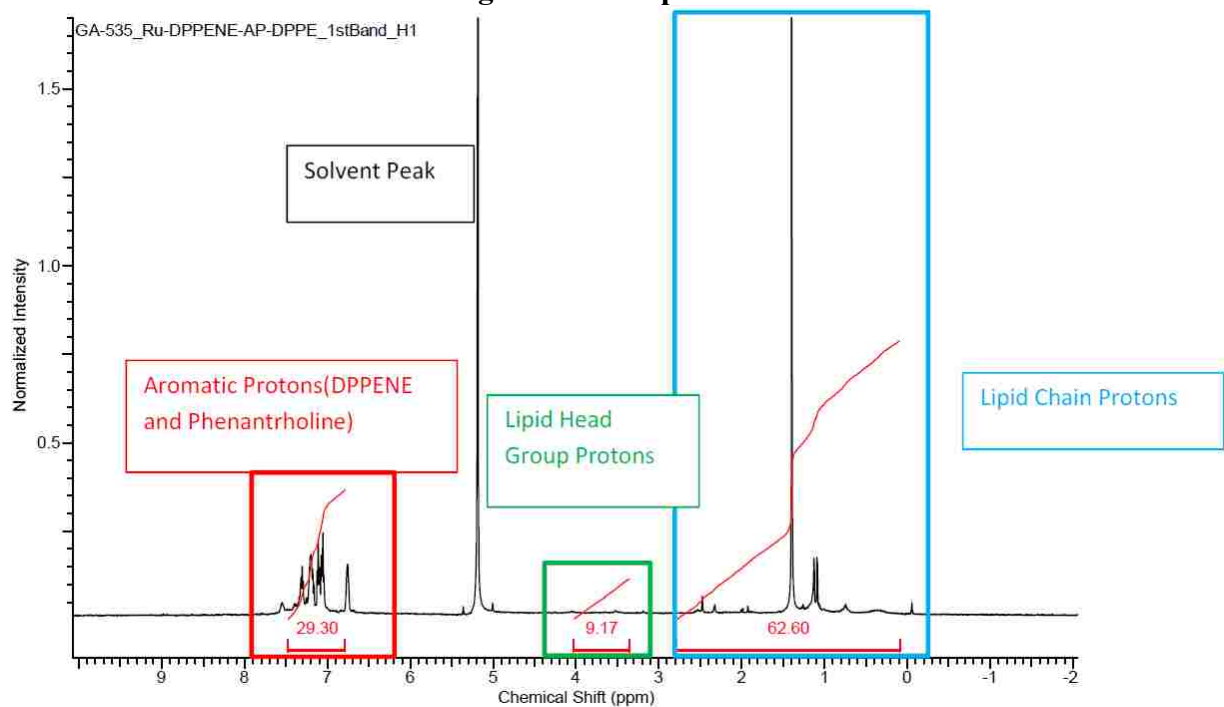
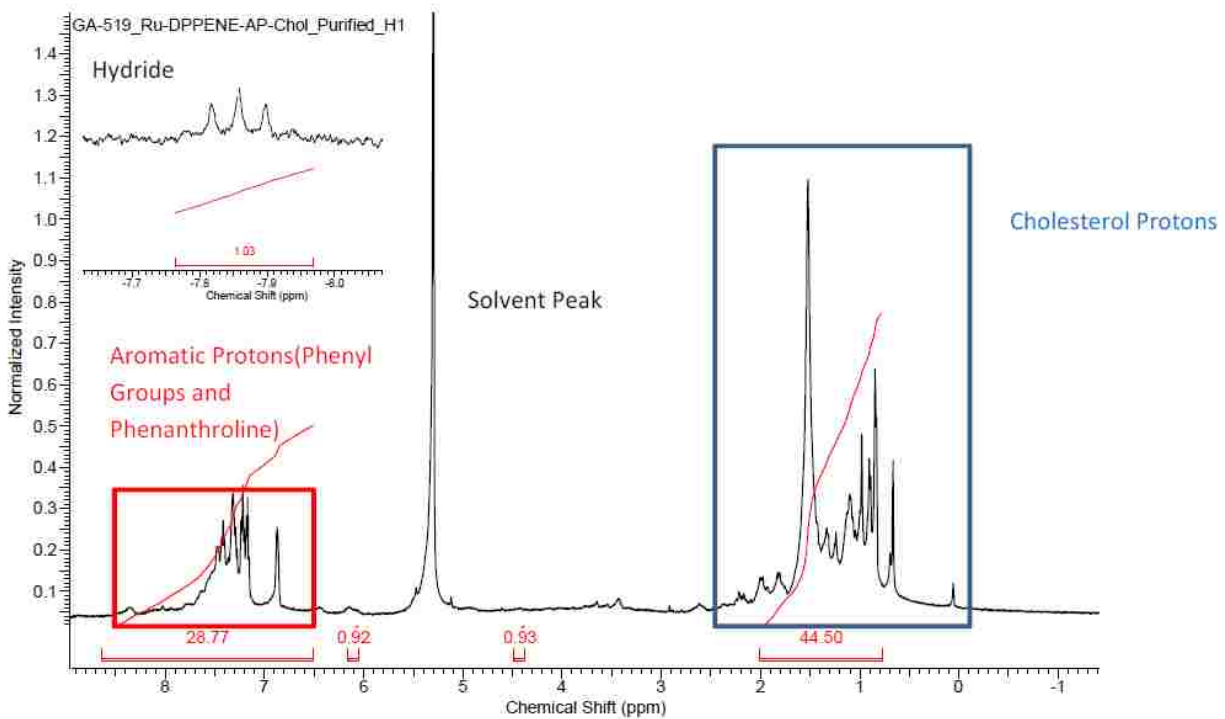
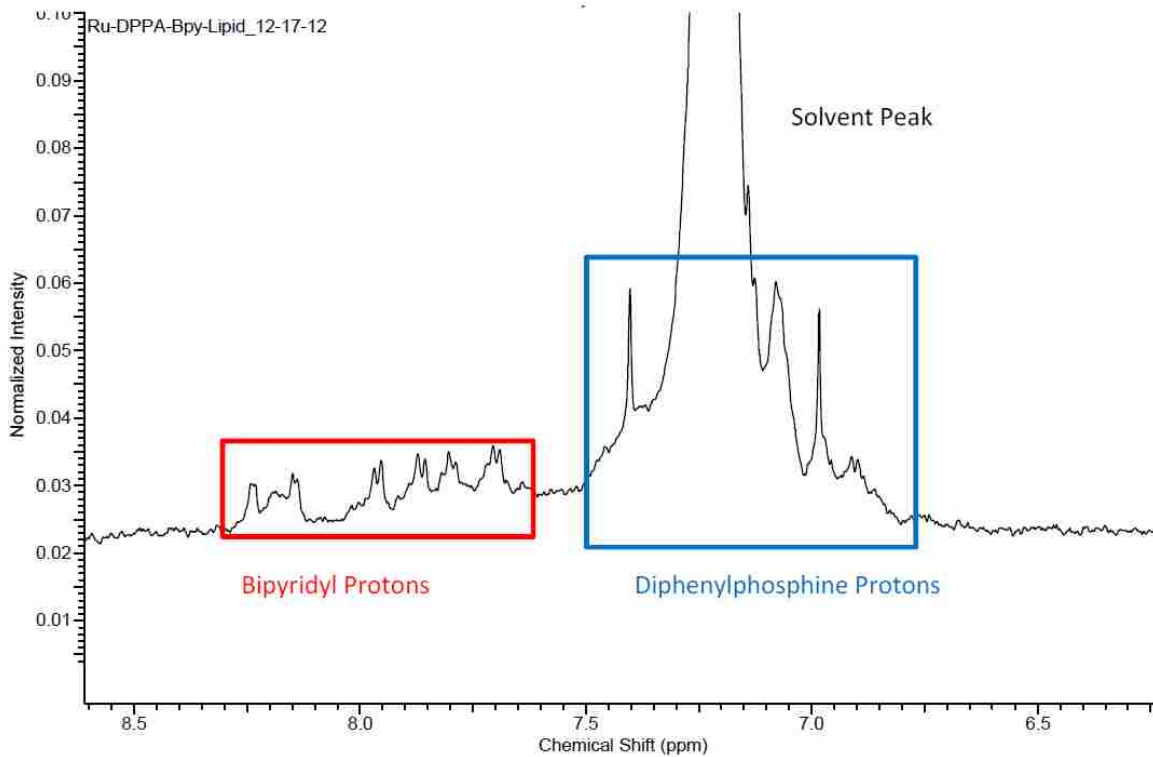
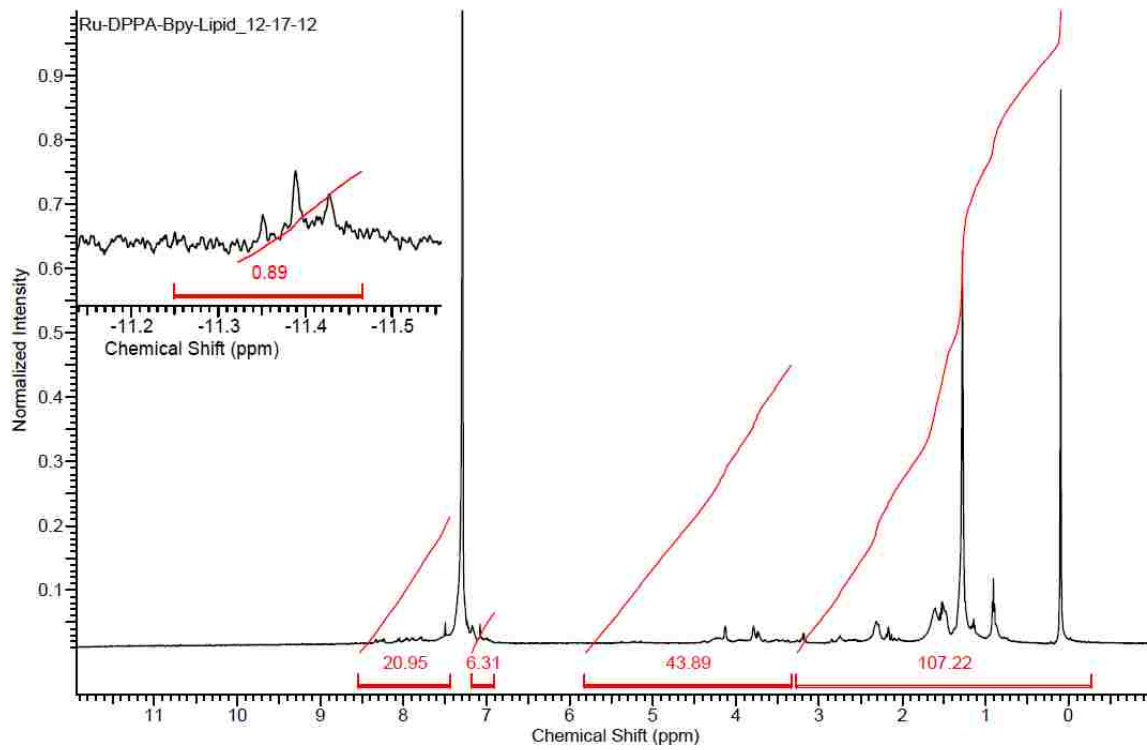


Figure A7 Compound 5



**Figure A8 Compound 7**



**Figure A9 Compound 9**

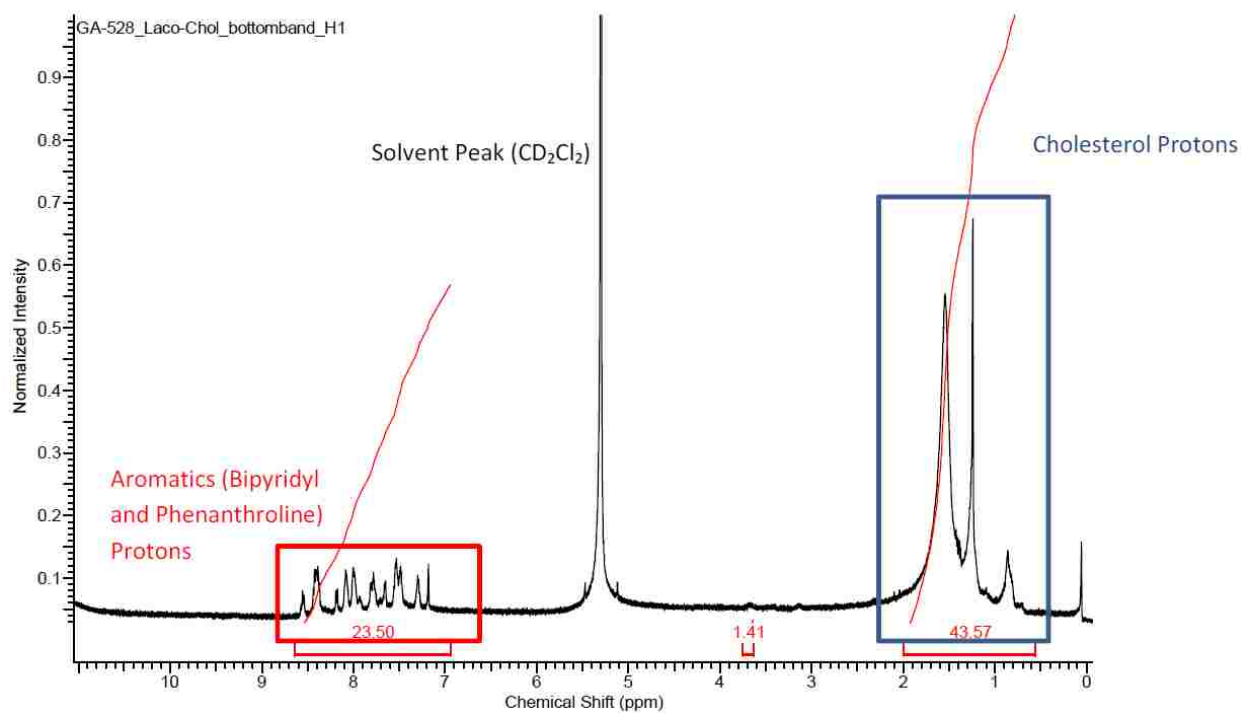
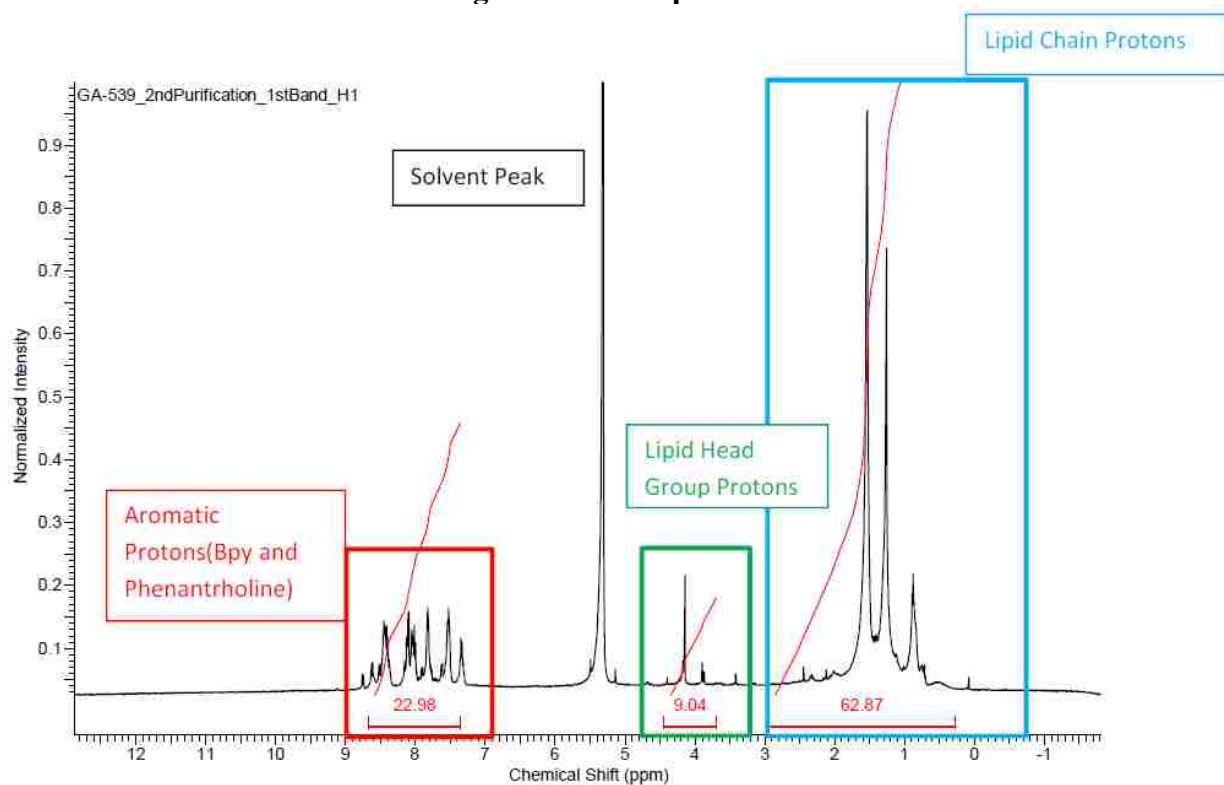


**Figure A10 Compound 10**



## Appendix B: Additional Schemes and Figures for Chapter 4

### Scheme B1 Isomers of Compounds 4 and 4'

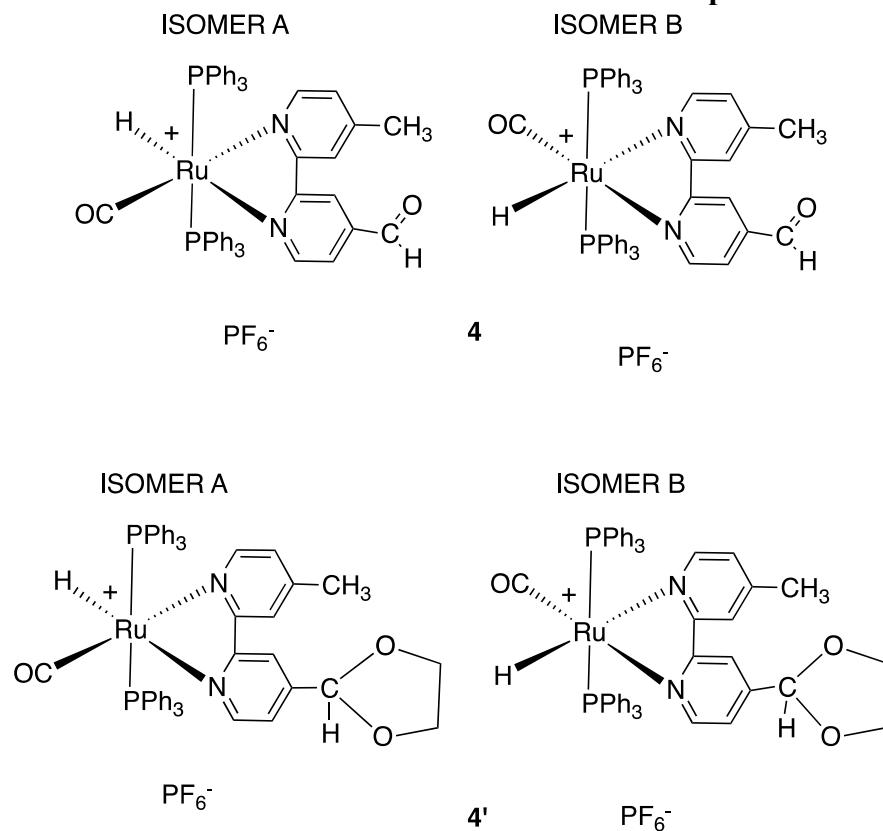


Figure B1a <sup>1</sup>H NMR of 4 and 4'

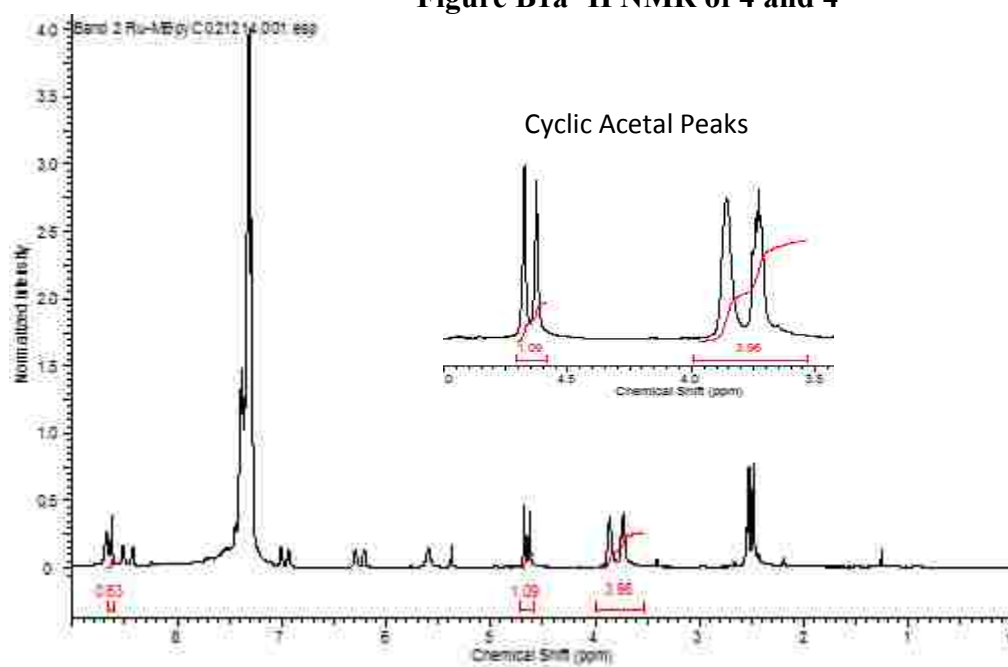


Figure B1b <sup>1</sup>H NMR of 4 and 4'

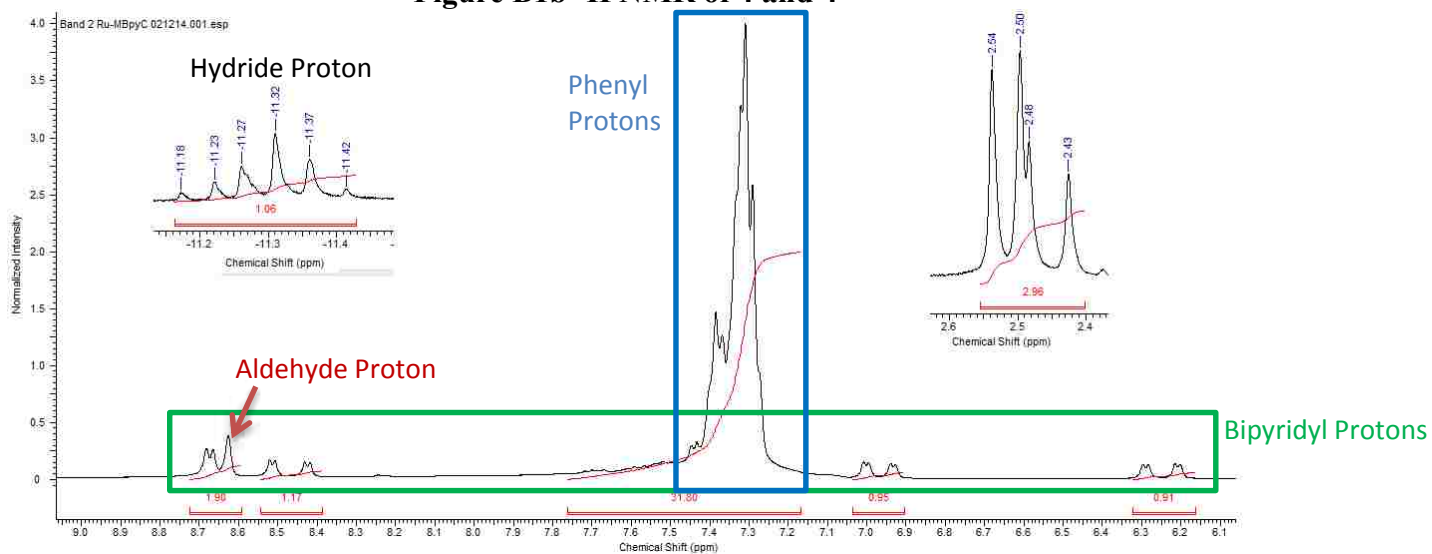
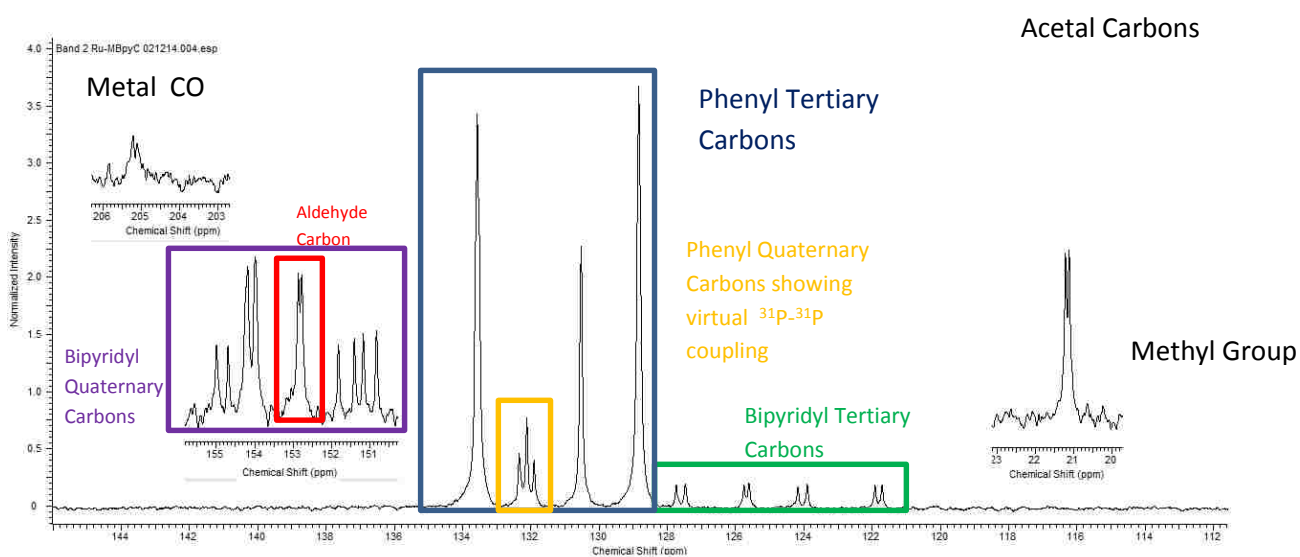
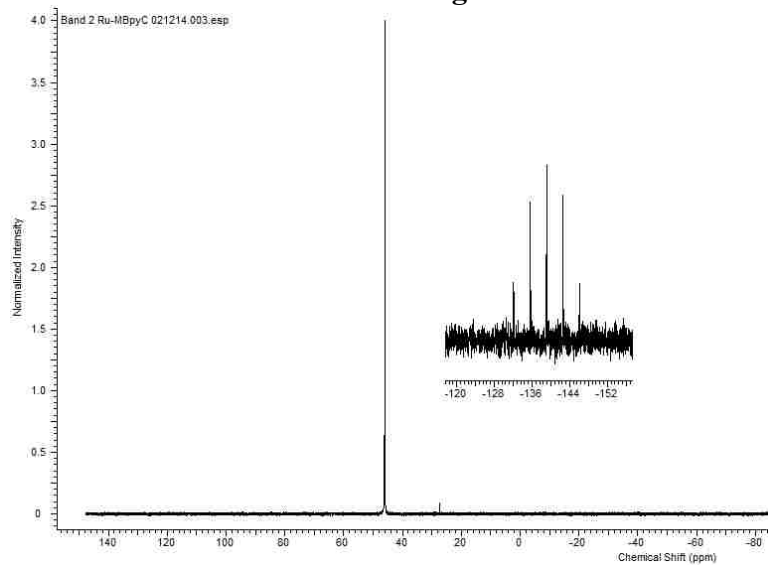


Figure B2 <sup>13</sup>C NMR of 4 and 4'





**FigureB3  $^{31}\text{P}$ NMR of 4 and 4'**



**Figure B4  $^{19}\text{F}$  NMR of 4 and 4'**

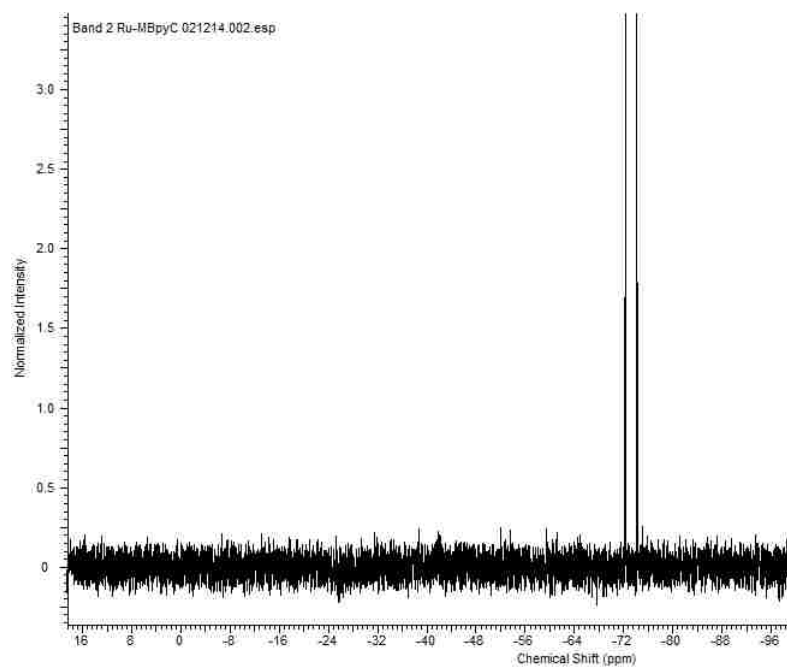


**Figure B5  $^{13}\text{C}$  SSNMR MPA-1 (Enriched)**

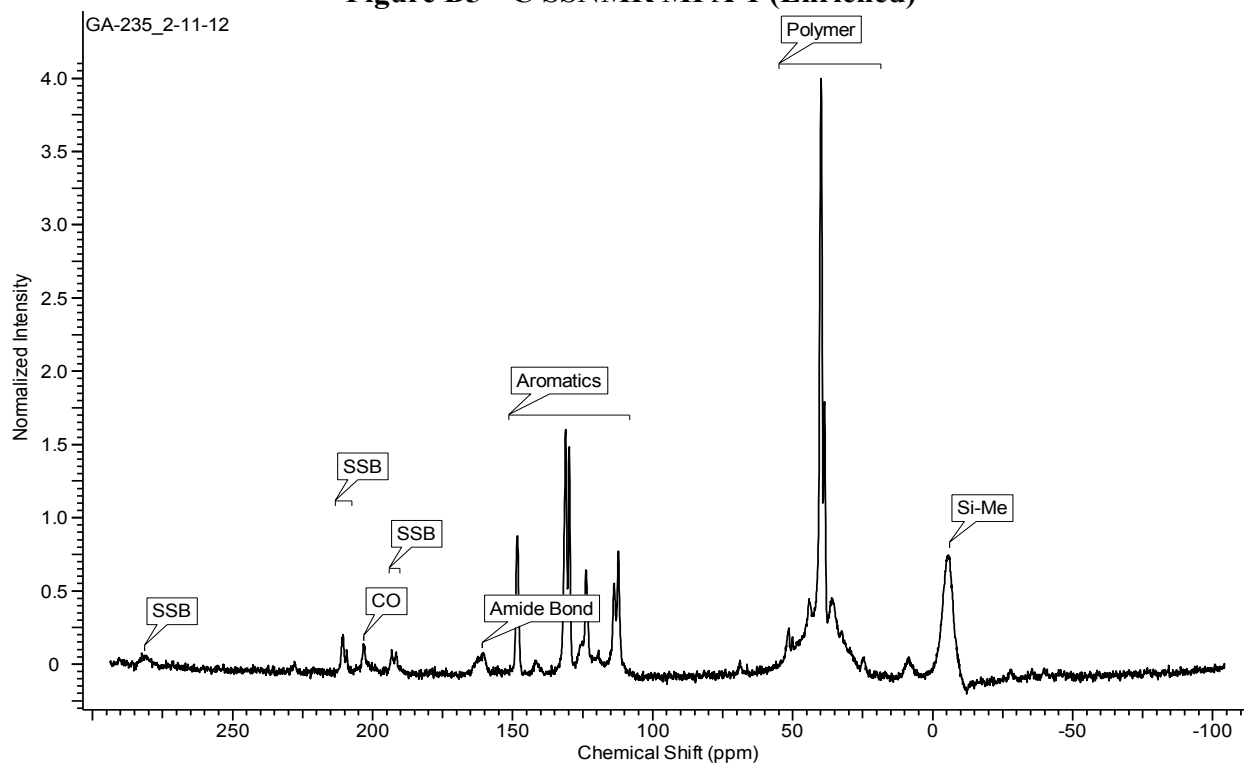


**Figure B6  $^{13}\text{C}$  SSNMR MPA-2 (Enriched)**

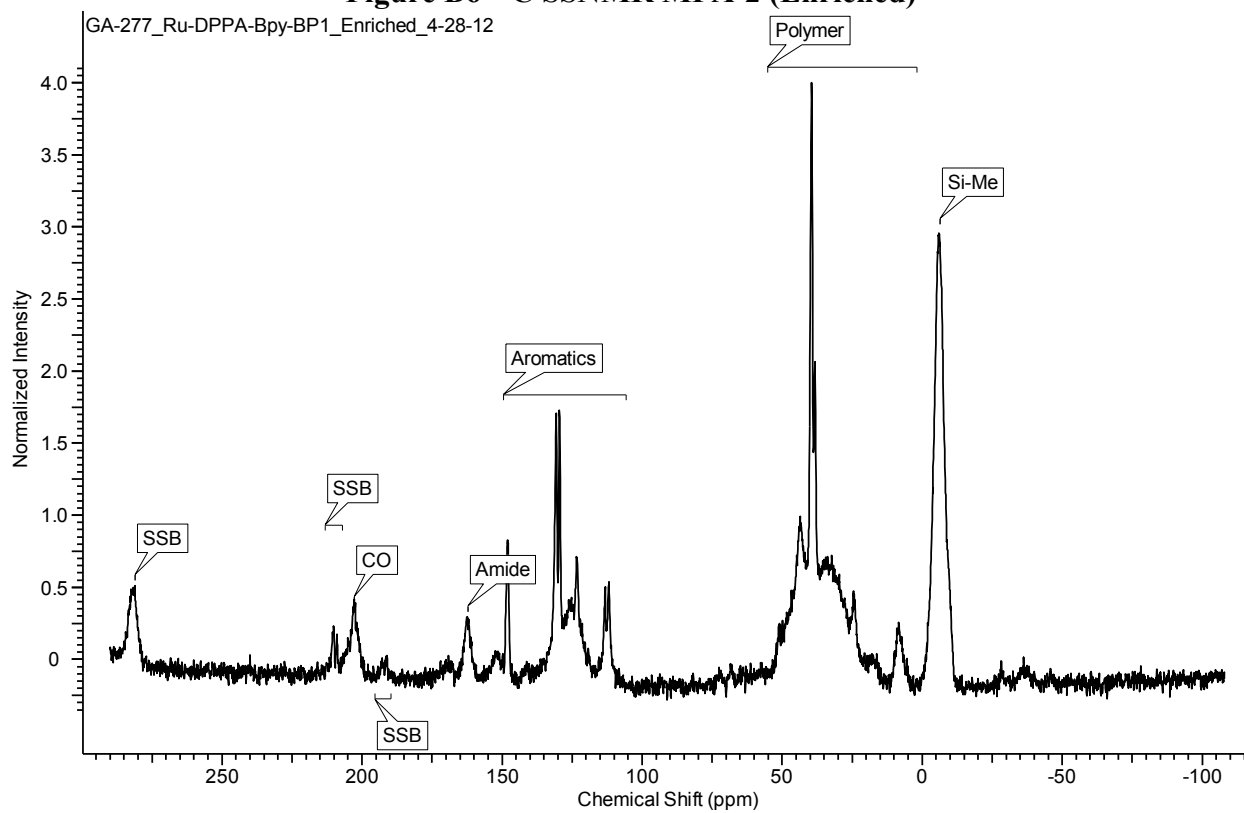


**Figure B7  $^{13}\text{C}$  SSNMR MPA-3 (Enriched)**

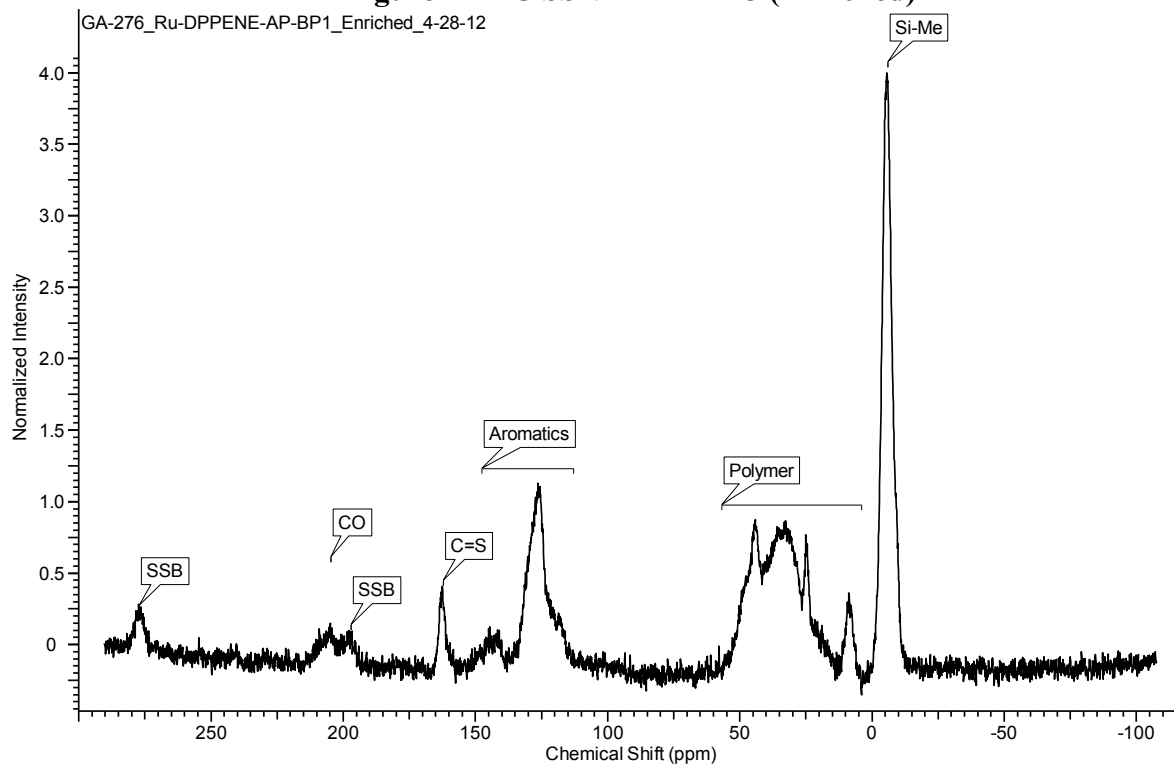


**Figure B8  $^{13}\text{C}$  SSNMR MPA-4 (Natural Abundance)**

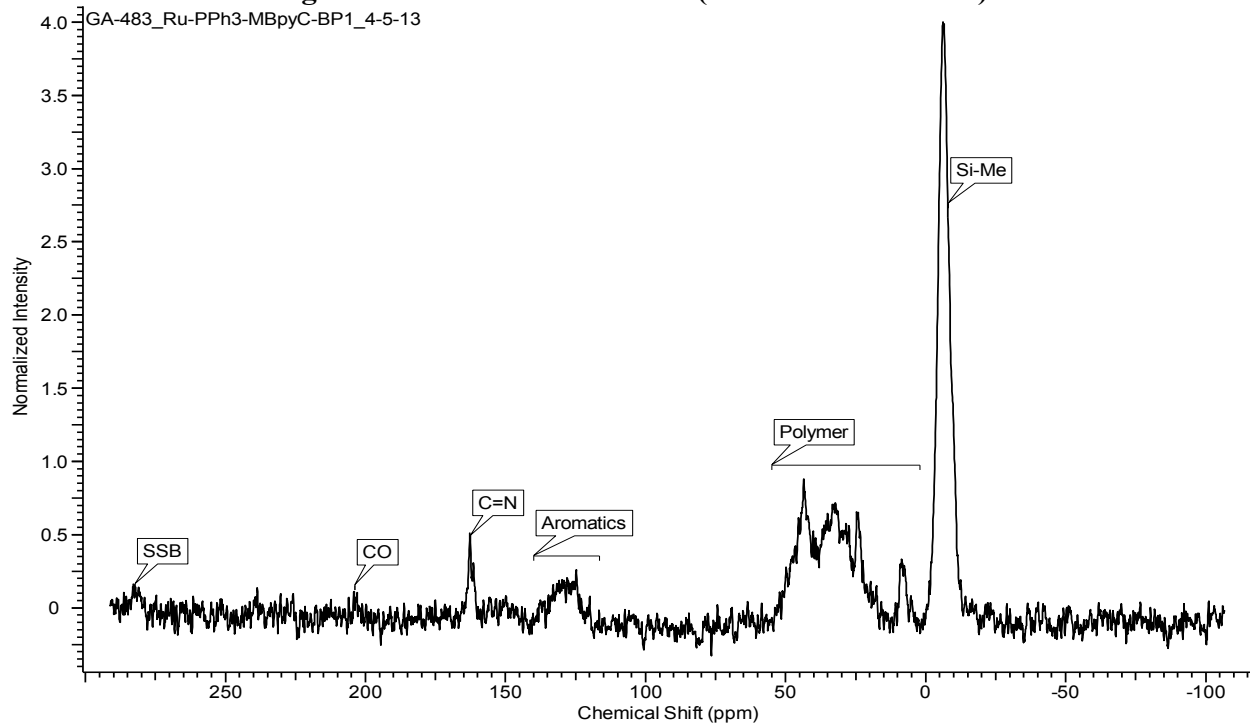


**Figure B9  $^{13}\text{C}$  SSNMR NPA-1 (Partially Enriched)**

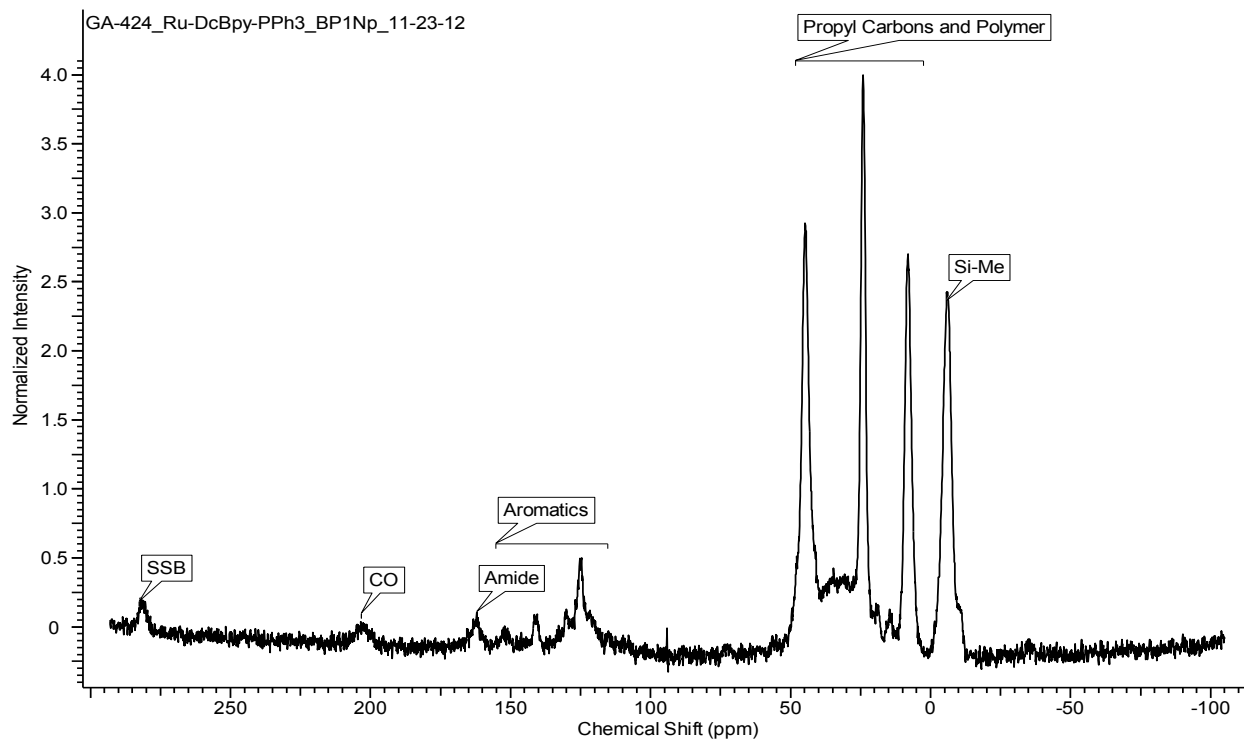


**Figure B10  $^{13}\text{C}$  SSNMR NPA-2 (Natural Abundance)**

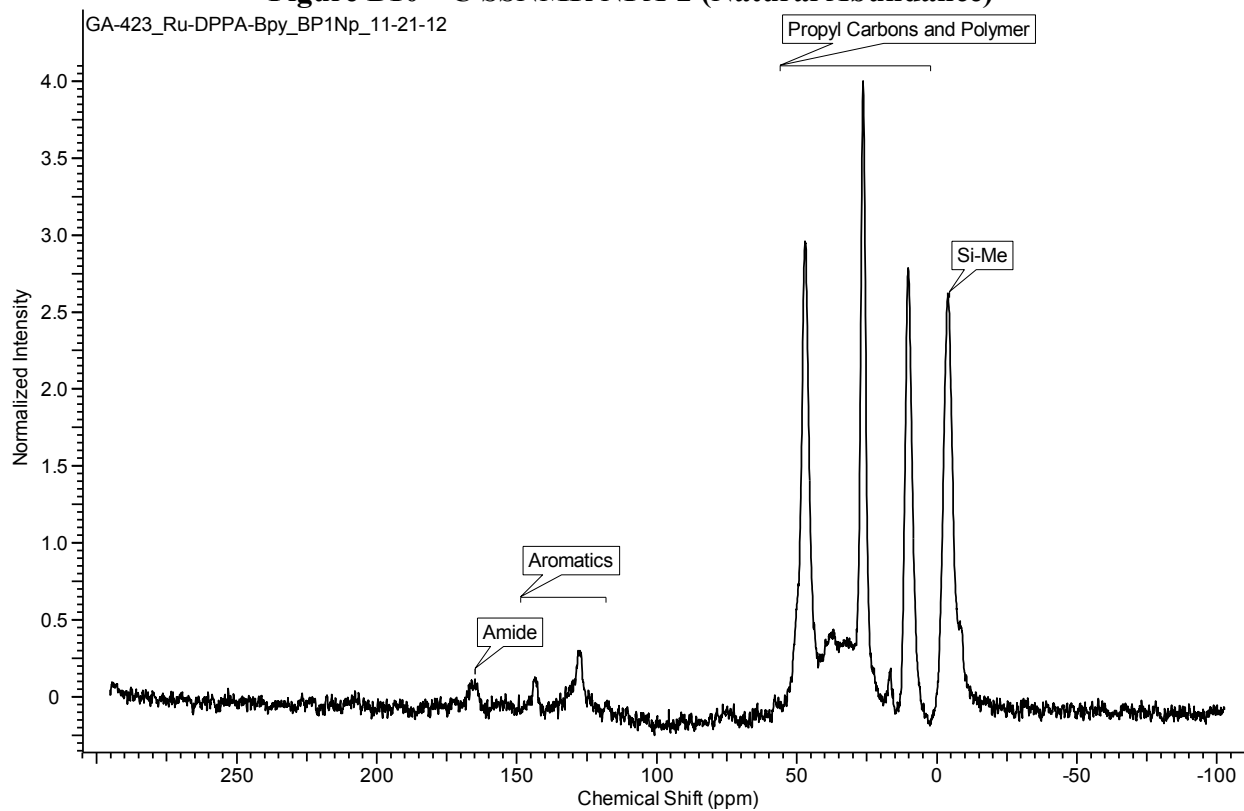


**Figure B11  $^{13}\text{C}$  SSNMR NPA-3 (Natural Abundance)**

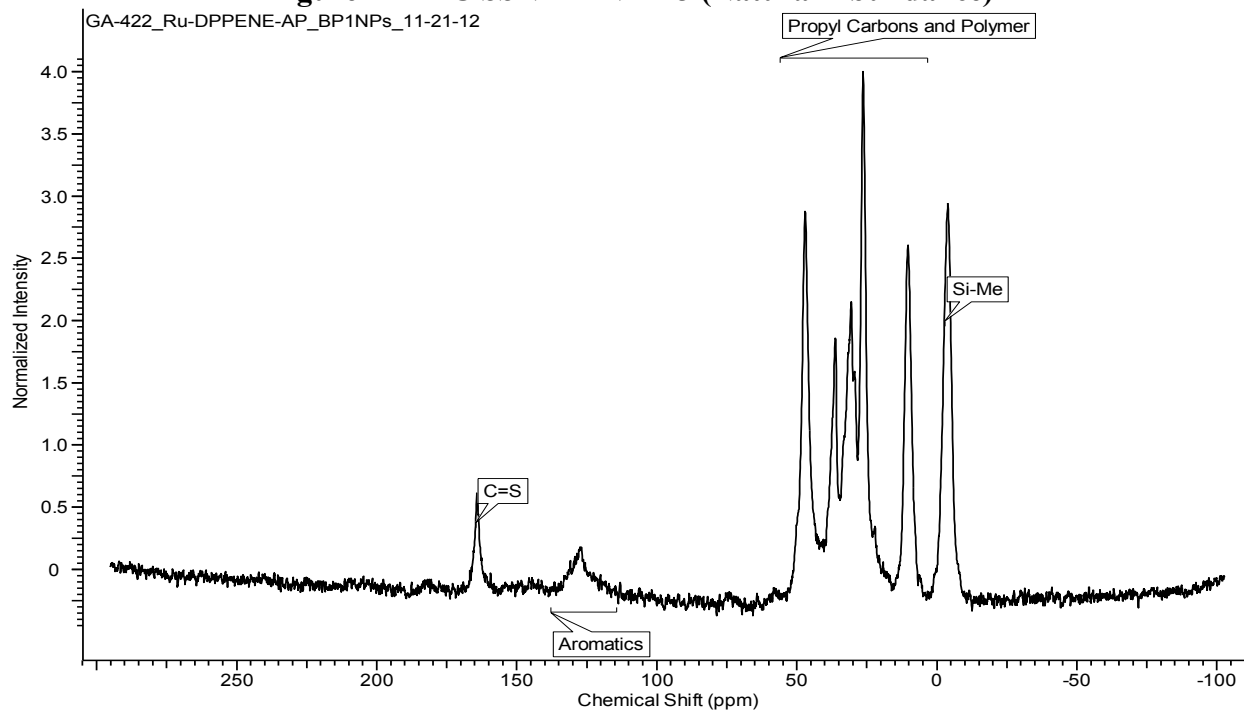


**Figure B12  $^{13}\text{C}$  SSNMR NPA-4 (Natural Abundance)**

